YAHIA FARES MEDEA UNIVERSITY

Faculty of Technology

Department of Process Engineering

DOCTORAL THESIS

In Environmental Science and Engineering

SYNTHESIS, CHARACTERIZATION AND APPLICATION OF BIDIMENSIONAL MATERIAL (MXENES) IN WATER DEPOLLUTION

By

Hiba BENAMOR

Jury Composition:

President: Mr. Nadiji MOULAI-MOSTEFA, Professor, University of Medea.

Examinators: Mme Razika KHELLADI, Associate professor, University of Medea.

Mr. Aziz SERAI, Associate professor, University of Medea.

Mr. Hocine BOUTOUMI, Professor, University of Blida 1.

Mr. Adel HADDAD, Associate professor, University of Blida 1.

Thesis director: Mr. Mohamed KREA, Professor, University of Medea.

Thesis Co-director: Mr. Omar. BOURAS, Professor, University of Blida 1.

Medea, February 2024

ملخص

في هذه الأطروحة تم تركيب و توصيف وتطبيق سيراميك ثلاثي محدد MAX وMAB إلى جنب المشتقة ثنائية الأبعاد MXenes لغرض امتصاص الملكيت الأخضر. ولتحقيق ذلك، تم تصنيع MAB وMAX من خلال استخدام طريقة MS^3 , تمت دراسة تاثير المادة المضافة Sn والأملاح في حالة Fe_2AlB_2 وCr_2AlC.

خضعت المساحيق الناتجة للفحص باستخدام تقنيات مثل حيود الأشعة السينية XRD والمجهر الإلكتروني الماسح SEM والتحليل الحراري الوزني (TGA) والتحليل الحراري التفاضلي (DTA). أظهرت النتائج أنه يمكن الحصول على Fe_2AlB_2 باستخدام المادة المضافة Sn وCr_2AlC مع ملح KCl بدرجة نقاء عالية عند 1000 درجة مئوية لمدة ساعة واحدة.

الجزء التالي من هذه الأطروحة مخصص لإنتاج MXene، والذي يتم تحقيقه عن طريق إزالة العنصر A من MAX عبر طريقة كيميائية. تم إخضاع المساحيق الناتجة للتقييم من خلال تحليل حيود الأشعة السينية XRD وتحليل Brunauer-Emmett-Teller (BET).

الجزء الأخير من البحث يتعلق بالتطبيق العملي لهذه المواد بما في ذلك MAB وMAXو MXene ، في سياق امتصاص الملكيت الأخضر. أظهرت دراسات الامتزاز كفاءتها الملحوظة في امتصاص الملكيت الأخضر تتفق متساوي الحرارة الحركية والامتزازية للملكيت الأخضر بشكل جيد مع نموذج الرتبة الثانية ونماذج فروندليتش.

الكلمات المفتاحية: مركبMAX، مركب MAB، MXenes، الامتزاز، طريقة MS^3، الامتزاز.

ABSTRACT

The major emphasis of this thesis is the synthesis, characterization, and use of certain ternary ceramics, especially the MAX and MAB phases, as well as their related two-dimensional MXenes, for Malachite Green adsorption. To achieve this, the MAB and MAX phases were synthesized through the employment of the MS^3 method. The influence of a Sn additive and salts was explored in the case of Fe_2AlB_2 and Cr_2AlC. The ensuing powders underwent scrutiny using techniques such as X-ray diffraction XRD, Scanning Electron Microscopy SEM, thermogravimetric analysis (TGA) and differential thermal analysis (DTA). The outcomes demonstrated that both Fe_2AlB_2 and Cr_2AlC could be obtained with Sn Additive and KCl salt with high purity at 1000°C for 1 hour.

The production of MXenes is accomplished by removing the Al element from their MAX phase via a chemical etching procedure. The resultant powders were evaluated using X-ray diffraction (XRD) and Brunauer-Emmett-Teller (BET) analyzes.

The last section of the study focuses on the practical use of these materials, which include MAX, MAB and MXenes, in batch adsorption. Adsorption experiments found that they were quite effective at absorbing Malachite Green., the kinetics and adsorption isotherms of Malachite Green agree well with the pseudo-second order and Freundlich models.

Keywords: MAX phase, MAB phase, MXenes, Synthesis, MS^3 method, Adsorption, malachite Green.

Résumé

Le principal objectif de cette thèse est la synthèse, la caractérisation et l'utilisation de certaines céramiques ternaires, en particulier les phases MAX et MAB, ainsi que leurs MXènes bidimensionnels associés, dans l'adsorption du vert malachite. Pour y parvenir, les phases MAB et MAX ont été synthétisées grâce à l'emploi de la méthode MS^3. L'influence d'un additif Sn et de sels a été explorée dans le cas de Fe_2AlB_2 et Cr_2AlC. Les poudres résultantes ont été examinées à l'aide de techniques telles que la diffraction des rayons DRX, la microscopie électronique à balayage MEB, l'analyse thermogravimétrique (ATG) et l'analyse thermique différentielle (ATD). Les résultats ont démontré que Fe_2AlB_2 et Cr_2AlC pouvaient être obtenus avec l'additif Sn et le sel KCl de haute pureté à 1000 °C pendant 1 heure.

La production de MXènes est réalisée en supprimant l'élément Al de leur phase MAX via une procédure de gravure chimique. Les poudres résultantes ont été évaluées par diffraction des rayons X (DRX) et Brunauer-Emmett-Teller (BET).

La dernière section de l'étude se concentre sur l'utilisation pratique de ces matériaux, qui comprennent MAX, MAB et MXenes dans adsorption du vert malachite. Les expériences d'adsorption ont montré qu'ils étaient très efficaces pour absorber le vert malachite, la cinétique et les isothermes d'adsorption du vert malachite s'accordent bien avec les modèles de pseudo-second ordre et de Freundlich.

Mots clés : Phase MAX, Phase MAB, MXènes, Synthèse, Méthode MS^3, Adsorption, Vert malachite.

DEDICATIONS

To my beloved son Elhadi Laith and my husband Ahmed Hadji, you both gave a different meaning of my life.

To my dear parents

To my dear brothers

To all my family

To my dear friends

Acknowledgements

First and foremost, I express my gratitude to Almighty Allah for granting me the health and determination to successfully complete this doctoral thesis.

I wish to extend my heartfelt appreciation to my Thesis Advisors, Professor Mohamed KREA and my co-promoter Pr. Omar BOURAS, for their invaluable guidance, support, and encouragement throughout these years of study and research. Their unwavering presence and dedication to our growth, coupled with their willingness to share their experience, have been truly remarkable. I am eternally grateful for the trust and interest they have shown in me during this period.

I would like to extend my heartfelt gratitude to Professor Mohamed HADJI, the director of the Laboratory 'Etudes et Recherche En Technologies Industrielle' (LERTI), University of Saad Dahleb Blida I regard him as my third thesis supervisor. I offer my sincere thanks for his kindness, as well as for the meaningful scientific interactions, I deeply appreciate the warm reception that I received in the laboratory and the continuous support, guidance, and valuable insights that Professor Mohamed HADJI generously provided.

A special thank you to the LERTI laboratory team Dr. Abbedesbour BENOMAR, Dr. Nabil CHIKER, Dr. Youcef HADJI, Dr. Adel HADDAD, Dr. Ahmed HADJI, Koceila AKHMOUM, Billel HAMZAOUI, Fouad BERBER, Salim KHALOUF and Merouane TOUATI from laboratory "Eau Environnement et Développement Durable". Without you no test would have been interpreted correctly.

I want to express my heartfelt gratitude to both my brother Dr. Abbedessabour Benomar and my husband Dr. Ahmed HADJI for their unwavering support throughout my doctoral thesis journey. My brother's assistance in interpreting results and guiding me through laboratory experiments was invaluable. His dedication truly made a difference. Equally, I'm immensely thankful to my husband for his constant moral support. His belief in me kept me going, even during the toughest moments. Their combined encouragement and help were instrumental in my success and I am truly blessed to have them by my side.

I extend my heartfelt gratitude to my beloved parents, the guiding lights of my life, for their endless affection. I am also deeply thankful to my brother Abderahmane for his

unwavering encouragement and sacrifices, which have sowed hope within me. May they find in these words the sincerest expression of my appreciation.

I would like to express my sincere gratitude to the jurys Pr. Nadiji MOULAI-MOSTEFA, Dr. Razika KHELLADI, Dr. Aziz SERAI, Dr. Hocine BOUTOUMI, and Dr. Adel HADDAD for the honor they have bestowed upon me by evaluating my thesis. Their expertise, commitment, and time devoted to reviewing my work are greatly appreciated. Their feedback and suggestions have been invaluable in improving this work. I am grateful for this opportunity that has allowed me to present my research to a panel of experts.

CONTENT

CONTENT 7

GENERAL INTRODUCTION 1

CHAPTER 1 4

1. MAX AND MAB PHASES 4

1.1 INTRODUCTION 4
1.2 MAX PHASES 5
1.2.1 History and discovery: 5
1.2.2 Crystalline structure of the MAX phases: 6
1.2.2.1 Atomic bonds: 6
1.2.3 Properties of the MAX phase 7
1.2.3.1 Elastic properties of the MAX phases: 7
1.2.3.2 Nonlinear elastic behavior 9
1.2.3.3 Mechanical behavior and deformation mechanisms 10
1.2.8.1 Mechanical properties of MAX phases: 11
1.2.8.2 Thermal choc resistance: 13
1.2.8.3 Oxidation resistance property 14
I.1.4 SOLID SOLUTIONS OF MAX PHASES: 15
1.3 MAB PHASES: 17
1.3.1 Crystalline structure of MAB phases: 17
1.3.2 Microstructure of MAB phases: 19
1.4 PROPERTIES OF MAB PHASES: 20
1.4.1 Elastic properties of MAB phases 20
1.4.2 Oxidation resistance of the MAB phases: 21
1.4.3 Thermal choc resistance: 22
1.4.4 Magnetocaloric properties: 23
1.5 CRACK HEALING BEHAVIOR OF MAX AND MAB PHASES: 24
1.5.1 Crack healing behavior of MAX phases and their composites: *25*
1.6 SYNTHESIS OF MAX AND MAB PHASES 27
1.6.1 Pressureless sintering method. 27
1.6.2 Molten salt assisted method. 28
1.6.3 molten salt shielded synthesis/sintering (MS^3) 28
1.7 APPLICATION OF THE MAX AND MAB PHASES IN THE ENVIRONMENTAL FIELD 30
1.8 SUMMARY: 32

2. CHAPTER 2 FROM MAX TO MXENES 33

2.1 INTRODUCTION 33
2.2 SYNTHESIS OF MXENES 33
2.2.1 $Ti_3C_2T_x$ MXene 35
2.2.2 Cr_2CT_x MXene 37
2.3 PROPERTIES OF MXENES 39
2.3.1 Chemical properties 39
2.3.2 Mechanical properties 40
2.3.3 Electronic properties 41
2.4 APPLICATION OF MXENES 42
2.4.1 MXenes for environmental applications 43
2.4.1.1 Membrane uses of MXenes 43
2.4.1.2 MXenes for Photocatalytic Applications 44

2.4.1.3 MXenes as adsorbents 45
2.4.1.4 Removal of inorganic contaminants by MXenes 46
2.4.1.5 Adsorption of organic pollutants 48
2.4.2 Energy Applications of MXenes *50*
2.4.2.1 Batteries 50
2.4.2.2 Super Capacitor 52
2.4.2.3 Electromagnetic Interference Protection System 53
2.5 SUMMARY: 53

3. CHAPTER 3 : MATERIALS AND METHODS 54

3.1 CHEMICAL PRODUCTS 54
3.2 SYNTHESIS OF MAX AND MAB PHASES 54
3.3 INITIAL MIXTURE POWDERS COMPOSITION 56
3.4 PREPARATION OF MXENES 57
3.4.1 Synthesis of Cr_2CTx 57
3.4.2 Synthesis of Ti_3C_2Tx 57
3.5 CHARACTERIZATIONS OF MXENE, MAX AND MAB PHASE 58
3.5.1 X-Ray Diffraction (XRD) 58
3.5.2 Scanning electron microscope 58
3.5.3 Thermogravimetric and differential thermal analysis (TGA), (DTA). 58
3.5.4 BET analysis 58
3.5.5 Determination pf pH_{pzc} 59
3.6 SORPTION OF MALACHITE GREEN 61
3.6.1 Preparation of the calibration curve of MG. 61
3.6.2 UV-Vis absorption of MG 62
3.6.3 Sorption kinetics 62
3.6.4 Effect of pH 62
3.6.5 Effect of initial concentration 63
3.6.6 Sorption Isotherms 63
3.6.7 Adsorption Modeling 63
3.6.7.1 Modeling Adsorption Kinetics 63
3.6.7.2 Adsorption Equilibrium Modeling 64
a) Langmuir Adsorption Isotherm 65
b) Freundlich model 65

4. CHAPTER 4 : RESULTS AND DISCUSSION 67

4.1 SYNTHESIS OF MAB AND MAX PHASES 67
4.1.1 Synthesis *of MAB phases* *67*
4.1.2 Characterization of MAB phases 68
4.1.2.1 X-Ray Diffraction (XRD) 68
4.1.2.2 Thermogravimetric and differential thermal analysis (TGA) ,(DTA) 71
4.1.2.3 Scanning electron microscopy of MAB phase 73
4.1.5 Synthesis of MAX phases 77
4.1.5.1 Synthesis of Cr_2AlC 77
4.1.6 Characterization of MAX phases with X-Ray Diffraction 78
4.1.6.1 Synthesis of Cr_2AlC with KCl shielding 78
4.1.6.2 Synthesis of Cr_2AlC with NaCl shielding 79
4.1.6.3 Synthesis of Cr_2AlC with KBr shielding 80
4.1.6.4 Synthesis of Cr_2AlC with NaBr shielding 80
4.2 SYNTHESIS OF TWO-DIMENSIONAL MATERIAL MXENES 84
4.2.1 Synthesis of two-dimensional Cr_2CTx 84
4.2.2 Synthesis of two-dimensional Ti_3C_2Tx 85
4.3 ADSORPTION STUDIES 85
4.3.1 BET Analysis 85
4.3.2 Adsorption of MG in batch mode 86
4.3.2.1 Effect of contact time 87

4.3.2.2 Adsorption kinetics 88
4.3.2.3 Effect of initial pH of solution 90
4.3.2.4 Effect of adsorbent dose 92
4.3.2.5 Isotherm studies 93
4.4 SUMMARY 94
GENERAL CONCLUSIONS **96**
PERSPECTIVE **97**
ACRONYMS LIST **98**
ANNEX 1 **100**
ANNEX 2 **101**
REFERENCES **102**

LIST OF ILLUSTRATIONS, GRAPHICS AND TABLES

Figure I. 1:Number of papers and citations on the MAX phases. ----------5

Figure I. 9 :Crystalline structure of (b) FeB and (d) Fe_2AlB_2 ---------- 19

Figure I. 10: SEM imaging of a Cr_2AlB_2 grain, microstructure of a Mn_2AlB_2 fracture facies ---------- 19

Figure I. 11:SEM micrographs of the fracture surfaces of Fe_2AlB_2 prepared by hot-pressing of 1.1Al/2FeB at 1100 °c for 1 h under 30 MPa In Ar. (a) a low magnification, and (b) a high magnification SEM taken from(a) 20

Figure I.12: (a)Etched microstructure of MoAlB, (b) BSE (Backscattered Secondary Electrons), of the polished surface of MoAlB properties of MAB phases ---------- 20

Figure I. 13: The dependence of the modulus of (a) young € and (b) shear modulus (G) with temperature. ----- 21

Figure I. 14: (a) The progression of the Al_2O_3 oxide layer on the MoAlB surface as a function of time, and (b) X-ray diffraction (XRD) of the layer formed ---------- 22

Figure I. 15 : Comparison of the thermal shock resistance of some MAX and MAB phases with Al_2O_3 . ------- 23

Figure I. 16: (a) SEM image of Ti_3GeC_2 MAX phase oxidized at 900°C for 4h . (b) SEM micrographs of $Ti_2AlC_{0.5}N_{0.5}$ MAX phase oxidized in Air at 1040 °C for 16 h . Cross-Sectional SEM image of a Ti_2AlC sample oxidized in Air at 1100 °C for (c) 16h and (d) 64 h. The uniform layer labeled d in (d) is replaced by striated layers in (c) that are Al_2O_3-Rich (Dark layers)and TiO_2-Rich layers the uniform layer labeled d in (d) is replaced by striated layers in (c) that are Al_2O_3-Rich (Dark layers)and TiO_2-Rich layers . ---------- 25

Figure I. 17: (a) Optical image showing a crack faces both covered by the same Al_2O_3 layer (Black) and the gap center was fully filled by a mixture of Al_2O_3 (Black) and TiO_2 (Large white particles). (b) SEM using Electron Backscatter Diffraction O the Healed-damage zone. ---------- 26

Figure I. 18:Stepwise schematic of the MS^3 process ---------- 29

Figure I. 19: Molten salt shielded synthesis (MS^3) without salt encapsulation in eutectic molten salt ---------- 30

Figure II. 1: Schematic Of MXene Synthesis ---------- 34

Figure II. 2: Lowest-energy atomic configurations during the step-by-step intercalation of HF via the Ti_3AlC_2 edge and extraction of AlF_3: (a) pristine and (b) one, (c) two, (d) three, (e) four, (f) Five, (g) six, and (h) seven HF-intercalated MAX complexes. Atoms at the left edge are fixed and shown here by a shaded region. silver, blue, orange, cyan, and pink balls represent Ti, C, Al, F, And H atoms, respectively ---------- 35

Figure II. 3:Schematic of the etching and delamination process of Mxene from MAX phase ---------- 36

Figure II. 4: Schematic representation of the synthesis of Cr_2CT_x nanosheets . ---------- 38

Figure II. 5: Schematic diagram representing reversible cointercalation of H_2O in $Ti_3C_2T_x$ MXenes having intercalated cation a (denoted as A- $Ti_3C_2T_x$). ---------- 40

Figure II. 6 :Schematic illustrating the use of MXenes ---------- 43

Figure II. 10: (a) Schematic illustration of the formation of the $Ti_3C_2(O_2H_{22m}pb_m)$ structure from $Ti_3C_2(OH)_2$ to $Ti_3C_2(O_2H_{22m}pb_m)$; (b) Top-view of the $Ti_3C_2(O_2H_{22m}pb_m)$ structure when the Pb coverage is 1/9 Ml.– represent the different atom sites of the hydroxy.---------- 46

Figure II. 11: Illustration of the removal mechanism of Cr(Vi) by the $Ti_3C_2T_x$ nanosheets ---------- 47

Figure II. 7: Charge-discharge curves of non-delaminated Ti_2CT_x synthesized by HF treatment at C/10 rate in a 1 M Lipf6/Ec-Dec electrolyte.---------- 51

Figure III.1: Step used in MAX and MAB phases synthesis. (a) Compact powder of MAX and MAB phases,(b) Encapsulated compact powder with salt (KCl or KBr, NaBr and NaCl), (c) Salt bed in cylindrical alumina crucible.----------55

Figure III.2: Schematic view of the MAX and MAB synthesis by the Molten Salt Shielded Synthesis "MS^3" process using KBr or KCl, NaCl, NaBr.----------56

Figure III.3:The proposed schematic illustrates the etching process from Cr_2AlC MAX phase to Cr_2CT_x MXene.----------57

Figure III.4: Structure of Malachite Green used.----------61

Figure IV. 1: Digital photographs showing (a): Sample Fe_2AlB_2 taken from the oven ,(b): The sample of Fe_2AlB_2 after salt removal.----------68

Figure IV. 2: XRD patterns of (a) 2Fe/2Al/2B/0.2Sn mixture and (b) 2Fe/2Al/2B mixture, synthesized by the MS^3 process using KBr salt at 900, 1000, 1100, and 1200 °C, for 1h synthesis time.----------70

Figure IV. 3 DTA curves of (a) 2Fe/2Al/2B/0.2Sn, (b) 2Fe/2Al/2B initial powder mixtures. TGA Curves of (C) 2Fe/2Al/2B/0.2Sn, and (d) 2Fe/2Al/2B initial powder mixtures.---------- 73

Figure IV. 4 :SEM micrographs of synthesized Fe_2AlB_2 powder at 1200 °C prepared starting from 2Fe/2Al/2B, without Sn additive. SEM-EDS elemental mapping of (b) Iron, (c) Aluminum and (d) Boron.---------- 74

Figure IV. 5:SEM micrographs of synthesized Fe_2AlB_2 with Sn additive at 1000 °C. (b) higher magnification of inset in (a). SEM-EDS elemental mapping of: (c) Boron, (d) Iron, € Aluminum, and (f) Tin. ---------- 75

Figure IV. 6: SEM micrographs of synthesized Fe_2AlB_2 with Sn additive at 1000 °C. SEM-EDS elemental mapping of: (b) Aluminum, (c) Iron, (d) Tin, and (e) Boron. ---------- 76

Figure IV. 7: digital photographs showing (a),(c),(e) : Sample of Cr_2AlC taken from the oven with KCl ,KBr and NaCl salt respectively ,(b),(d),(f) : the sample of Cr_2AlC after salt removal. ---------- 77

Figure IV. 8: X-RAY diffraction analysis of the synthesized Cr_2AlC at various temperature 900 °C To 1200 °C for 1h with molar ratio of 2Cr/1.2Al/1C. ---------- 78

Figure IV. 9 : XRD patterns of 2Cr/Al/C, synthesized by the MS^3 process using NaCl salt at 900, 1000, 1100, and 1200 °C, for 1h synthesis time.---------- 79

Figure IV. 10: XRD patterns of 2Cr/Al/C, synthesized by the MS^3 process using KBr salt at 900, 1000, 1100, And 1200 °C, for 1h synthesis time.---------- 80

Figure IV. 11: XRD patterns of 2Cr/Al/C, synthesized by the MS^3 process using NaBr salt at 900, 1000, 1100, and 1200 °C, for 1h synthesis time.---------- 81

Figure IV. 12: (a) SEM micrographs of synthesized Cr_2AlC with KCl salt At 1000 °C, b) Higher magnification. SEM-EDS elemental mapping of: (c) Chromium, (d) Aluminum, and (e) Carbon.---------- 83

Figure IV. 13 : XRD patterns of the MAX (Cr_2AlC) and its MXene (Cr_2CT_x).---------- 84

Figure IV. 14 :XRD patterns of the MAX (Ti_3AlC_2) and its MXene ($Ti_3C_2T_X$).---------- 85

Figure IV. 15 : Nitrogen Adsorption–Desorption isotherms of Cr_2AlC, Cr_2CT_x and $Ti_3C_2T_x$ samples.---------- 86

Figure IV. 16: Kinetics of Adsorption of MG on different MAX, MAB and MXenes phases. ---------- 87

Figure IV. 17:Adsorption kinetics of MG on MAB, MAX phases and MXenes . ---------- 89

Figure IV. 18: Effect of pH on Adsorption of MG onto MXenes, MAX and MAB phases.---------- 91

Figure IV. 19 : Effect of adsorbent dose on the Adsorption of MG at pH=6. ---------- 92

Figure IV. 20: Adsorption isotherms of MG onto MXenes , MAB and MAX phases.---------- 93

Table I. 1: Elastic properties of MAX phases----------8

Table I. 2: Lists the room-temperature mechanical properties of some typical MAX phases ---------- 12

Table I. 3: Single-site solid-solution MAX phases that have been experimentally synthesized---------- 16

Table II. 1:a Summary of various studies on MXene application for dye removal.---------- 49

Table III. 1 : Characteristics of the powders used. ---------- 54

Table III. 2: Proportions used in the initial powder mixtures. ---------- 56

Table IV. 1: Kinetic parameters for second order model. ---------- 89

Table IV. 2: Adsorption isotherm parameters for MG Adsorption onto MXenes ,MAX and MAB phases. ----- 94

GENERAL INTRODUCTION

During the 1960s, the research team led by Jeitschko and Nowotny unveiled a variety of novel phases containing nitrogen (N), carbon (C), and boron (B). These phases referred to as "H phases" or "HÄGG" phases[1], had been unnoticed until Barsoum from Drexel University illuminated their distinctive characteristics, later termed "MAX phases" [2,3]. MAX phases function as materials that bridge the divide between ceramics and metals. They comprise ternary carbides or nitrides, arranged in nano-lamellar structures, characterized by the general chemical formula $M_{n+1}AX_n$. Here, M represents a transition metal, A denotes an element from group IIIA or IVA of the periodic table, and X stands for either carbon (C) or nitrogen (N). Similar to metals, they possess machinability and excel as conductors of heat and electricity. These phases also exhibit refractory traits, high rigidity, and resistance to oxidation. Their amalgamation of ionic and covalent attributes classifies them as ceramics [4].

Among the MAX phases, one notable example is the Cr_2AlC ternary carbide, a material displaying a compelling combination of properties. It demonstrates high strength while maintaining a degree of ductility. It also functions as a proficient electrical and thermal conductor. Thanks to its resistance to oxidation and corrosion, along with its remarkable photocatalytic activity and resilience to thermal shock, it proves suitable for high-temperature applications and aggressive environments [5–8]. A distinctive aspect is its ease of machinability, setting it apart from conventional ceramics.

Following the achievements of MAX phases, a novel type of nanolaminate ternary boride called MAB phases (with B as boron) was successfully synthesized by Ade & Hillebrecht in 2015 [9]. MAB phases have garnered increasing attention due to their unique properties. For instance, Fe_2AlB_2 possesses a layered orthorhombic crystal structure with the space group Cmmm [9]. This structure alternates two layers of Fe_2B_2 slabs with layers of Al atoms, imparting damage tolerance and machinability akin to MAX phases [10]. Furthermore, Fe_2AlB_2 comprises elements abundant in the Earth's crust, and it exhibits electrical conductivity, magnetic properties, and a magnetocaloric effect [11–13]. This position is as a potential candidate for applications in magnetic cooling and magnetothermal-based energy harvesting.

Nevertheless, the synthesis of Cr_2AlC and Fe_2AlB_2 has not been as extensively studied as that of other MAX phases (e.g., Ti_3AlC_2, Ti_2AlC_2). Particularly for Fe_2AlB_2, challenges like prolonged annealing and difficulties in achieving a pure Fe_2AlB_2 phase have been prominent issues. Therefore, finding a cost-effective method to synthesize pure Fe_2AlB_2 and Cr_2AlC powders is crucial. Existing reports [12,14–17] on synthesizing Cr_2AlC and Fe_2AlB_2 typically involve very high temperatures, leading to elevated costs for Fe_2AlB_2 and Cr_2AlC production. The molten salt shielding technique, which permits the synthesis of porous materials or powders at relatively low temperatures, may be a viable option. This technique employs salt not only as a reaction medium but also as a means of protecting materials from oxidation during processing in an open-air atmosphere [18].

MXenes, a family of two-dimensional (2D) transition metal carbides and carbonitrides prepared from MAX phase precursors by selective etching of the A-site element [19], Today after a decade of their discovery, MXenes were applied in different areas, including energy storage, catalysis [20], sensing [20], and adsorption [21,22] MXenes have many exceptional properties, including the 2D shape, highly negative charge, and activation groups abundance.

The primary purpose of this thesis is to synthesize the Cr_2AlC and Fe_2AlB_2 phases using the Molten Salt Shielded Synthesis technique (MS^3) by tuning additives and preparation parameters in order to achieve very pure phases, lower elaboration temperatures and reduce synthesis time. The second step consists of to remove the element Al from successfully synthesized MAX and MAB phases, using chemical etching to produce the two-dimensional MXene material. The final step is to evaluate these materials for their capability to adsorb malachite green.

The outline of this manuscript is described briefly below:

- Chapter 1 focuses on the literature review of MAX and MAB phases, delving into their structures, properties, and synthesis methods using the MS3 technique. Additionally, it explores their applications in the environmental domain.
- Chapter 2 centers on the literature review of the two-dimensional material MXene, providing a comprehensive exploration of the synthesis methods for Ti_3C_2Tx and Cr_2CT_x, as well as their properties. Furthermore, this chapter explores their diverse applications across various domains.
- Chapter 3 details the experimental section, encompassing the following aspects:

- Preparation protocols for the MAB phase (Fe_2AlB_2) and the MAX phase (Cr_2AlC) by molten salt shielded synthesis, with a study of the influence of different salts on Cr_2AlC and Sn additive for Fe_2AlB_2 preparation.
- Preparation protocols for the two-dimensional materials Cr_2CTx and $Ti_3C_2T_x$.
- Characterization protocols involving physico-chemical analyses of the materials.
- Utilization of these materials in tests for adsorption kinetics and isotherms of malachite green (MG) in batch systems.

- Chapter 4: Present the various achieved results and their corresponding discussions.

Chapter 1

1. MAX and MAB phases

1.1 Introduction

In the last decade, ternary ceramics have attracted a lot of attention of the researcher's community, due to their high resistance to oxidation, wear, mechanical properties, and chemical inertness. Among these ceramics, we find the MAX and MAB phases family. These ternary ceramics are nano lamellar ceramics where some possess some of the best properties of metals and ceramics [23].

MAX phases are nitrides or carbides with a chemical formula of $M_{n+1}AX_n$, where M is a transition metal, A: usually IIIA and IVA group element in the periodic table, and X is C or N. Recently, boron joined this family, where two phases Hf_2TeB [24] and Ti_2LnB_2 [25] have been experimentally synthesized. These new boron-containing MAX phases are called MAX phases borides to avoid confusion with the MAB phases. The difference between MAX phases and MAB phases is by their chemical formula, and space group (hexagonal crystalline structure P6/3mmc).

On the other hand, MAB phases are ternary nano-lamellar borides, where their renewed interest go back to 2016 S. Kota et al.[14], where the Drexel research group led by Pr. M. W. Barsoum, have reported the only boride, up to date, that forms a protective alumina layer when exposed to high temperatures at open air [26]. Making MoAlB phase is the only boride that sustains high temperature applications. The MAB phases discovery is still in progress; thus, their chemical formula and definition is frequently changing. The chemical formulas of experimentally synthesized MAB phases are MAB, M_2AB_2, M_3AB_2, M_4AB_4, M_6AB_3, and M_5AB_2. Where M is a transition metal, A is Al and Si, and B is boron [27].

1.2 MAX phases

1.2.1 History and discovery

MAX stages are divided into two chapters. Its first chapter is set in the 1960s, when Jeitchko and Nowotny synthesized novel ternary phases known as Hagg or H phases [28,29]. Meanwhile, they received insufficient attention from the scientific community at the time. The first report on the H phases came in 1993, when a group from Poland identified some similarities between Ti_3SiC_2 and metals [30]. It's when a group from Drexel University, USA, Pr. M.W. Barsoum and his co-workers (1997), showed the great potential of these phases that a renewed interest was triggered [31–33]. Since then, the term "MAX phases" has appeared in more than 400.000 research publications.

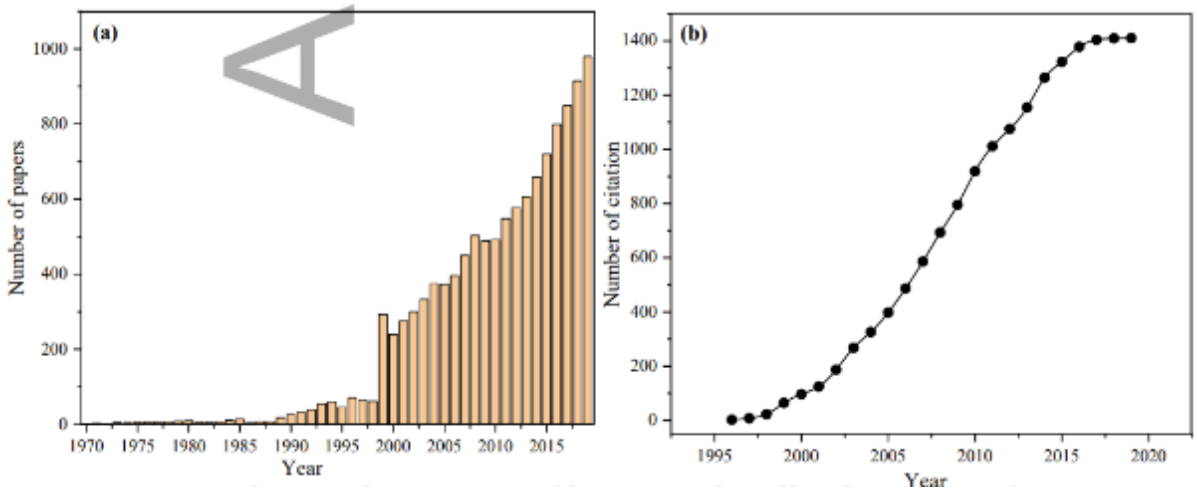


Figure I. 1:Number of papers and citations on the MAX phases[34].

Among the Hagg phases, it exists one boride, MoAlB. The synthesis and characterization of this phase in a bulk form were done at Drexel University in 2016 [26]. The MoAlB showed some characteristics similar to MAX phases, except for machinability. That phase attracted interest because up to date it's the only ternary boride that forms a protective oxide layer in the 1000 -1400°C temperature range [35,36]. Other ternary borides were discovered and synthesized in a bulk form since then, like the Mn_2AlB_2 (2019) [37], Fe_2AlB_2 (2018) [38], Cr_2AlB_2 (2018) [39], WAlB (2023) [40,41], M_5SiB_2 (M=Mn, V, Mo, Fe, and Cr; 2021-2023) [42–44]. These phases followed their MAX phases sisters and they're called MAB phases.

1.2.2 Crystalline structure of the MAX phases

The $M_{n+1}AX_n$ phases are lamellar materials with a hexagonal crystalline structure within $P_{63/mmc}$ space group. Figure I.2 shows the three structures possible of the MAX phases where n= 1, 2, or 3. The atoms of the element M (in red) form octahedral groups of M_6X, where X atoms occupy its center. These groups are separated by a mono layer of A element. The stacking of these layers constitutes their lamellar structure as shown in figure I.2b [45,46].

1.2.2.1 Atomic bonds:

MAX phases have three types of atomic bonds: covalent, ionic and metallic bonds. The difference in structure, density and bonds make the difference in certain properties such as rigidity, electrical and thermal conductivity, hardness, corrosion resistance, etc.

- Covalent bonds: it's the strongest bond in the crystalline structure of the MAX phases, it takes place between M and X elements.
- Ionic bonds: Like in titanium carbide and titanium nitride, it has been proved that it is impossible to find a ceramic that possesses only covalent bonds. M-X could also be ionic. However, in many physical reports, M-A is considered always and the most dominant source of ionic bonds in MAX phases. It must be noted that M-A bonds are thirty-three weaker bonds compared to covalent M-X bonds. These bonds make MAX phases highly anisotropic materials.
- Metallic bonds: M-M bonding represents metallic bonds which provide to the MAX phases their electrical and thermal properties [45,46].

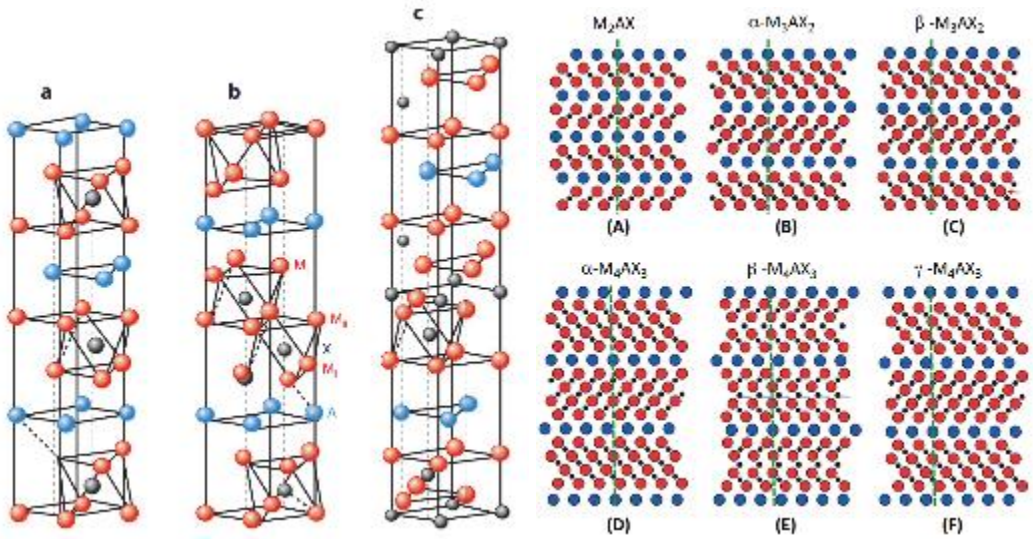


Figure I. 2 : (a) MAX phase unit cells: (a) 211, (b) 312, and (c) 413 phases. (b) Schematics of the ð1120Þ planes in (A) M_2AX; (B) a-M_3AX_2; (C) b-M_3AX_2; (D) a-M_4AX_3; (E) b-M_4AX_3 and (F) g-M_4AX_3 phases. Dashed vertical lines are guides for the eye [47].

1.2.3 Properties of the MAX phase

The research on the MAX and MAB phases reports are highly cited due to their interesting properties [27]. They present a good combination of properties such as high Young's modulus [48,49], an electrical conductivity that is close to the corresponding M element [46,50], good thermal choc resistance [51], damage tolerance [49], oxidation resistant at ambient and some at high temperatures, high damping properties [52–56], low friction behavior at high and at ambient temperatures, and good corrosion resistance [57–59]. Some distinguished properties have put these phases at the front line like crack-healing behavior (Cr_2AlC, Ti_2SnC, Ti_2AlC, MoAlB) [60–64], good neutron radiation damage response [65], and unexpectedly, recently they showed a capability of dye adsorption and degradation in water treatment application [66]. On top of it all, MAX phases are also machinable, and simply by a hacksaw [45].

1.2.3.1 Elastic properties of the MAX phases

The MAX phases, as shown in Table I.1 and Figure I.3, are known to be elastically stiff. They exhibit high specific stiffness values due to their combination of stiffness and relatively low densities, which range from approximately 4-5 g/cm^3 (as listed in Table I.1). For example, Ti_3SiC_2 has a specific stiffness comparable to Si_3N_4 and is roughly three times that of Ti.

Poisson's ratios for the MAX phases are around 0.2, which is lower than that of Ti (0.3) and closer to the value of near-stoichiometric TiC (0.19). One of the notable characteristics of the MAX phases is their machinability. Unlike other materials with high stiffness, the MAX phases can be easily machined using simple tools. Additionally, their excellent electrical conductivities allow for machining using electron discharge methods. This makes them highly attractive for various applications where both stiffness and machinability are important factors to consider [67].

Table I. 1: Elastic properties of MAX phases [45].

SOLID	DENSITY (G cm^{-3})	G(GPa)	E(GPa)	*V*	B‡ (GPa)	B* (GPa)
Ti_2AlC	4.1	118	277	0.19	144	186
$Ti_2AlC_{0.5}N_{0.5}$	4.2	123	290	0.18		
V_2AlC	4.81	116	235	0.20	138	166
Cr_2AlC	5.24	102	245	0.20	138	166
	5.1	116	288			
Nb_2AlC	6.34	117	286	0.21	165	208
Ta_2AlC	11.46	121	292			251
Ti_3GeC_2	5.02	142	340-347	0.19	169	179
TI_3ALC_2	4.2	124	297	0.20	165	226 ±3
$Ti_3(Si,Ge)C_2$	4.35	136.8	322	0.18	166	183±4
Ti_3AlCN	4.5	137	330	0.21		219±4
Cr_2GeC	6.88	80	245	0.29	165	226±3
						169±2
V_2GeC						165±2
Ti_2SC		125	290	0.16	145	191±3
Nb_2SnC			216			180±5
Hf_2SnC			237			169±4
Nb_2AsC	8.05					
Nb_4AlC_3	6.98	127	306			
B-Ta_4AlC_3	13.2	132	324			
Ti_4AlN_3	4.7	127	310	0.22	185	216
$TiC_{0.96}$	4.93	205	500	0.19	272	
Zr_2SC	6.20					186
Ti_3SiC_2	4.52	193	343-339	0.20	190	206
Zr_2SnC			178			

B∗ : bulk moduli values measured directly in an anvil cell

B‡ : bulk moduli values calculated from the shear and longitudinal sound velocities.

In general, MAX phases that contain In, Pb, and Sn as A-group elements tend to have lower stiffness compared to those composed of lighter A-group elements. as shown in Figure

I.3. The presence of heavier A-group elements, such as In, Pb, and Sn, can result in reduced stiffness in MAX phases [68].

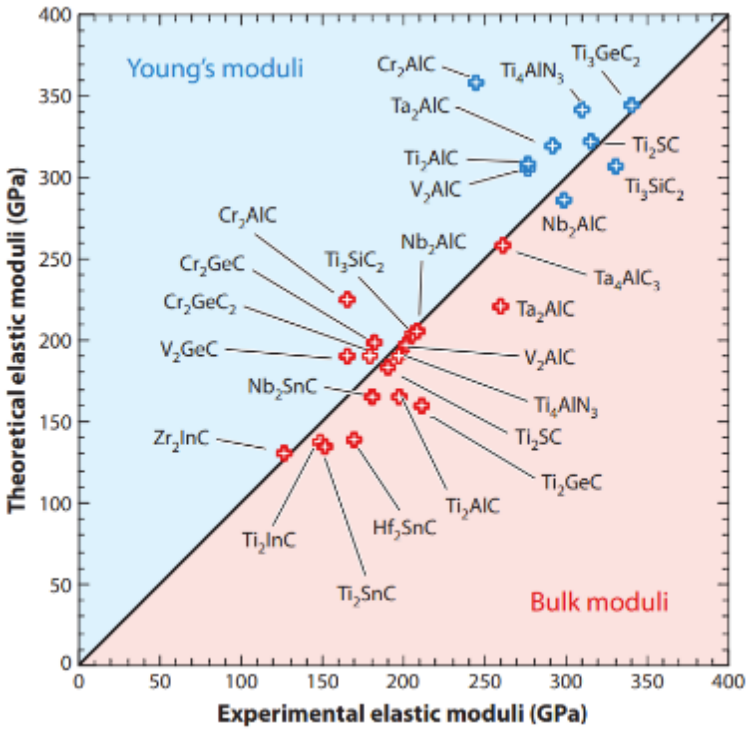


Figure I. 3: Experimental and theoretical (a) bulk moduli B (red) and (b) Young's moduli E (blue) of select MAX phases [67].

1.2.3.2 Nonlinear elastic behavior

One of the most intriguing aspects of MAX phases is their nonlinear, hysteretic, elastic behavior, which is unusual for materials with high stiffness. When subjected to cyclic loading in compression [69] or tension [70], MAX phases exhibit spontaneously reversible hysteretic loops, and the shape and size of these loops strongly depend on the grain size, as shown in Figure I.4 This unique hysteretic behavior in MAX phases adds to their intriguing mechanical properties and makes them distinctive among other materials with high stiffness [67].

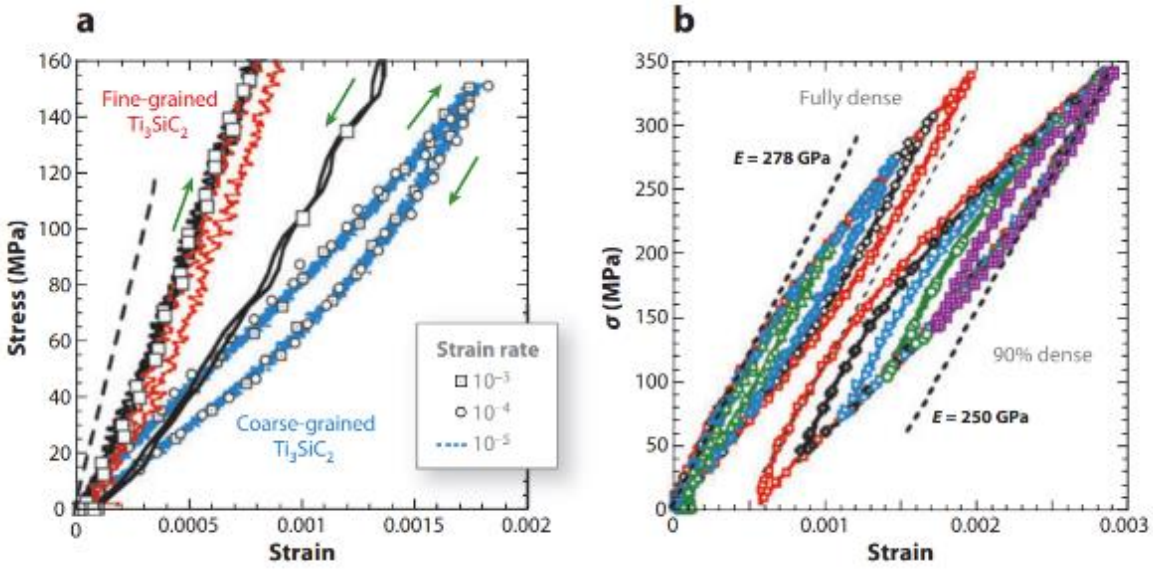


Figure I. 4 : Typical cyclic compressive reversible stress-strain loops. (a) Ti_3SiC_2. (b) Ti_2AlC_2 [71].

Notably, the results show that the 10% porous Ti_2AlC dissipates more energy per unit volume on an absolute scale per cycle compared to its fully dense counterpart.

1.2.3.3 Mechanical behavior and deformation mechanisms

The combination of high stiffness, high toughness, and unusual nonlinear elastic behavior makes MAX phases attractive for a wide range of applications, including in aerospace, energy, electronics, and other fields.

The mechanical behavior and deformation mechanisms of MAX phases are complex and intriguing, characterized by their unique combination of high stiffness [72], high toughness [73], and unusual nonlinear elastic behavior [67]. MAX phases exhibit a range of deformation mechanisms depending on the loading conditions, temperature, grain size, and other factors. of the layered solids, including MAX phases, mica, ice, and graphite, are plastically anisotropic materials due to their layered crystal structure in polycrystalline samples of such materials, favorably oriented or "soft" grains may deform by glide of basal plane dislocations, transferring the load to "hard" grains that are not favorably oriented to the applied stress [74]. The plastic anisotropy of layered solids can also result in the formation of kink bands (KBs) during deformation. Kink bands are regions of localized plastic deformation that form along specific crystallographic directions, typically perpendicular to the applied stress [67]. These KBs can be observed at different length scales, as shown in Figure I.5 in typical micrographs. The presence of KBs and the uneven distribution of plastic deformation among grains due to plastic

anisotropy can have important consequences for the mechanical behavior of layered solids. They can affect the overall strength, ductility, and toughness of the material, as well as influence its response to cyclic loading, fatigue, and other mechanical properties. Understanding the formation and behavior of KBs and the effect of plastic anisotropy is crucial for predicting and optimizing the mechanical behavior of layered solids, including MAX phases [75].

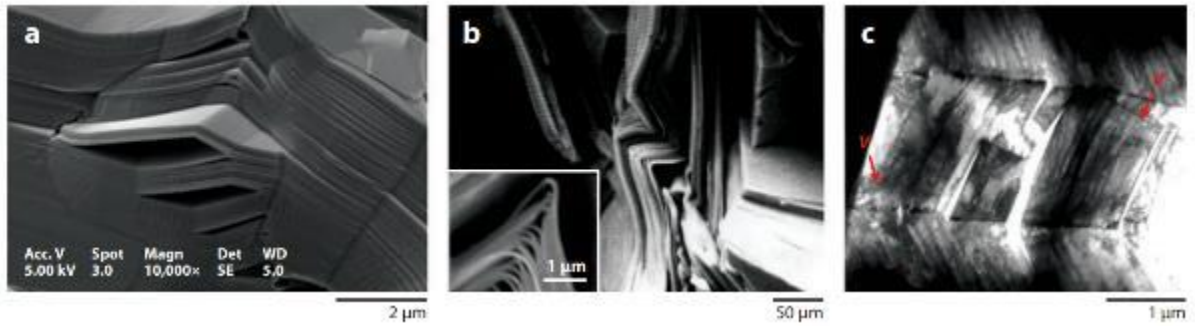


Figure I. 5: Typical examples of the nanolaminated nature of the MAX phases at different length scales. (a) Scanning electron micrographs of a porous Ti_3SiC_2 sample that failed in compression (b) Typical kinking and delamination observed on fractured surfaces of Ti_3SiC_2 (c) Bright-field transmission electron microscopy image of a kink band with a high misorientation (stovepipe) angle containing delamination cracks. Separate dislocation walls, which are generally normal to the basal planes but are inclined to the kink boundaries [75].

1.2.8.1 Mechanical properties of MAX phases

MAX phases are known for their unique combination of mechanical properties [73,76–79]. Most MAX phases are elastically quite stiff due to their strong covalent bonding, and their density is relatively low, ranging from 4.1 to 5 g/cm^3[80]. This results in high specific stiffness values, which is calculated as the Young's modulus divided by density. For example, the specific stiffness of Ti_2AlC MAX phase is slightly lower than that of Si_3N_4 ceramics, and roughly three times higher than that of Ti metal [80].

Table I. 2 lists the room-temperature mechanical properties of some typical MAX phases. It is worth noting that most MAX phases have relatively low density, except for Ta-containing MAX phases, which have higher densities [67]. In terms of hardness, MAX phases are considered “soft” compared to other ceramics, with hardness values falling in the narrow range of 2-5 GPa [81]. Young’s modulus of MAX phases ranges from 282 GPa to 340 GPa, which is between ceramics, but much higher than most metals and alloy [82]. The flexural strength of MAX phases is relatively low compared to other structural ceramics, ranging from 260 to 480 MPa, but they typically exhibit good crack propagation resistance and high fracture toughness

values of 5.7-7.7 MPa·$m^{1/2}$, which are comparable to those of structural Si_3N_4 ceramics with interlocking microstructure [80].

Table I. 2: Room-temperature mechanical properties of some typical MAX phases [67].

	MICROSTRUCTURE	K_{1C}(MPaM$^{1/2}$)	Đ(MPa)	
Ti_3SiC		7	720	Flexural
	Fine grained	8-9.5	298	Tensile
			1.050	compressive
			600	Flexural
	Coarse grained	8.5-16	180	Tensile
			720	compressive
			350	Flexural
Ti_3AlC_2		6.9	340	Flexural
	Fine grained	7.8	320	Flexural
	Coarse grained	9.5	169	Flexural
			764	compressive
Ti_2AlC		6,5	275	Flexural
			540	compressive
Ti_2AlN			381	compressive
Ti_4AlN			350	Flexural
			475	compressive
$Ti_3Si_{0.95}Al_{0.05}C_2$	Fine grained	6.5	458	Flexural
	Coarse grained	6.7	306	Flexural
Cr_2AlC			378	Flexural
			1.160	compressive
Gr_2GeC			770	compressive
Ta_2AlC		7.7	360	Flexural
			804	compressive
Nb_4AlC_3		7.1	346	Flexural
			515	compressive
B-Ta_4AlC_3		7.7	372	Flexural
			821	compressive
Ti_4AlN_3			350	Flexural
			475	compressive
			450	Flexural
Ti_2SC			1400	compressive
V_2AlC		5.5	475	compressive
			450	Flexural
Ti_2GeC			1900	compressive
Ti_3GeC			1277	compressive

1.2.8.2 Thermal choc resistance

The thermal shock resistance of MAX phases, such as Ti_3SiC_2, is influenced by factors such as grain size and quenching temperature [83]. Coarse-grained Ti_3SiC_2 samples typically show no significant change in post-quenching flexural strength with quench temperature and may even exhibit slightly higher strengths when quenched from higher temperatures, as shown in Figure I.6. On the other hand, fine-grained Ti_3SiC_2 samples generally show a gradual decrease in post-quenching strength over a range of temperatures [84].

Similar behavior has been observed in $Ti_3(Si_xGe_{1-x})C_2$ solid solutions, indicating a nonsusceptibility to thermal shock. However, in some cases, post-quenching flexural strength of coarse-grained $Ti_3(Si_{0.5},Ge_{0.5})C_2$ samples was found to be about 20% higher than that of the as-received sample, as shown in Figure I.6 [84].

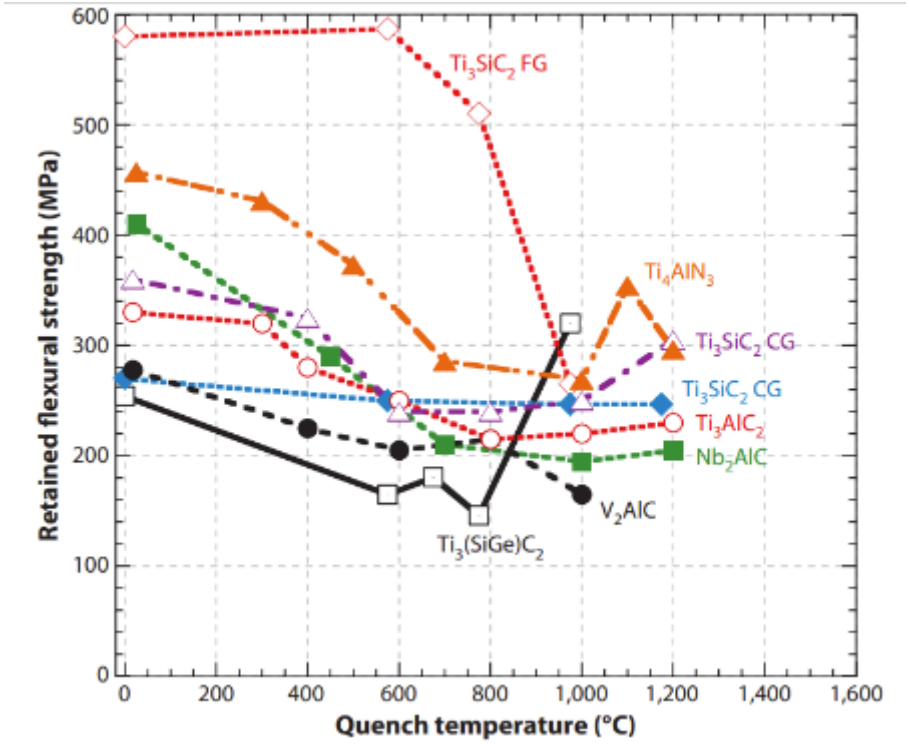


Figure I. 6 : Post quench flexural strength versus quench temperature of select MAX phases [84].

1.2.8.3 Oxidation resistance property

The high-temperature oxidation resistance of Al-containing MAX phases, such as Ti_2AlC, Ti_3AlC_2, V_2AlC and Cr_2AlC is attributed to the diffusion of weakly bonded Al elements to the surface at high temperatures, forming a dense and continuous Al_2O_3 layer on the surface. This Al_2O_3 layer effectively limits the inward diffusion of oxygen ions (O^{2-}) and protects the MAX phase from further oxidation [7].

Several factors influence the oxidation behavior of MAX phases, including oxidation temperature, grain size, and solid solution composition. The weight gain per unit surface area of MAX phases during oxidation typically follows cubic or parabolic kinetics. The formation of a dense and continuous Al_2O_3 layer is typically associated with cubic kinetics, which indicates excellent oxidation resistance [7,85].

The cross-section view of the oxide layer observed by scanning electron microscopy (SEM) on Ti_3AlC_2 samples after oxidation at 800 °C for 24 hours and 500 hours (Figure I.7) shows an increase in the thickness of the oxidized surface layer from approximately 7 μm to 200 μm. The composition of the oxidized layer also changes with oxidation time, with layers of different chemical compositions formed due to the inward diffusion of O^{2-} and outward diffusion of Ti^{4+} and Al^{3+} during oxidation [86].

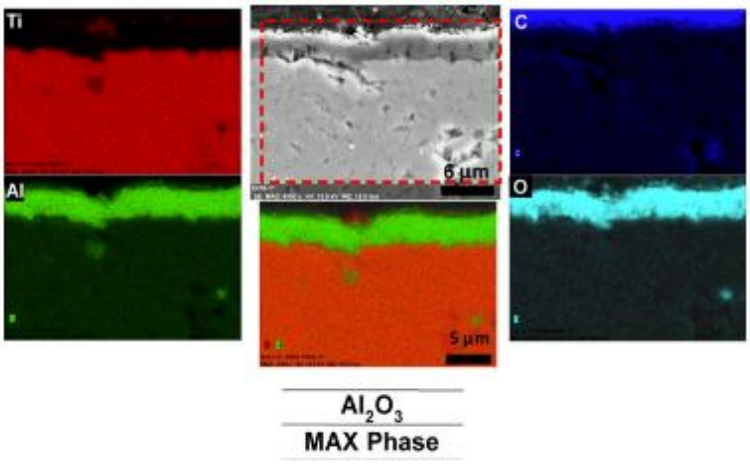


Figure I. 7: ross-section view of the oxide layer observed by SEM on the Ti_3AlC_2 SPSed specimen oxidized during 1000 h at 1000°C. Ti, Al, C, and O corresponding EDXS maps of the oxide scale [86].

I.1.4 Solid solutions of MAX phases

The versatility of MAX phases is greatly increased by the ability to synthesize solid solutions on the M, A, or X sites. Some of these solid solutions were first synthesized in early work by Schuster and colleagues, but their synthesis has been further optimized in recent studies. Table I. 3 [87] provides a list of all known single-site quaternary phases, along with the degree of substitution whenever possible. Several strategies have been developed to enhance the diversity of solid solutions in MAX phases including:

Incorporation of small amounts of Fe and Mn into Cr_2AlC, Cr_2GaC, Cr_2GeC, and V_2AlC has led to magnetic properties [88]. For example, microwave synthesis was used to synthesize $(V_{1-x}Fe_x)_2AlC$, and this novel processing method could potentially be applied to incorporate other new elements. These magnetic MAX phases could serve as ideal precursors for the synthesis of magnetic MXenes [89].

Elements such as Au, Bi, and Cu have been incorporated on the A sites of MAX phases such as $(Cr_{1-x}Mn_x)_2AuC$, $Zr_2(Al_{0.4}2Bi_{0.58})C$, and $Ti_3(Al_{1-x}Cu_x)C_2$ [87] respectively, representing some of the newest elements to be incorporated on the A sites. Interestingly, Cu incorporation into Ti_3AlC_2 led to a symmetry reduction from hexagonal P63/mmc to the monoclinic C2/c space group. Similar symmetry reductions were observed for in-plane "ordered" solid solutions such as $(Mo_{2/3}Sc_{1/3})_2AlC$, $(V_{2/3}Zr_{1/3})_2AlC$, $(Mo_{2/3}Y_{1/3})_2AlC$, $(W_{2/3}Sc_{1/3})_2AlC$, and $(Cr_{2/3}Y_{1/3})_2AlC$ i-MAX phases, as discussed later [87–89].

The discovery of hybrid 523-type $(V_{0.5}Cr_{0.5})_5Al_2C_3$ and higher-order 514-type $(Ti_{0.5}Nb_{0.5})_5AlC_4$ represents new MAX phases with unique compositions [90].

In addition to the solid solutions presented in Table I.3, more complex phases with five elements on the M and A sites have been shown to exist in the $(Ti_{0.95}Zr_{0.05})_3(Si_{0.9}Al_{0.1})C_2$ and $(Zr_{0.8}Nb_{0.2})_2(Al_{0.5}Sn_{0.5})C$ systems [87].

It is noteworthy that incorporation of X-site solid solutions in $Ti_2Al(C_x,N_{1-x})_y$ resulted in 20% substoichiometric occupancy on the X sites [91]. Recent studies by Lapauw and colleagues have also shown that solid solutions on the M and A sites are enhanced when the prismatic distortion, given by the dM-M/dM-A ratio (where dM-M is the distance between M atoms and M-A is the distance between M and A atoms), is minimized. This prismatic distortion is minimized when the size of the M and A atoms are comparable [92,93].

Table I. 3 Single-Site Solid-Solution MAX Phases That Have Been Experimentally Synthesized [87].

	M SITE	A SITE	X SITE
211	$(V_{0.96}Mn_{0.04})_2AlC$ $(V_{1-x}Ti_x)_2AlC$ (x = 0.5, 1, 1.5) $(Cr_{1-x}Mn_x)2GeC$ $(Cr_{0.5}Mn_{0.5})_2AuC$ $(Cr_{0.5}Mn_{0.5})_2GaC$ $(Cr_{1-x}Fe_x)_2AlC$ (x < 0.02) $(Cr_{1-x}Mn_x)_2AlC$ (x < 0.1) $(Cr_{1-x}Vx)_2AlC$ (x = 0.5, 1, 1.5) $(Cr_{1-x}Tix)_2AlC$ (x = 0.5, 1.5) $(Cr_{0.5}V0.5)_2GeC$ $(Nb_{1-x}Zr_x)_2AlC$ (0 < x < 1) $(Nb_{1-x}V_x)_2AlC$ (0 < x < 1) $(Nb_{2/3}Sc_{1/3})_2AlC$ $(Ti_{1-x}Nbx)_2AlC$ (0 < x < 1) $(Ti_{1-x}Tax)_2AlC$ (0 < x < 1) $(Ti,Zr)_2InC$ $(Ti,Hf)_2InC$ $(Ti_{1-x}Mo_x)AlC$ (0 < x < 0.2)	$Zr_2(Al_{0.42}Bi_{0.58})C$; x = 0.58 $Cr_2(Al_{0.97}Si_{0.03})C$ $Cr_2(AlxGe_{1-x})C$ $V_2Ga_{1-x}Al_xC$ (0.43 < x < 0.6) $Zr_2(Al_{1-x}Sn_x)C$ (0 < x < 1) $Zr_2(Al_{0.3}Sb_{0.7})C$ $Zr_2(Al_{0.35}Pb_{0.65})C$ $Mo_2(Ga_{0.33}Fe_{0.5}Au_{0.16})C$	$Ti_2Al(C_x,N_{1-x})_y$ (0 < x < 1; y < 0.2)
312	$(Ti_xV_{0.5})_3AlC_2$ (x = 0.5) $(V_{1-x}Cr_x)_3AlC_2$ (x = 0.5) $(Cr_{1-x}Ti_x)_3AlC_2$ $(Zr_{1-x}Ti_x)_3AlC_2$ (0 < x < 1)	$Ti_3Si_xGe_{1-x}C_2$ $Ti_3Si_xGe_{1-x}C_2$ (0 < x < 1) $Ti_3(Si_{1-x}Pd_x)C_2$ $Ti_3Al_{1-x}Sn_xC_2$ (x = 0.2) $Zr_3(Al_{1-x}Si_x)C_2$ $Ti_3(Al_{1-x}Cu_x)C_2$ (0 < x < 0.5) $Ta_3(Al_{1-x}Sn_x)C_2$ (x 0.04)	$Ti_3Al(C_{0.5}N_{0.5})_2$
413	$(Nb_{0.5}V_{0.5})_4AlC_3$ $(Nb_{0.8}Ti_{0.2})_4AlC_3$ $(Nb_{0.8}Zr_{0.2})_4AlC_3$ $(Cr_{5/8}Ti_{3/8})_4AlC_3$ $(V_{0.5}Cr_{0.5})_4AlC_3$		
HIGHER ORDER	$(V_{0.5}Cr_{0.5})_5Al_2C_3$ $(Ti_{0.5}Nb_{0.5})_5AlC_4$		

1.3 MAB Phases

1.3.1 Crystalline structure of MAB phases

In what concerns the MAB phases, as cited in the introduction, they possess different chemical formulas. However, experimentally synthesized MAB phases are frequently M_2AB_2 and MAB phases. The crystalline structure of M_2AB_2 or as called the Mn_2AlB_2 structure is orthorhombic that crystallizes in a Cmmm space group [94].

In more detail, the MAB phases, which include MAlB, M_2AlB_2, M_3AlB_4, M_4AlB_6, and M_4AlB_4 prototypes, are typically crystallized into orthorhombic crystal structures that depend on the M:B ratio and the number of interleaved Al-atom planes and often referred to as the 222, 212, 314, 416, and 414-types, respectively [10].

In the 212-type structure (space group Cmmm; x = 1, y = 0, z = 1), the BM_6 trigonal prisms, with B atoms at the center, connect on their rectangular and triangular faces in the ac-plane to form M-B blocks with a thickness of two M layers. These blocks are separated by Al monolayers. Each unit cell (u.c.) contains two formula units (f.u.). Each Al atom sit directly in between the B atoms in the M-B blocks directly below and above it, forming a B-Al-B chain along the stacking b-axis [10]. As such, adjacent M-B blocks are twinned across the Al planes, similar to the MAX phases. The relatively short atomic separation between B atoms in the B-B chains (parallel to 〈100〉) corresponds to the lattice parameter or a-LP [10].

The 314-type structure (space group Pmmm; x = 1, y = 1, z = 1) of Cr_3AlB_4 exhibits distinct differences from the 212-type structure: (1) M-B blocks encompass three M-atom planes, with only one f.u. in the u.c., (2) M-B blocks align along the c-axis, and (3) the c-LP of Cr_3AlB_4 is notably smaller compared to the b-LP of Cr_2AlB_2. Cr_4AlB_6, the sole representation of the 416-type compound (Figure I.8(c)), crystallizes in Cmmm space group [9]. This structure shares similarities with the 212 and 314 structures, yet the M-B blocks consist of 4 M-atom planes. Also, akin to the 212 structure, M-B blocks arrange along the b-axis, and the u.c. comprises two f.u. Overall, Cr_2AlB_2, Cr_3AlB_4, and Cr_4AlB_6 form the $(CrB)_2Al(CrB_2)_y$ (y = 1-3) series of MAB phases, analogous to the $M_{n+1}AX_n$ (n = 1-3) series of related MAX phases [9] .

The M-Al-B compounds (M = Mo, W) adopt a 222-type structure (space group Cmcm; x = 2 and z = 1), where M-B blocks are akin to those in the 212-type structure. However, Al bilayers intersperse each M-B block along the stacking b-axis. Each M-B block is displaced by 1/2, a + c, relative to the lower adjacent M-B block. Notably, the inclusion of a second Al layer results in the Al planes losing their status as crystallographic twinning planes, distinguishing them from the 212 structures.[10,94,95].

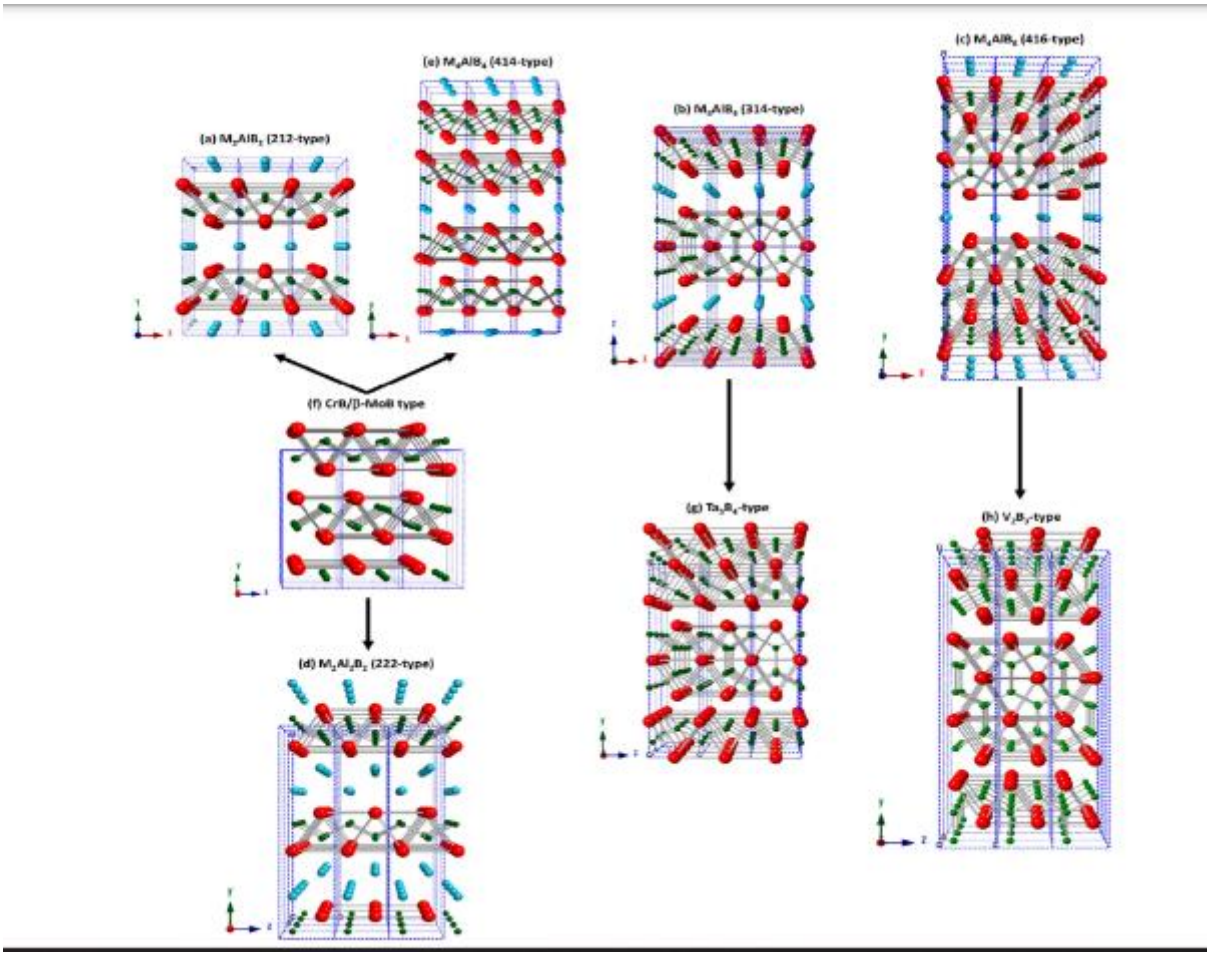


Figure I. 8: Crystal structures of various MAB phases and structurally related binary borides: (a) 212-type [Cmmm], (b) 314-type [Pmmm], (c) 416-type [Cmmm], (d) 222-type [Cmcm], (e) 414-type [Immm], (f) CrB/β-MoB [Cmcm], (g) Cr_3B_4 [Immm], and (h) Cr_4B_6 [Cmcm]. The M, Al, and B atoms are shown in red, light blue, and green, respectively. Dotted blue lines outline individual unit cells. Note that multiple unit cells are shown for clarity [10].

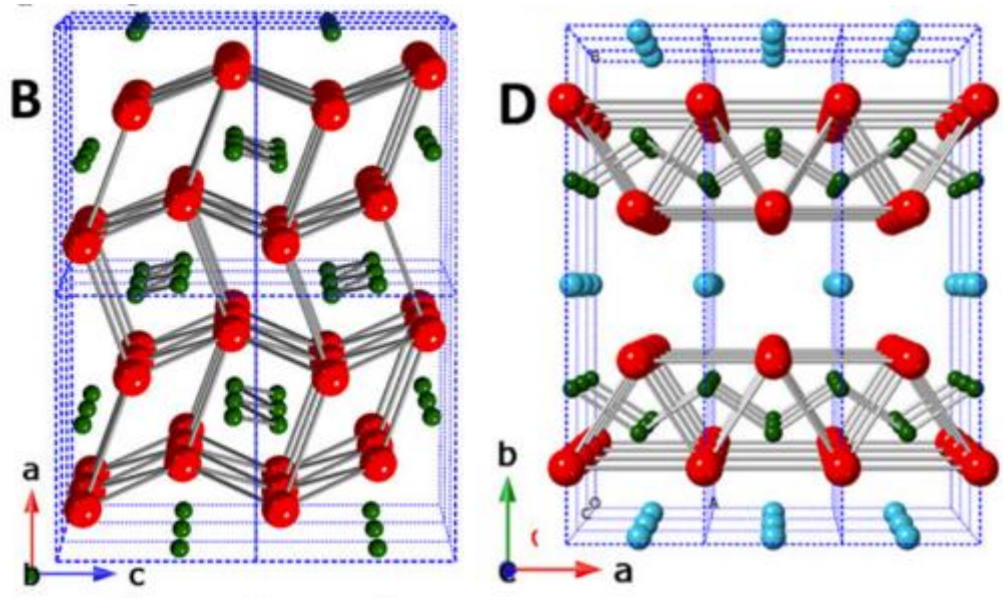


Figure I. 9 : Crystalline structure of (B) FeB and (D) Fe_2AlB_2 [10]

1.3.2 Microstructure of MAB phases

Figure I.10 depicts SEM images of a fractured Cr_2AlB_2, Mn_2AlB_2, and Fe_2AlB_2 surfaces. The microstructure of the MAB phases shows a polycrystalline aspect by grains with different orientations. The lamellar property of the MAB phases makes this observation possible without using transmission electron microscopy. There is a big resemblance between MAB and MAX phases concerning the typical morphology of the nonlamellar structure.

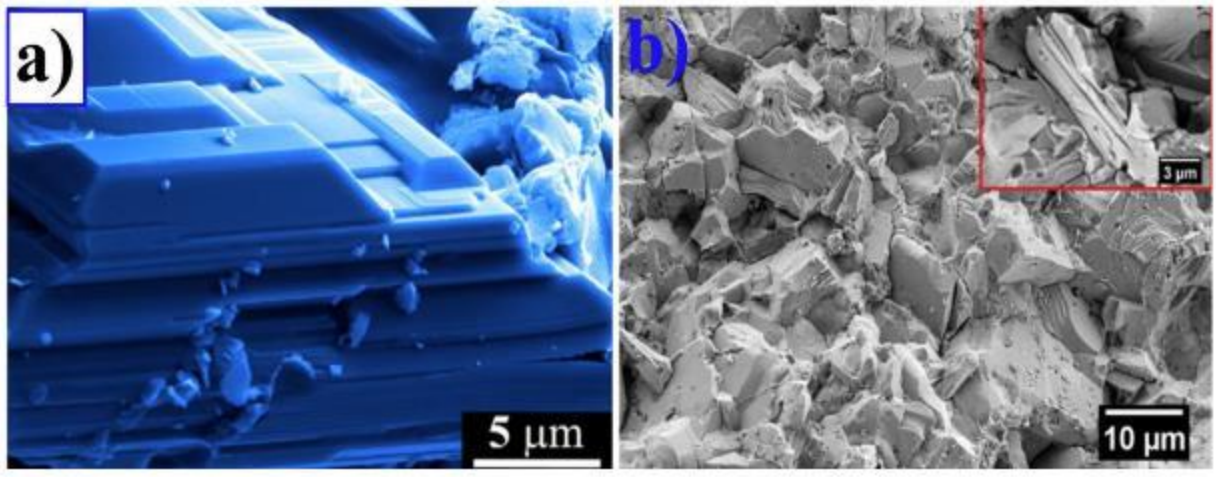


Figure I. 10: SEM imaging of a Cr_2AlB_2 grain, Microstructure of a Mn_2AlB_2 fracture facies [96,97].

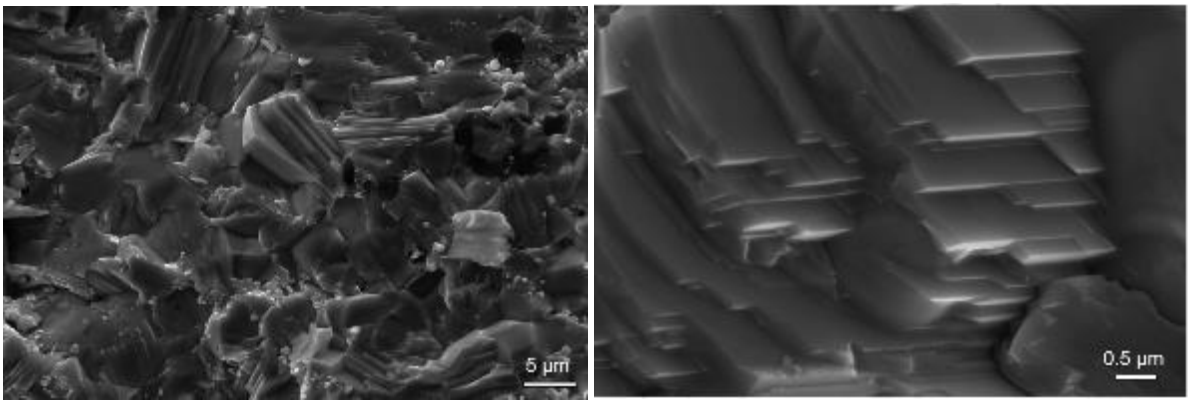


Figure I. 11: SEM micrographs of the fracture surfaces of Fe_2AlB_2 prepared by hot-pressing of 1.1Al/2FeB at 1100 ºC for 1 h under 30 MPa in Ar. (a) a low magnification, and (b) a high magnification SEM taken from(a) [12].

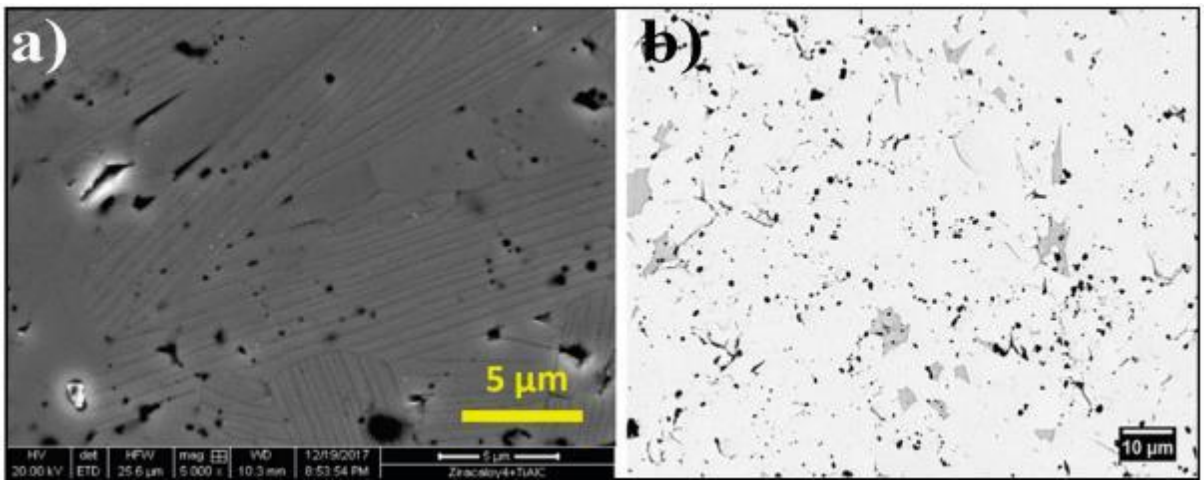


Figure I. 12: (a)Etched microstructure of MoAlB, (b) BSE (Backscattered Secondary Electrons) backscattered electron micrograph, of the polished surface of MoAlB properties of MAB phases [98].

1.4 properties of MAB phases

1.4.1 Elastic properties of MAB phases

Studies show as mentioned in Figure I.13 that MoAlB phase is two times rigid than Mn_2AlB_2 phase at room temperature. For both ceramics the Young's modulus E and shear modulus G decrease about 10-15 percent at 1000C temperature. It was supposed by Kota et al [10]. that the softening of the Al_xMn_y and Al_xMo_y intermetallics is the main cause of this drop. One

interesting thing is that the MAB phases show higher Young's modulus compared to reported MAX phases [10].

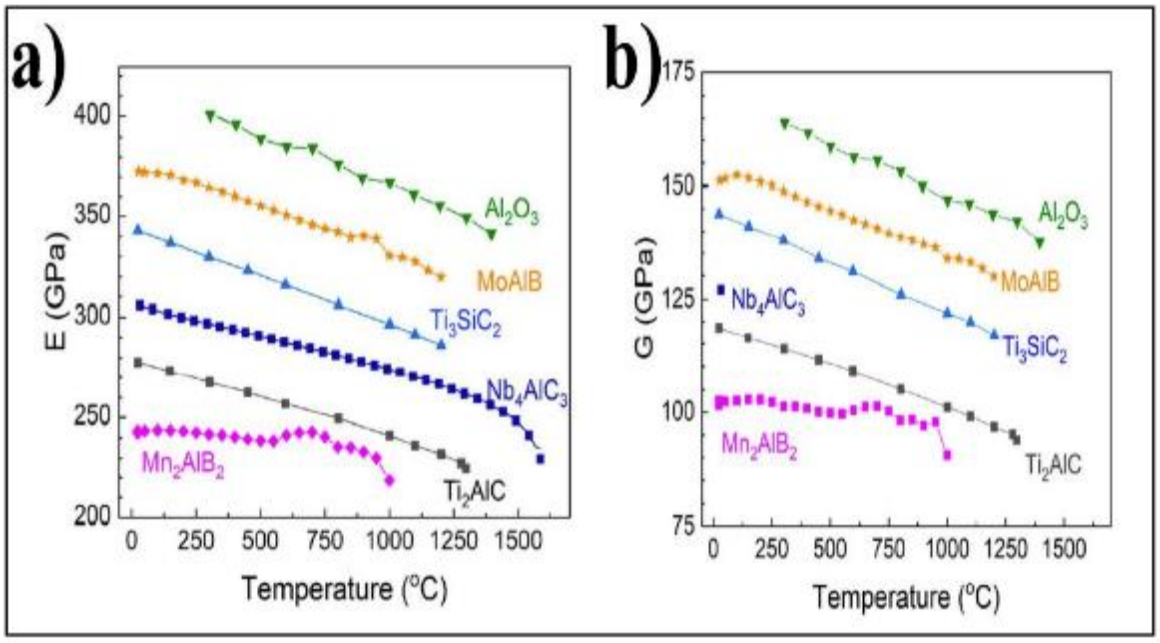


Figure I. 13: The Dependence of the Modulus of (A) Young € and (B) Shear Modulus (G) With Temperature [10].

1.4.2 Oxidation resistance of the MAB phases

Among the essential factors that determine whether a material could be used for high temperature is its oxidation resistance property. Kota et al. [14] introduced MoAlB as the only ternary boride that could form a protective oxide layer scale onto its surface when exposed at high temperature in air environment. It had the ability to form Al_2O_3 oxide layer, protective and adherent, making MoAlB as a potential candidate ceramic to be used at temperatures between 1100-1350 °C as shown in Figure I.14.

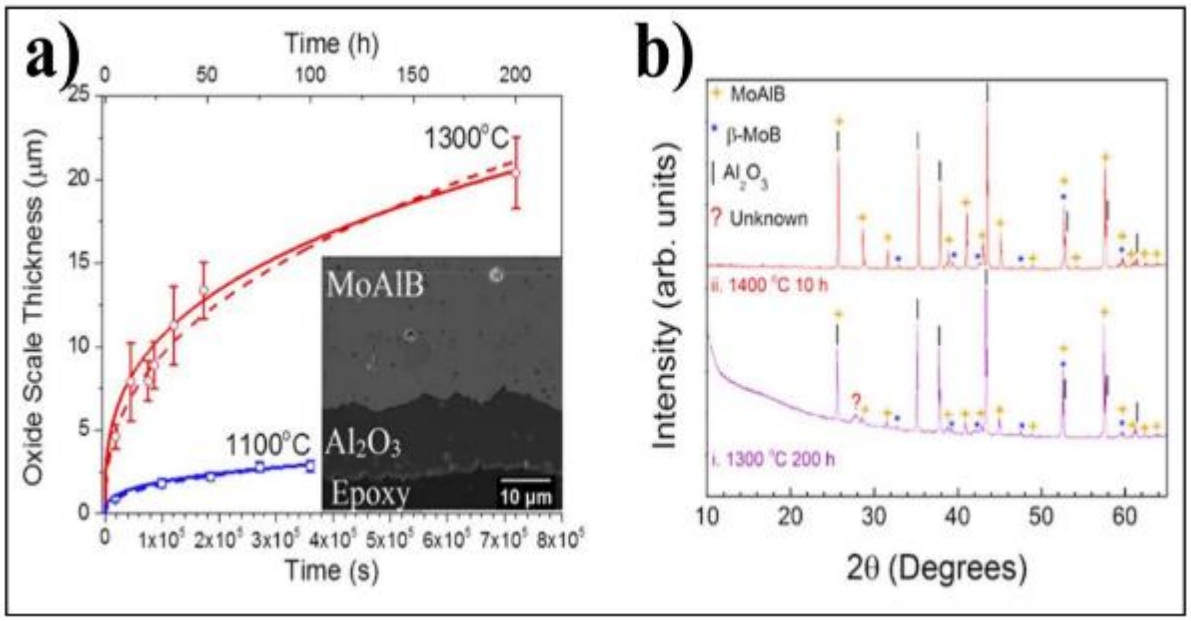


Figure I. 14: (a) Progression of the Al_2O_3 oxide layer on the MoAlB surface as a function of time, and (b) X-ray diffraction (XRD) of the layer formed [14] .

The MoAlB/oxide interface was proven to be free from cracks and voids, increasing its ability to sustain high exposure time to the harsh environment. Similarly to MAX phases, M and B elements also oxidize, the oxides products are volatile below 800 °C, thus their formation was only proven by theoretical investigations. In another study, Benamor et al. [99] proved the formation of these oxides through Raman and XPS analysis under heat-induced friction test, confirming the statement.

1.4.3 Thermal choc resistance

One of the desired properties of MAX and MAB phases is their resistance to thermal chocs compared to other engineering ceramics. Figure I.15 illustrates the flexural strength of some MAX, MAB phases, and other ceramics, after several cycles of quenching in water. Compared to alumina ceramic, MAX phases show better thermal choc resistance. However, MAB phases are shown to possess lower thermal choc resistance compared to MAX phases. As shown by X. Lu et al. [100] one of the properties of MoAlB ceramic is that it possesses a crack healing behavior, which it heals its cracks through filling them by oxides products (mainly alumina).

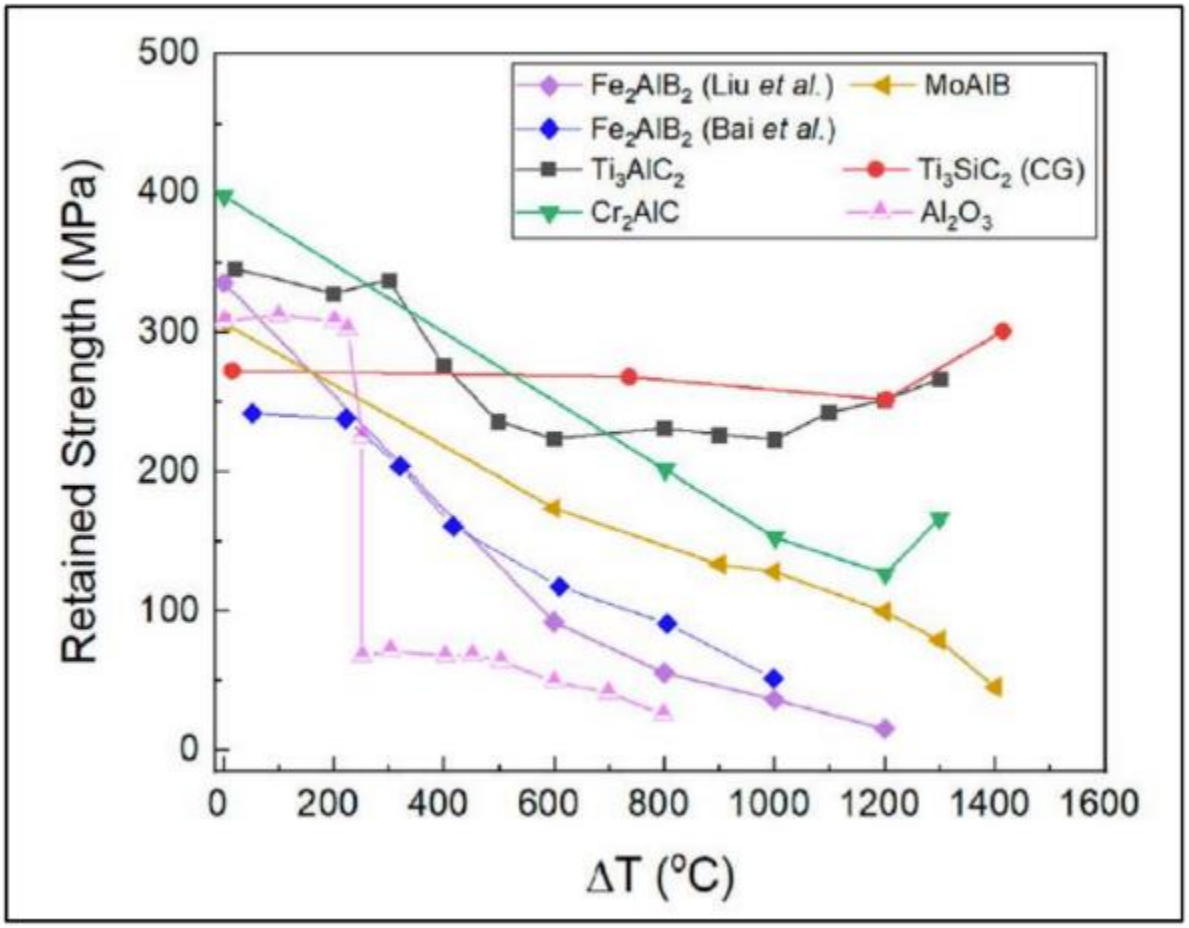


Figure I. 15 : Comparison of the thermal shock resistance of some MAX and MAB phases with Al_2O_3 [10] .

1.4.4 Magnetocaloric properties

Fe_2AlB_2 is a promising material for magnetic refrigeration devices due to its substantial magnetocaloric effect (MCE) near room temperature. When cyclically magnetized and demagnetized under adiabatic conditions, it absorbs and releases heat [101]. This allows it to be used for magnetic refrigeration, which has higher efficiency and avoids environmentally harmful chlorofluorocarbons compared to conventional refrigerators.

Another advantage of Fe_2AlB_2 is that it is composed entirely of earth-abundant elements, which makes it cost-effective compared to other magnetocaloric materials that contain expensive rare-earth elements, precious metals, or toxic elements [102].

Fe_2AlB_2 also has a high spin-orbit magnetic moment transfer (SOMT), which helps to avoid hysteresis losses and maintain mechanical stability, especially in a device operating at high frequencies. Additionally, the good thermal conductivity of the MAB phases can lead to

effective heat exchange in a prototype to compensate for the eddy current losses expected for electrically conductive materials [103].

Overall, Fe_2AlB_2 shows great potential as a magnetic refrigeration material, and its unique properties make it a promising alternative to other magnetocaloric materials [101–104].

1.5 Crack healing behavior of MAX and MAB phases

Researchers have always focused their efforts on developing new ceramic materials capable of healing large cracks at moderate temperatures in a short period of time, ceramics with repeatable healing capability and good mechanical resistance at elevated temperatures whether in air or in a vacuum atmosphere.

Owing to the weak bonding between M-A elements when exposed to high temperatures, MAX phases decompose into their binary MX compounds releasing A element through diffusion [105–107], A element get oxidized and forms a protective layer containing oxides [108,109].

Upon exposure of MAX phases to high temperature in an oxidizing environment; the selective oxidation of A element is favored over M element such as Al_2O_3 in the case of Ti_2AlC MAX phases [110]. Many studies have reported layered oxide scales in different MAX phases, such as TiO_2 and GeO_2 in Ti_3GeC_2 MAX phase (Figure I.16 a) and layers of TiO_2 and Al_2O_3 in $Ti_2AlC_{0.5}N_{0.5}$ MAX phase. They revealed that oxidation occurs by inward diffusion of oxygen and outward diffusion of A and M atoms [111,112].

In mostly all cases long time high temperature exposure causes the formation of both M and A containing oxides by diffusion through pores or grain boundaries, even if the first protective layer is dense and well adhered to MAX phase surface, as shown in Figure I.16 c and I.16 d [113].

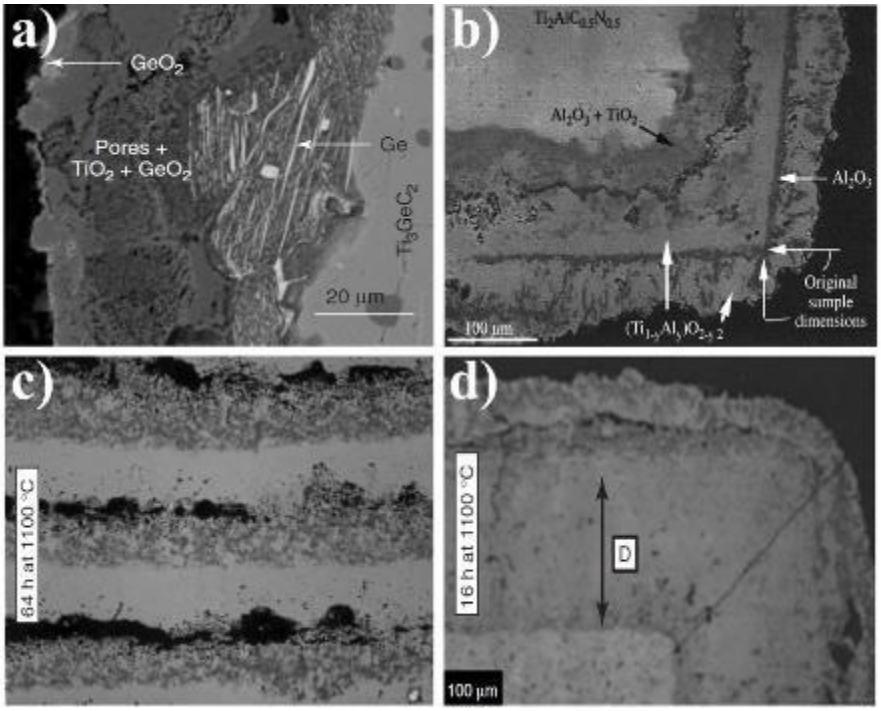


Figure I. 16: (a) SEM image of a Ti_3GeC_2 MAX phase oxidized at 900°C for 4h. [114] . (b) SEM micrographs of $Ti_2AlC_{0.5}N_{0.5}$ MAX phase oxidized in air at 1040°C for 16 h [115] . Cross-sectional SEM image of a Ti_2AlC sample oxidized in air at 1100°C for (c) 16h and (d) 64 h. The uniform layer labeled D in (d) is replaced by striated layers in (c) that are Al_2O_3-rich (dark layers) and TiO_2-rich layers. The uniform layer labeled D in (d) is replaced by striated layers in (c) that are Al_2O_3-rich (dark layers) and TiO_2-rich layers [115] .

1.5.1 Crack healing behavior of MAX phases and their composites

The presence of cracks in brittle materials such as ceramics may result in loss of performance or worst, a sudden catastrophic failure. The crack healing behavior of MAX phases requires an oxidation reaction to fill and seal the cracks where mainly "A" element serves as a repair filler.

Song et al. [116] studied the crack healing behavior of Ti_3AlC_2, where they showed its ability to fill a 7 mm crack length and 5 µm width at a healing temperature of 1100 °C for 2h healing time. The crack was filled by two oxide phases, α-Al_2O_3 and rutile TiO_2. It was found that increasing TiO_2 presence inside cracks leads to spallation failure due to a mismatch in the coefficient of thermal dilatation. The formation of only Al_2O_3 phase is preferred because it enhances hardness and Young's modulus of the healed zone, this was achievable in the case of Ti_2AlC MAX phase when the crack width is less than 1 µm.

The only materials capable of multiple healing behavior were micro-vascular polymers-based networks, until Li et al. [117] in 2012, presented Ti_2AlC as repeatedly repairing damage

ceramic, it achieves 7 healing cycles at a given location. The cracks were healed at 1200 °C for 2h, where Al_2O_3 covered the crack faces, and TiO_2 was present at the center of the healed zone, as shown in figure I.17.

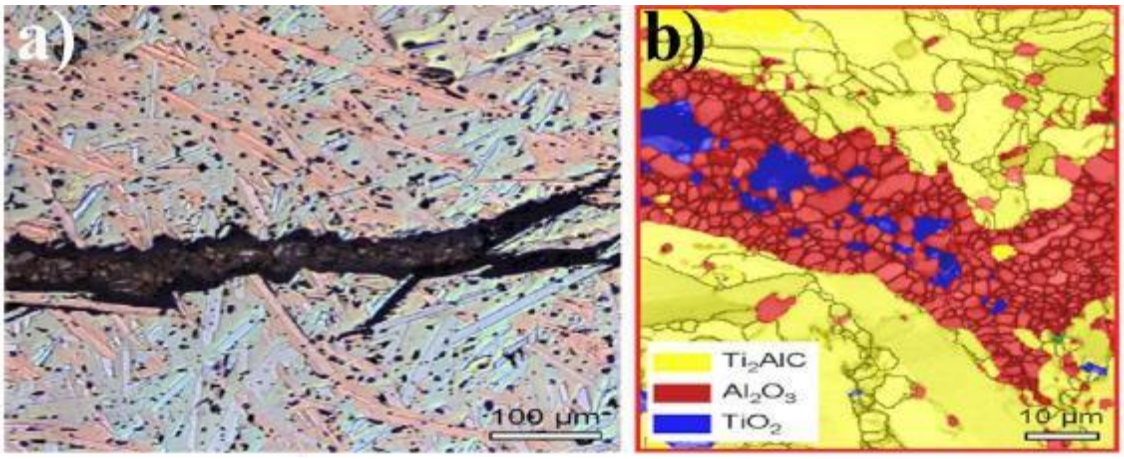


Figure I. 17: (a) Optical image showing a crack face both covered by the same Al_2O_3 layer (black) and the gap center was fully filled by a mixture of Al_2O_3 (black) and TiO_2 (large white particles). (b) SEM using electron backscatter diffraction of the healed-damage zone [118].

Al containing MAX phases; require high crack healing temperatures exceeding 1000 °C; the Cr_2AlC has gained interest since the healing temperature is done at 900 °C [61], which is lower than both Ti_2AlC and Ti_3AlC_2.

Shibo Li et al. [119] reported oxidation induced crack healing behavior of Ti_2SnC MAX phase, the crack healing behavior is done at 800 °C in only 1h. Restoring solid contacts by filling the cracks by SnO_2 and TiO_2 oxides resulted in mechanical and electrical properties recovery. Not only Ti_2SnC exhibited the lowest temperature at shorter time for healing, it does provide repeatable healing capability.

Ceramic Matrix Composites using MAX phases as reinforcing particulates have shown great potentials as multifunctional materials, they are called often MAXmet's for Metal Matrix composites [120,121]. MAX phases have been used to enhance hardness and wear behavior of soft metals [122,123], as well as toughness, bending strength and wear resistance of some ceramic materials [124,125], MAXmets are composites with high damping properties [126], with good electrical and thermal conductivities [127].

In the area of crack-healing property, MAX phases proved their ability to be used inside a ceramic matrix as an effective healing agent. Al_2O_3 ceramic matrix reinforced by $Ti_2Al_{0.5}Sn_{0.5}$ MAX phase solid solution showed ability of repairing cracks bellow 1000°C, the crack was filled by a mixture of SnO_2, TiO_2 and Al_2O_3 oxides [128]. Nb_2AlC also showed the capacity of producing Nb_2O_5 and $NbAlO_4$ oxides to potentially fill the cracks in ZrO_2 matrix [129].

1.6 Synthesis of MAX and MAB phases

The MAX phases can be synthesized using various techniques, including the hot pressing technique " HP " [130], the SPS technique for "Spark Plasma Sintering" [131–133] , the PSHS technique for "Pressured-assisted Self-Propagating High temperature Synthesis" [131], the SC technique for "Slip Casting" [134], and finally the HIP technique for "Hot Isostatic Pressing" [135]. These techniques yield highly dense materials. The Pressureless Sintering technique does not require the application of pressure during synthesis, thus the resulting material is easily transformed into powder.

1.6.1 Pressureless sintering method

several MAX and MAB have been synthesized using pressureless sintering methods. Córdoba et al. [136] conducted a study on the synthesis of Ti_3SiC_2 MAX phase using various molar ratios and starting powders under an Ar atmosphere. They achieved a purity of up to 98% at 1400 °C. The commonly employed approach in these methods involves using elemental powders of the MAX phase (Ti, Si, C) and carbides (SiC, TiC) in different molar ratios.

In another work [123] the formation of Ti_3SiC_2 was achieved by using titanium hydride (TiH_2) as starting powder, Liu et al. [137] synthesized Fe_2AlB_2 phase in the temperature range of 1000-1200 °C for 1h using pressureless sintering. They showed that a single Fe_2AlB_2 phase was achievable by pressureless sintering in the temperature range of 1100-1200 ºC for 1 h and concluded that Fe_2AlB_2 is more easily formed by the Al/FeB mixture compared to Fe/Al/B according to the Gibbs free energy calculations [124].

To overcome these manufacturing issues, the molten salt method is the most adequate for ceramic powder synthesis at low temperatures. Two different methods can be distinguished: molten salt assisted method and molten salt shielded synthesis (MS^3).

1.6.2 Molten salt assisted method

The first method includes mixing salt with the initial starting powders to enhance reactivity. Several MAX and MAB phases have been produced by this method. Wang et al. [138] synthesized V_2AlC ternary carbide by the molten NaCl-assisted method. They showed that the ionic liquid environment when salt melts it helps the formation of V_2AlC. The synthesis temperature was lowered from 1400 °C without salt assistance to 1050 °C when using NaCl.

Tin et al. [16] reported the successful synthesis of the Cr_2AlC phase in a binary NaCl/KCl system at 1000 °C. Other ternary compounds such as Ti_3SiC_2 [139] using NaCl molten salt and Cr_2AlB_2 [140] using eutectic NaCl/KCl have been successfully synthesized using this method. In all reported cases, the presence of salts reduced either or both synthesis temperature and time. Therefore, highly pure powder products were formed. Even though the molten salt-assisted method increased the sinterability of several MAX and MAB phases, the use of inert protective gas is still mandatory.

1.6.3 Molten salt shielded synthesis/sintering (MS^3)

The second method was recently discovered by Dash et al. [18] They showed a better alternative to the protecting inert gas atmosphere by a molten salt shielded synthesis (MS^3) process. Unlike the previously mentioned molten salt-assisted method, where inert atmosphere is required. This process uses salt not only as a reaction medium but also to protect the materials from oxidation during processing in an open-air atmosphere. Cold pressed salts can form a gas-tight encapsulation around the initial powders, inhibiting air entry Figure I.18 They were able to synthesize different ternary transition metal compounds (Ti_3SiC_2, Ti_2AlN, TiC, and MoAlB) as well as pure Ti.

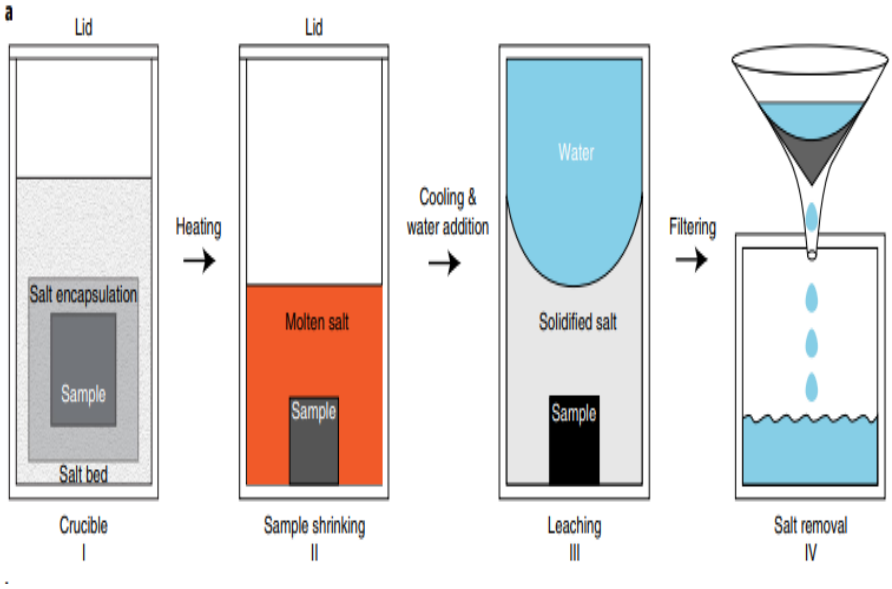


Figure I. 18: Stepwise schematic of the MS^3 process [18]

In another study, Roy et al. [141] reported the synthesis of V_2AlN and Ti_2AlN using a modified MS^3 process, where they skipped the encapsulation step Figure I.19 by using a low-melting eutectic salt mixture of NaCl-KCl (melting point 657°C). The single phase of Ti_2AlN was obtained at 1100°C, which was 150°C lower than the one synthesized by Dash.

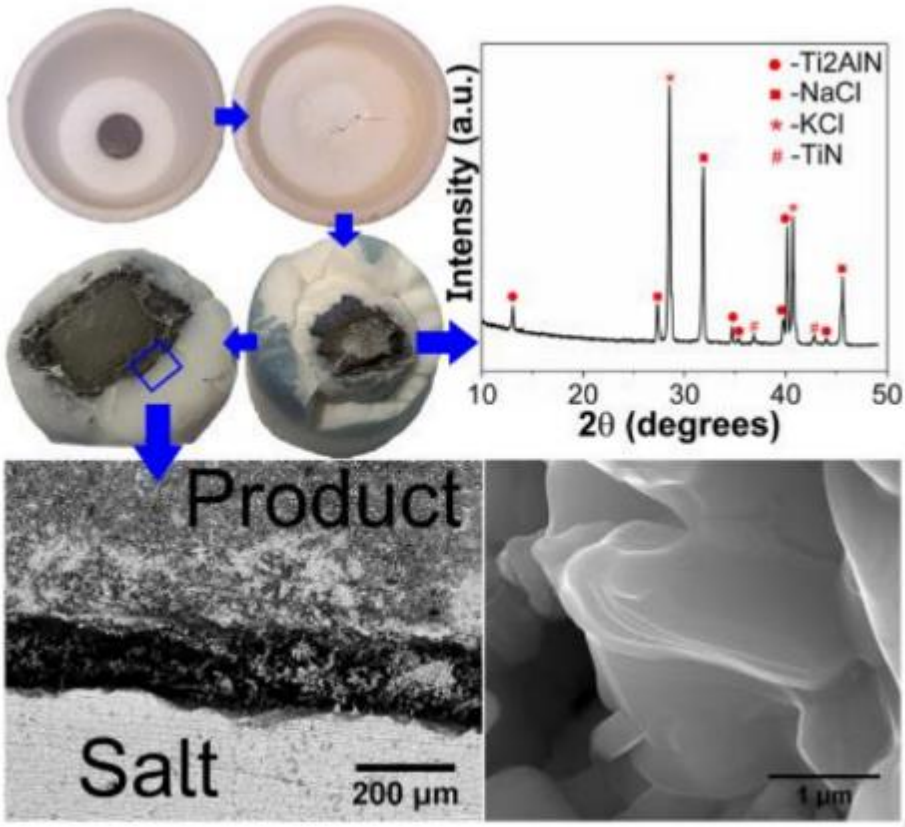


Figure I. 19: molten salt shielded synthesis (MS^3) without salt encapsulation in eutectic molten salt [141].

Recently, Dey et al. [15] synthesized Fe_2AlB_2, Mn_2AlB_2, and MoAlB powders by molten salt shielded synthesis with different salts (NaCl, KBr, and eutectic NaCl-KCl). Their experimental method differs from Dash et al.'s method [18,142]. The salts were used only as an airtight-shield and were not mixed with the initial powders. Their study showed that MAB phases could be synthesized in a salt medium without using any shielding gas. Despite all these advances in reducing synthesis temperature and time, the production process is still energy intensive. All attempts to further reduce them, even with small variations are welcome.

1.7 Application of the MAX and MAB phases in the environmental field

MAX and MAB phases have shown promise as catalysts in environmental applications. They can be used in processes such as pollutant degradation, water purification, and air filtration.

A magnetic MAX phase composite (MNPs-Ti_3AlC_2) was utilized for the adsorption and recovery of hexavalent chromium from Tannery wastewater [143]. The maximum adsorption of Cr (IV) was observed to be approximately 99% at pH 3, with an adsorbent dose of 100 mg for a 30 mL sample and a vortex time of 5 minutes, even in the presence of various competing ions. Alkaline leaching enabled easy recovery of about 98 ± 1% of Cr (IV) from the adsorbent surface. The adsorption process was spontaneous endothermic.

Shalini et al. [6] utilized Cr_2AlC for photocatalytic degradation of different organic pollutants in 2021 , Cr_2AlC has shown 99% efficiency in the degradation of malachite green, an organic pollutant under visible light irradiation demonstrated exceptional photocatalytic activity, achieving a remarkable 99% degradation efficiency under visible. The catalyst showed stability during recycling and being able to perform photoreactions for up to four cycles. They demonstrated that Cr_2AlC exhibited suitability for degrading cationic dyes compared to anionic dyes because the surface charge of the Cr_2AlC MAX phase was determined to be negative.

Ansarian et al. [144] studied the catalytic activity of the Ti_3GeC_2 MAX phase for the activation of peroxydisulfate (PDS) under ultrasound (US) irradiation. The Ti_3GeC_2 MAX phase exhibited excellent capability for PDS activation under US irradiation to achieve a high removal efficiency of 94.7% for a concentration of 0.15 mmol/L of PDS. Furthermore, the Ti_3GeC_2/PDS/US ternary system demonstrated outstanding performance in the removal of various pollutants, including dimethyl phthalate, hydroxychloroquine, and mefenamic acid.

These findings present a promising prospect for the application of Ti_3GeC_2 MAX phase-based materials in ternary catalyst/oxidant/US systems for efficient treatment of organic contaminants.

The sonocatalytic activity of the synthesized MAX phase was evaluated by degrading oxytetracycline antibiotics to mitigate potential pollution caused by emerging contaminants [145]. Remarkably, the Ti_2SnC MAX phase achieved a degradation efficiency of 100% within 2 hours under specific conditions ([Ti_2SnC] = 1 g L^{-1}, [OTC] = 10 mg L^{-1}, and natural pH). The sonocatalytic system based on Ti_2SnC also demonstrated excellent stability during ultrasonic irradiation, even after eight consecutive runs. Furthermore, the Ti_2SnC-mediated sonocatalytic system effectively degraded RIF, AB7, and LEV.

1.8 Summary:

The main points of the bibliographic study on the MAX and MAB phases showed herein could be summarized as follows:

- The crystalline structure of the MAX and the MAB phases have a crystalline structure similar to their binaries MX and MB, respectively, interleaved by mono or bi-atomic layers of A element.
- Because of the presence of the three atomic bonds (covalent, ionic, and metallic) some MAX and MAB combine some of the best properties of metals and ceramic materials.
- The most interesting property of MAX phases is their incredible easiness to be machined, neutron irradiation damage tolerance, high temperature oxidation resistance, similar electrical and thermal properties to metals.
- The MAX and MAB phases have various applications in the environmental domain like adsorption, pollutants degradation…

2. Chapter 2 From MAX to MXenes

2.1 Introduction

in 2011, the teams led by Barsoum reported the synthesis of new 2D materials in the form of powders from nano-lamellar three-dimensional precursors called s MAX phases [19]. This novel class of materials, named MXene by analogy with the MAX phases and graphene, made up of carbides or carbonitrides of transition metals, "functionalized" by surface groups such as hydroxyl, oxygen, or fluorine, commonly denoted as "T."

MXenes have the advantage of possessing significant chemical flexibility in theory, given the large number of existing MAX phases.

The literature reports various properties for this new class of materials, particularly for titanium-based systems, which are currently the most studied. Due to the properties of MXenes such as environmental-friendly characteristics, large specific surface area, high chemical stability, thermal/electrical conductivities, and hydrophilicity, MXenes can be employed as suitable materials in various applications including lithium-ion battery [146], semiconductor [147], supercapacitor [148] and environmental applications like adsorption [149].

2.2 Synthesis of MXenes

This material was obtained by immersing a powder of Ti_3AlC_2 in a 50% solution of hydrofluoric acid (HF) [19]. This chemical treatment results in the removal of the A-element from the MAX phase while preserving the structure of the MX layers. The result is a stack of 2D titanium carbide ($Ti_3C_2T_x$) sheets passivated by surface terminations, denoted as T, resulting from the chemical treatment. These surface terminations can be of the OH, O, or F type. The general chemical composition of these materials is $M_{n+1}X_nT_n$.

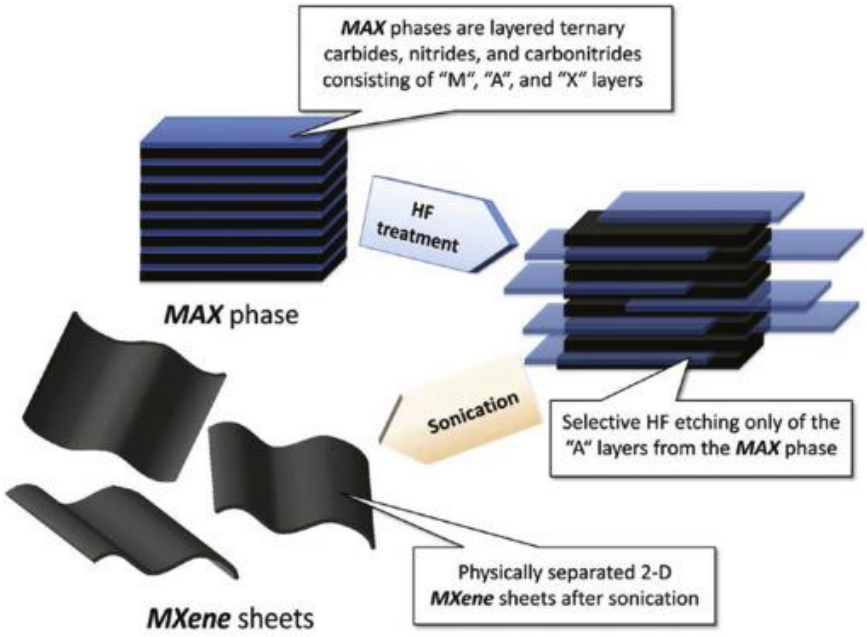


Figure II. 1: Schematic of MXene synthesis [150].

The chemical formula of MXene is represented as $M_{n+1}X_nT_x$, where T represents the surface terminating species and x indicates the coverage of T on the MXene surface. When x = 2, it means that for each surface M atom, one terminating species is attached [151,152].

The termination process occurs when the A layer is etched from the MAX phase. As the bonds between the MX slabs and the atomically thin A layer are broken, new bonds are formed with the etchant species. The etching process is influenced by the specific chemicals used, while the termination process is demonstrated theoretically. The theoretical simulation Figure II.2 illustrates how the etchant (HF) interacts with the MAX phase edge (Ti_3AlC_2), targeting the A layer but also interacting with the adjacent M elements. HF dissociates, attracting F to the A and M elements, while H prefers to form H_2. As the concentration of HF increases, the M-A bonds eventually break, and AlF_3 is formed. Consequently, the A element is removed, and the two-dimensional MXene material starts to form. After the A element removal, the exposed M element surfaces are terminated by both H and F, with the F-terminated surface being the preferred configuration, while H_2 gas is released as a by-product [153].

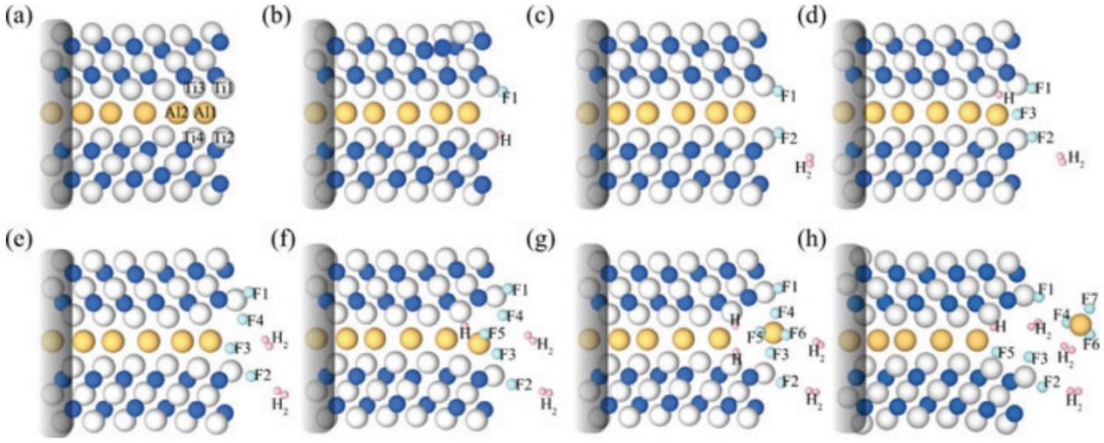


Figure II. 2: Lowest-energy atomic configurations during the step-by-step intercalation of HF via the Ti_3AlC_2 edge and extraction of AlF_3: (a) pristine and (b) one, (c) two, (d) three, (e) four, (f) five, (g) six, and (h) seven HF-intercalated MAX complexes. Atoms at the left edge are fixed and shown here by a shaded region. Silver, blue, orange, cyan, and pink balls represent Ti, C, Al, F, and H atoms, respectively [153].

Since then, numerous MXenes have been obtained, such as Ti_2C, Nb_2C, V_2C, Ti_3CN, and Ta_4C_3, as well as solid solutions on the M-site, such as $(Ti_{0.5}, Nb_{0.5})_2C$, $(V_{0.5}, Cr_{0.5})_3C_2$, Mo_2TiC_2, $Mo_2Ti_2C_3$, and Cr_2TiC_2 [154–156], In what follows, we will describe the synthesis of the two most published MXenes, notably the Ti_3C_2Tx and Cr_2CT_x MXene.

2.2.1 $Ti_3C_2T_x$ MXene

The first method used for the synthesis of MXenes involves immersing a powder of the MAX phase in a 50% aqueous HF solution to remove the A-element [19]. It was suggested that these terminations were a result of the etching process, as indicated by the following simplified reactions.

$$Ti_3AlC_2 + 3HF \rightarrow AlF_3 + 3/2H_2 + Ti_3C_2 \text{…..II.1}$$

$$Ti_3C_2 + 2H_2O \rightarrow Ti_3C_2(OH)_2 + H_2 \text{ ……..II.2}$$

$$Ti_3C_2 + 2HF \rightarrow Ti_3C_2F_2 + H_2 \text{ ……..II.3}$$

Subsequently, other treatments have been used to improve the quality of the obtained MXenes and to overcome the complex handling of concentrated HF.

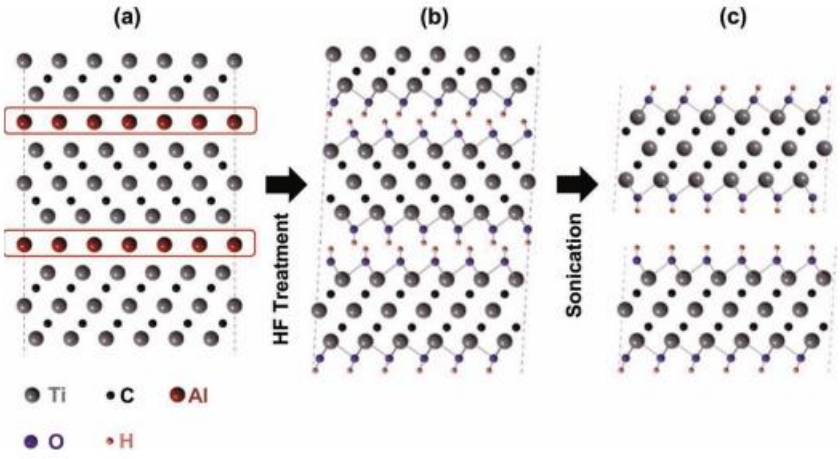


Figure II. 3: Schematic of the etching and delamination process of MXene from MAX phase [19].

The synthesis conditions (processing time, concentration, and temperature) are key factors in obtaining high-quality $Ti_3C_2T_x$.

Hu et al. [157] prepared $Ti_3C_2T_x$ using both low concentration (6 mol L^{-1}) and high concentration (15 mol L^{-1}) of HF. Corresponding results showed that Ti_3C_2 at low concentration had a high content of O functional groups, and they predicted a high electrolyte capacity of 1190 F g^{-1} could be achieved when Ti_3C_2 is terminated with O groups.

It is well known that high HF concentration is highly dangerous to the environment and harmful to health. One of the problems with HF treatment is its highly aggressive nature, which often leads to MXene powders containing defects such as holes [154]. and the attack of M-X bonds before the complete removal of the A-element. The processing time is crucial, making the process using HF challenging to control. As a result, several harmless and less hazardous synthesis methods have been proposed to replace the HF treatment for $Ti_3C_2T_x$ preparation.

Hope et al. [158] proposed a treatment of Ti_3AlC_2 by mixing lithium fluoride (LiF) in an HCl solution and showed that the functional groups prepared by HF and the LiF-HCl mixture had significant differences. The HF-prepared samples had four times more F terminations, while the LiF-HCl-prepared samples had a higher content of O terminations. This suggests that the LiF-HCl method is preferred for producing MXenes for batteries.

In another study, Ghidiu et al. [159] also indicated that the interlayer spacing of the samples prepared by the (HCl/LiF) mixture is larger than the MXene obtained through the HF

route, due to the intercalation of multiple layers of water and Li^+ ions between the $Ti_3C_2T_x$ sheets. LiF can also be replaced by other fluoride salts.

In this field, Wang et al. [160] prepared samples using a mixed solution of FeF_3 and HCl and showed a faster oxidation rate in water.

Due to the toxicity of fluoride-containing solutions, many other etching agents have been studied. Yang and his group [161] demonstrated an electrochemical approach without fluoride for the delamination of Ti_3C_2 in an aqueous electrolyte. In this method, the aluminum atoms were attacked by chloride ions in an anodic etching process, and the intercalation of ammonium hydrogen allowed for the exfoliation of the anode edges, resulting in a MXene with two OH and O terminations. This MXene exhibited remarkable surface capacity in superconductor applications.

Another cost-effective etching agent using an alkaline medium was studied by Li et al. [162], who conducted experiments with NaOH at high temperature and at a concentration of 27.5 M, which leads the Aluminium hydroxide was dissolved in NaOH, resulting in highly pure MXene.

Gengnan Li et al. [163] successfully elaborated MXene using KOH. The resulting MXene had no -F functional groups and exhibited improved energy storage properties compared to MXene synthesized by HF.

2.2.2 Cr_2CT_x MXene

So far, there have been two approaches for chemically etching Cr_2AlC to achieve exfoliation. The first method was developed by Bhuvaneswari Soundiraraju et al. [164] They employed a distinctive approach to exfoliate Cr_2AlC, utilizing a combination of ferric chloride ($FeCl_3$) and tartaric acid (TA). This technique had not been previously utilized for exfoliating any recognized MAX phases.

This approach has not been previously attempted for the exfoliation of any known MAX phases. In this method, the selective removal of aluminum (Al) is facilitated by the difference in electrode potentials within the system. Subsequently, the organometallic complex-forming ability of TA is utilized to remove the etched Al from Cr_2AlC, preventing the formation of insoluble alumina. The resulting two-dimensional (2D) nanosheets of (multilayered) ML-

Cr_2CT_x are then delaminated to (few-layered) FL-Cr_2CT_x by immersing them in dimethyl sulfoxyd (DMSO) and sonicating as described in Figure II.4. .

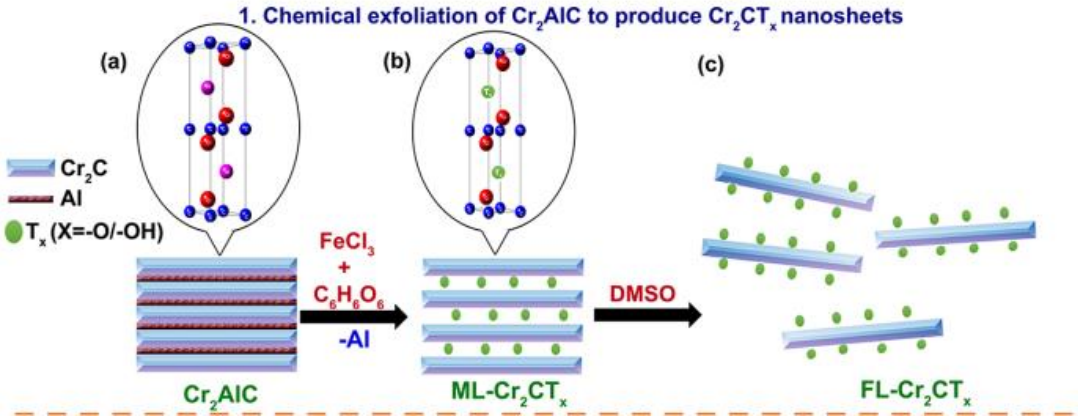


Figure II. 4 : Schematic representation of the synthesis of Cr_2CT_x nanosheets [164].

The second method [165] is A simple synthesis strategy, was suggested to produce Cr_2CT_x from Cr_2AlC by using suitable compositions of H_2SO_4 and LiF under mild conditionswhere Al layers were etched from the layered Cr_2AlC and successfully transformed into a composite of Cr_2CT_x MXene (Cr_2C and Cr_2CO_2) without the involvement of fluoride.

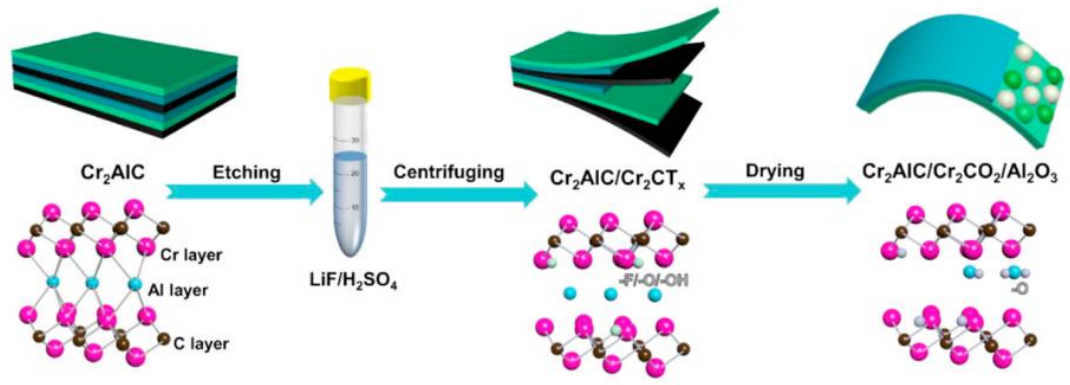


Figure II. 5 : The etching process from Cr_2AlC MAX to Cr_2CT_x MXene [165].

2.3 Properties of MXenes

Two dimensional (2D) materials have garnered great attention owing to their unique physical and chemical properties such as High Surface Area, Chemical Stability, Mechanical Strength, Thermal Stability and Optical Properties.

2.3.1 Chemical properties

MXenes typically possess a hydrophilic surface. However, Michael Ghidiu et al. discovered that $Ti_3C_2T_x$ formed using a combination of 10% HF with LiCl exhibited only ion exchange and H_2O intercalation, unlike MXene produced using 10% HF alone [166].

A schematic diagram in Figure II.6 illustrates the changes in basal spacing in this intercalated MXene [166]. Due to the presence of the redox-active Ti atom, titanium-based MXenes demonstrate high volumetric capacitance. The conductive carbide layer within MXenes facilitates the supply of electrons to the redox-active sites. Surfaces of transition metal oxides serve as redox-active centers, promoting ion transport.

As a result, MXenes have become prominent candidates for pseudocapacitors, which utilize fast redox reactions to enhance energy density [167].

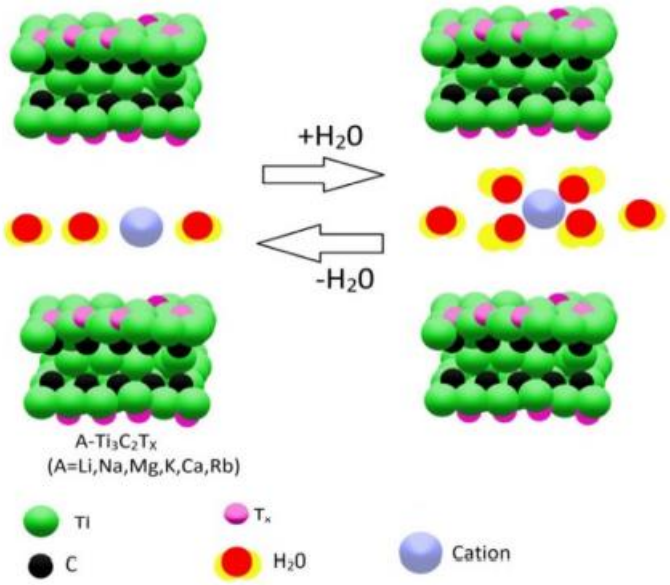


Figure II. 6: Schematic diagram representing reversible cointercalation of H_2O in $Ti_3C_2T_x$ MXenes having intercalated cation A (denoted as A- $Ti_3C_2T_x$) [166].

2.3.2 Mechanical properties

The mechanical properties of MXenes are highly influenced by their surface terminations. O-terminated MXenes are predicted to exhibit very high stiffness, whereas those terminated by other groups (such as F and OH) [168] display lower elastic stiffness value. This is due to the difference of lattice constants of MXenes with different terminations, where O-terminated MXenes typically have smaller lattice parameters than F or OH-terminated MXenes [169]. Surface-functionalized MXenes, in general, exhibit increased flexibility compared to bare MXenes. For instance, the functionalization of Ti_2C reduces its Young's modulus but enables it to withstand larger strains than bare Ti_2C and even graphene [170]. The surface-terminated groups serve as a buffer layer for Ti_2C during tensile deformation, slowing down the collapse of Ti layers and increasing the critical strain at which Ti_2C fractures [21].

The mechanical properties of MXenes are also influenced by the number of atomic layers, determined by 'n' in its chemical formula $M_{n+1}X_n$. Studies [171] have shown that the thinnest Ti_2C MXene has the highest Young's modulus among all $Ti_{n+1}C_n$ (n = 1, 2, 3. In the case of

functionalized MXenes, it has been demonstrated that as 'n' decreases, the strength and hardness of $M_{n+1}X_nT_x$ gradually increase [172].

2.3.3 Electronic properties

MXenes cover various electronic properties ranging from metallicity and semiconductivity to topological insulativity, due to their high compositional diversity. Extensive theoretical and experimental research has been conducted to investigate the band structures, density of states (DOS), and other electronic properties of MXenes [173].

The findings indicate that the majority of (functionalized) MXenes are metallic or semimetallic, while only a small number exhibit semiconductor behavior.

Early theoretical studies have reported several examples, including Sc_2CT_2 (T = OH, F, O), Ti_2CO_2, Zr_2CO_2, and Hf_2CO_2, with band gaps ranging from 0.24 to 1.8 eV [174].

Notably, $Sc_2C(OH)_2$, Sc_2CF_2, and Sc_2CF_2 have reported band gaps of 0.45, 1.03, and 1.8 eV, respectively, highlighting the influence of surface groups on the electronic properties of MXenes [175].

The band structures of $Sc_2C(OH)_2$ and Sc_2CF_2 exhibit more similarity compared to Sc_2CO_2, as F and OH groups require an additional electron for stabilization, while O can accommodate two more electrons. Based on band structure analysis, five out of six structures are predicted to have indirect band gaps, except for $Sc_2C(OH)_2$ [176].

To further understand the semiconductor behavior observed in some functionalized MXenes, researchers have investigated the electronic structures of both bare and functionalized MXenes. Obtained results show that, similar to MAX phases, bare MXenes are generally metallic, with the Fermi energy contributed by the d orbitals of the M element [177].

The p orbitals of the X element are located slightly below the d orbitals, creating a small band gap. After functionalization with F or O surface groups, the Fermi energy shifts downward. F functionalization leads to a downward shift as each F gains one electron, while O functionalization causes a further downward shift, ultimately resulting in Ti_2CO_2 becoming a semiconductor. Projected density of states (PDOS) plots of Ti_2C, Ti_2CF_2, and Ti_2CO_2 provide a clearer understanding of this mechanism [178].

Additional studies [179,180] revealed that strain or an external electric field can strongly influence the band gap of Ti_2CO_2 and Sc_2CO_2. Furthermore, the similarity of M elements, such as Ti, Zr, and Hf results in similar electronic properties.

As they belong to the same group and have the same outermost electron configuration ($4s^2$, $5s^2$, and $6s^2$ respectively), they exhibit a transition trend from metallic to semiconducting characteristics. For M_2CO_2 (M = Ti, Zr, Hf) MXenes, the band gap increases with the period of the M metal, corresponding to a decrease in metallicity[179].

However, in the case of $Ti_3C_2O_2$ and $Ti_4C_3O_2$ MXenes, the increasing number of Ti (M) elements counteracts the effect of the 2p orbitals of O leading to a return to metallic behavior [181].

2.4 Application of MXenes

MXenes are found in various applications because of their structural, surface, optical, mechanical, magnetic, and transport properties, which are significantly influenced by the MXene fabrication process [182].

These characteristics have facilitated the application of MXenes in energy storage and conversion, telecommunications, sensor science, environmental applications, and the biomedical field.



Figure II. 7: Schematic illustrating the use of MXenes [183]

2.4.1 MXenes for environmental applications

MXene, which consists of two-dimensional transition metal carbides/nitrides, has emerged as a promising material for addressing environmental concerns related to toxic compounds.

due to their exceptional physical and chemical properties, including a larger specific surface area, enhanced surface functionality achieved through excellent functionalization capabilities, and easy dispersibility in solvents like water.

MXene finds applications in separation techniques such as photocatalysis, adsorption, and membrane separation. It possesses a highly hydrophilic surface, ion exchange capabilities and robust surface functional groups [184].

2.4.1.1 Membrane uses of MXenes

In recent decades, membrane separation has emerged as a highly promising technology to address environmental and energy-related challenges [185]. It has found widespread application in industries such as chemicals, pharmaceuticals, and water treatment, offering numerous advantages leading to a decreased carbon footprint, enhanced reliability, straightforward operation, and minimized secondary pollution [186].

The first MXene-based membrane [187] was prepared through vacuum filtration of a colloidal solution of $Ti_3C_2T_x$ onto a hydrophilic polyvinylidene difluoride (PVDF) substrate with a pore size of 0.45 µm. The MXene sheets were easily stacked in layered structures with

a well-defined interlayer spacing, which acted as selective transport channels. This membrane exhibited a water flux of 37.4 L bar^{-1} h^{-1} m^{-2}.

Later, various MXene-based membranes were prepared through vacuum filtration. The first example was a MXene-based membrane filtered onto a polyethersulfone (PES) support. The prepared ultrafiltration membrane exhibited a water flux of 115 L m^{-2} h^{-1} and a rejection rate of 92.3% for Congo red dye at a pressure of 0.1 MPa [188] .

Ding et al. elaborated $Ti_3C_2T_x$ membranes with expanded microchannels to further enhance the water flux [189]. During the colloidal fabrication process, $Fe(OH)_3$ was used as an intercalation medium to increase the spacing between the layers. The resulting $Ti_3C_2T_x$ membranes demonstrated excellent water permeation performance (over 1000 L (bar h m^2) $^{-1}$) with favorable rejection rates (over 90%) for Evans blue molecules.

Another type of ultra-thin 2D MXene membrane was prepared for pervaporation desalination application [190]. Polyacrylonitrile (PAN) and MXene exhibited a water permeation of 85.4 L m^{-2} h^{-1} and a 99.5% rejection rate for NaCl at 65 °C. Furthermore, this membrane demonstrated durability and long-term performance in a synthetic seawater system, highlighting the potential of MXene-based materials in water treatment applications.

2.4.1.2 MXenes for Photocatalytic Applications

The initial experimental attempt for photocatalytic applications of MXenes was involved using $Ti_3C_2T_x$ MXene as a photocatalyst for the degradation of methylene blue (MB) and acid blue 80 [191]. MB was degraded by 81% when in contact with $Ti_3C_2T_x$ under UV light for 5 hours, whereas only 18% degradation occurred in darkness. Up to 62% of acid blue was degraded after interacting with MXene under UV light within 5 hours. In contrast, no degradation took place in darkness even after 20 hours.

Semiconductor/MXene nanocomposites have also been studied to enhance photocatalytic activity.

Gao et al. [192] synthesized $TiO_2/Ti_3C_2T_x$ nanocomposites through a hydrothermal process, showing improved photocatalytic activity for the degradation of methyl orange under UV irradiation compared to pure TiO_2 or Ti_3C_2. Their studies suggest that the $TiO_2/Ti_3C_2T_x$ composite exhibits more efficient electron-hole separation than pure TiO_2 or $Ti_3C_2T_x$ under UV irradiation.

To further enhance the photocatalytic activity of the $TiO_2/Ti_3C_2T_x$ complex, Peng et al. [193] used the hole-trapping capability of the Schottky junction and exposed active facets to improve photocatalytic performance. The enhanced charge separation and exposed active facets significantly enhanced the photocatalytic degradation of methyl orange dye. This work opens up new possibilities for utilizing MXenes in high-performance photocatalysts.

Zhou et al. [194] synthesized a $CeO_2/Ti_3C_2T_x$ nanocomposite through a one-step hydrothermal method based on the electrostatic attraction between Ce^{3+} ions and $Ti_3C_2T_x$ nanosheets. The composite exhibited excellent photocatalytic activity in the degradation of Rhodamine B compared to pure $Ti_3C_2T_x$ and CeO_2.

In another study, the $Ti_3C_2T_x$-TiO_2-CuO nanocomposites [195] demonstrated excellent photocatalytic degradation of methyl orange (> 99% in 80 minutes) compared to the $Ti_3C_2T_x/TiO_2$/CuO nanocomposite.

2.4.1.3 MXenes as Adsorbents

adsorption stands out as a highly effective, versatile, and cost-efficient technique for water treatment. Its ability to remove a wide range of contaminants including organic compounds, heavy metals, pesticides, dyes, and other pollutants, with high efficiency, selectivity, and ease of operation. Its compatibility with existing processes, and its environmental friendliness make it a favorable choice for water purification applications.

Due to the high specific surface area and abundant -OH and -O functional groups with adjustable surface chemistry, MXenes exhibit competitive or superior adsorption performance compared to other nanomaterials. The presence of functional groups on the MXene surface provides direct ion exchange sites and contributes to reduce certain organic molecules and cations [196,197].

MXenes and their composites demonstrate a strong ability to intercalate multiple ions. Various cations such as Na^+, K^+, NH_4^+, Mg^{2+}, and Al^{3+} and organic molecules (such as hydrazine, urea, and dimethyl sulfoxide) was easily intercalated between the layers of $Ti_3C_2T_x$ MXene [182,198]. $Ti_3C_2T_x$ is the most commonly studied MXene model in this field of research.

2.4.1.4 Removal of inorganic contaminants by MXene

Heavy metal ions, including Pb(II), Cr(IV), Hg(II), Cd(II), and Cu(II), are highly toxic to humans and other living organisms, making them significant pollutants in water and soil. The most effective method for removing these heavy metal ions is adsorption, as biological processes or chemical reactions are unable to degrade them. MXenes, with their abundant active sites, can adsorb metal ions through electrostatic and chemical interactions [199].

Numerous studies have been conducted on the sequestration of heavy metal ions using MXenes. Among the various toxic heavy metal ions in water, Pb(II) is a commonly encountered pollutant, and its concentration in drinking water is strictly regulated.

In 2014, Qiuming Peng et al. [200] reported that $Ti_3C_2(OH/ONa)_xF_{2-x}$ was synthesized via chemical exfoliation and alkalization intercalation, demonstrated strong Pb(II) ion adsorption (140 mg/g) and selectivity against competing cations like Ca(II) and Mg(II). Adsorption involves trapping Pb(II) ions in hydroxyl sites, forming robust bonds with oxygen atoms. This mechanism, depicted in Figure II.8, was corroborated by first-principles calculations, highlighting the influence of hydroxyl sites and functional groups on $Ti_3C_2(OH)_xF_{2x}$ MXene's Pb(II) ion adsorption behavior

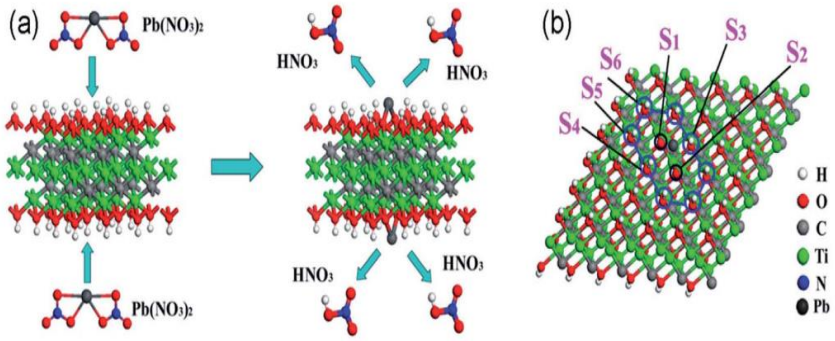


Figure II. 8: (a) Schematic illustration of the formation of the $Ti_3C_2(O_2H_{22m}Pb_m)$ structure from $Ti_3C_2(OH)_2$ to $Ti_3C_2(O_2H_{22m}Pb_m)$; (b) top-view of the $Ti_3C_2(O_2H_{22m}Pb_m)$ structure when the Pb coverage is 1/9 ML. S1–S6 represent the different atom sites of the hydroxy [200].

So far, experimental work on Pb^{2+} removal by MXene has been limited to $Ti_3C_2T_x$. The effect of $M_2X(OH)_2$ structures on the adsorption behavior of Pb^{2+} has been theoretically investigated through first-principles calculations [201]. The formation energies of Pb^{2+} adsorption on $M_2N(OH)_2$ are higher compared to $M_2C(OH)_2$, suggesting that transition metal nitrides are more effective than carbides for the adsorption of heavy metals.

Cr(VI) is considered as another significant heavy metal pollutant in water after Pb(II), and its adsorption characteristics on MXenes have also been studied. Cr(VI) is predominantly found in its anionic form, $Cr_2O_7^{2-}$

Ying et al. [197] conducted a study where they observed that $Ti_3C_2T_x$ MXene exhibited a high adsorption capacity for Cr(VI) of 250 mg/g under optimized synthetic conditions (10% HF delamination, room temperature, pH = 5). The treated water showed a residual Cr(VI) concentration below 5 ppm. $Ti_3C_2T_x$ MXene not only reduces Cr(VI) to less toxic Cr(III) but also concurrently adsorbs the converted Cr(III). Initially, electrostatic attraction between the positively charged MXene surface and negatively charged $Cr_2O_7^{2-}$ leads to Cr(VI) adsorption (protonation of MXene's hydroxyl groups at low pH). Upon adsorption, electrons transfer from MXene to $Cr_2O_7^{2-}$ aided by H^+ forming TiO_2 and Cr(III) ions. Cr(III) ions interact with the [Ti-O] bond on MXene forming the Ti-O-Cr(III) structure. This reduction mechanism extends to other oxidizing agents like $K_3[Fe(CN)_6]$, $KMnO_4$, and $NaAuCl_4$, which can be reduced and removed by $Ti_3C_2T_x$ MXene.

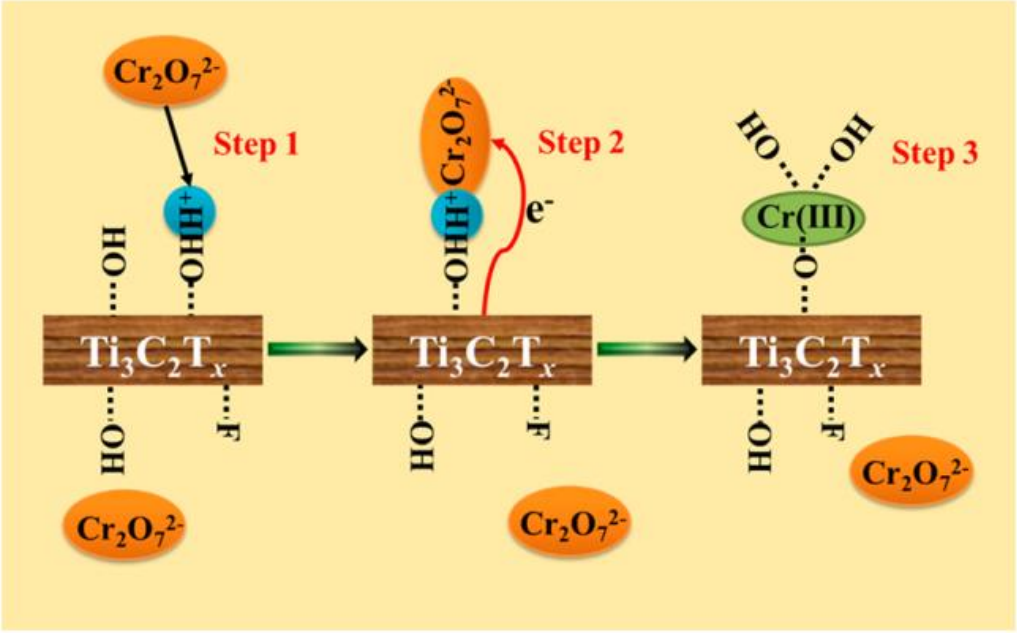


Figure II. 9: Illustration of the Removal Mechanism of Cr(VI) by the $Ti_3C_2T_x$ Nanosheets [197].

Zhang et al. [202] synthesized a new 2D material, MXene-iron oxide (MXI), by selectively exfoliating an aluminum layer followed by magnetic intercalation of iron oxide for phosphate sequestration in water.

Compared to commercial adsorbents, the MXI nanocomposite exhibited superior treatment capacities of 2100 and 2400 Kg kg^{-1} (simulated and real, respectively) in phosphate wastewater tests with fast kinetics. The material can be recycled using binary alkaline brine solutions.

On the other hand, Asif Shahzad et al. [203] deposited Fe_2O_3 nanoparticles on the surfaces of $Ti_2C_2T_x$ MXene nanosheets (MGMX) for Hg(II) adsorption. The maximum experimental adsorption capacity for Hg(II) was found to be 1128.41 mg g^{-1}

. The MGMX nanocomposite demonstrated high hydrophilicity, particularly favorable functional groups for M^{2+} ions, high specific surface area, aqueous phase stability, recyclability, and easy separation after interaction with the pollutant. The MGMX nanocomposite was successfully reused in five successive adsorption-desorption cycles, indicating a good adsorbent regeneration capacity.

2.4.1.5 Adsorption of organic pollutants

O. Mashtalir et al. [191] investigated the adsorption of Methylene Blue (MB) dye on ML-$Ti_3C_2T_x$ MXene. The results showed that the adsorption capacity of $Ti_3C_2T_x$ for MB was 39 mg/g, which is lower than that of commercial activated carbon but comparable to other materials with similar structures and surfaces (such as raw kaolinite and commercial clays).

In another study, Zheng Wei et al. [204] modified the interlayer spacing and surface functional groups of $Ti_3C_2T_x$ MXene through an alkaline treatment to enhance its adsorption performance. In this treatment, the interlayer spacing between $Ti_3C_2T_x$ layers was increased by up to 29% with LiOH, 28% with NaOH, and 21% with KOH, and the surface functional groups were adjusted by converting F- to OH-. Among the MX-Alkaline-$Ti_3C_2T_x$ samples, NaOH-$Ti_3C_2T_x$ exhibited the highest adsorption capacity 189 mg/g) with rapid removal of Methylene Blue.

Later, Byung-Moon et al. [205] used MXene in combination with Metal-Organic Frameworks (MOFs) for the adsorption of Methylene Blue (MB) and Acid Blue 80 (AB) and showed that both MXene and MOF exhibited high adsorption capacities for MB (140 mg/g) and AB (200 mg/g).

In another laboratory, Chong Cai et al. [206] demonstrated that the prepared PA-MXene composite exhibited improved adsorption properties for the model dyes MB and RhB, with the adsorption capacity of the PA-MXene composite remaining at approximately 85% after 12 cycles.

Table II. 1: A summary of various studies on MXene application for dye removal.

Dyes	MXene component	Uptake/ efficiency	References
Methylene blue	$Ti_3C_2T_x$	39 mg/g	[191]
Methylene blue	LiOH- $Ti_3C_2T_x$	121 mg/g	[207]
Methylene blue	$Ti_3C_2T_x$	100 mg/g	[207]
Methylene blue	NaOH-$Ti_3C_2T_x$	189 mg/g	[207]
Methylene blue	KOH-$Ti_3C_2T_x$	77 mg/g	[207]
Methylene blue	Phytic acid MXene	42 mg/g	[208]
Methylene blue	MXene	140	[205]
Methylene blue	Surface charged Ti_2CT_x	2460.9 mg/ g	[209]
Methylene blue	F-terminated $Ti_3C_2T_x$	92%	[210]
Methylene blue	h $Ti_3C_2T_x$	24 mg/g	[211]
Methylene blue	MXene-CMC	100%	[212]
Methylene blue	MXene/AAC	311.5 mg/g	[213]
Methylene blue	Sulfonic groups	111.11 mg/	[214]
Methylene blue	MXene/Sodium alginate beads	81.36 mg/g	[215]
Methyl Orange	Sulfonic groups functionalized Mxenes	111.11 mg/ g	[214]
Congo red	MXene/PEI functionalized sodium alginate aerogel	3568 mg/g	[216]
Rhodamine B dye	Phytic acid MXene	22 mg/g	[208]
Neutral red	Poly-acrylic acid MXene	42.50 mg/g	[217]
Safranine T	Poly-acrylic acid MXene	33.76 mg/g	[217]
Malachite Green	$Ti_3C_2T_x$	94.54%	[218]

2.4.2 Energy Applications of MXenes

In a world where we are moving towards sustainable and renewable energy sources, which are inherently intermittent, there is a crucial need to develop more suitable distribution networks with this characteristic of intermittency.

A network with widespread deployment of efficient electrochemical energy storage devices is necessary to enhance operational efficiency and control of energy distribution [183]. Hence, there is an obligation to develop high-performance electrochemical storage systems such as batteries, supercapacitors and fuel cells.

2.4.2.1 Batteries

In order to improve the properties of batteries, a major research focus is the discovery of new materials for electrode fabrication with better capacity, operational potential, capacity ratio, cycle stability and lower cost. Recently, MXenes have shown promising potential as electrodes in lithium-ion batteries due to their layered structure, which allows for reversible Li^+ intercalation, and their versatile compositions, enabling optimization of the electrochemical properties of the battery [219] .

In 2012, Naguib et al. utilized MXene as a negative electrode material for lithium-ion batteries [146]. They assessed the electrochemical properties of non-delaminated Ti_2CT_x. Figure II.10 demonstrates that Ti_2CT_x exhibited a large irreversible capacity during the initial charge, with an initial coulombic efficiency of 45%. Subsequently, it delivered a specific capacity of 150-200 mAh/g at a C/10 rate (~20 mA/g) while maintaining good capacity retention with voltage profile between 0 and 2.0 V vs Li/Li^+.

Gogotsi and Barsoum also investigated the electrochemical properties of non-delaminated Nb_2CT_x and V_2CT_x in a nonaqueous Li^+ electrolyte [155]. both MXenes exhibited specific capacities of 210-220 mAh/g, along with sloping potential profiles resembling those observed for Ti_2CT_x.

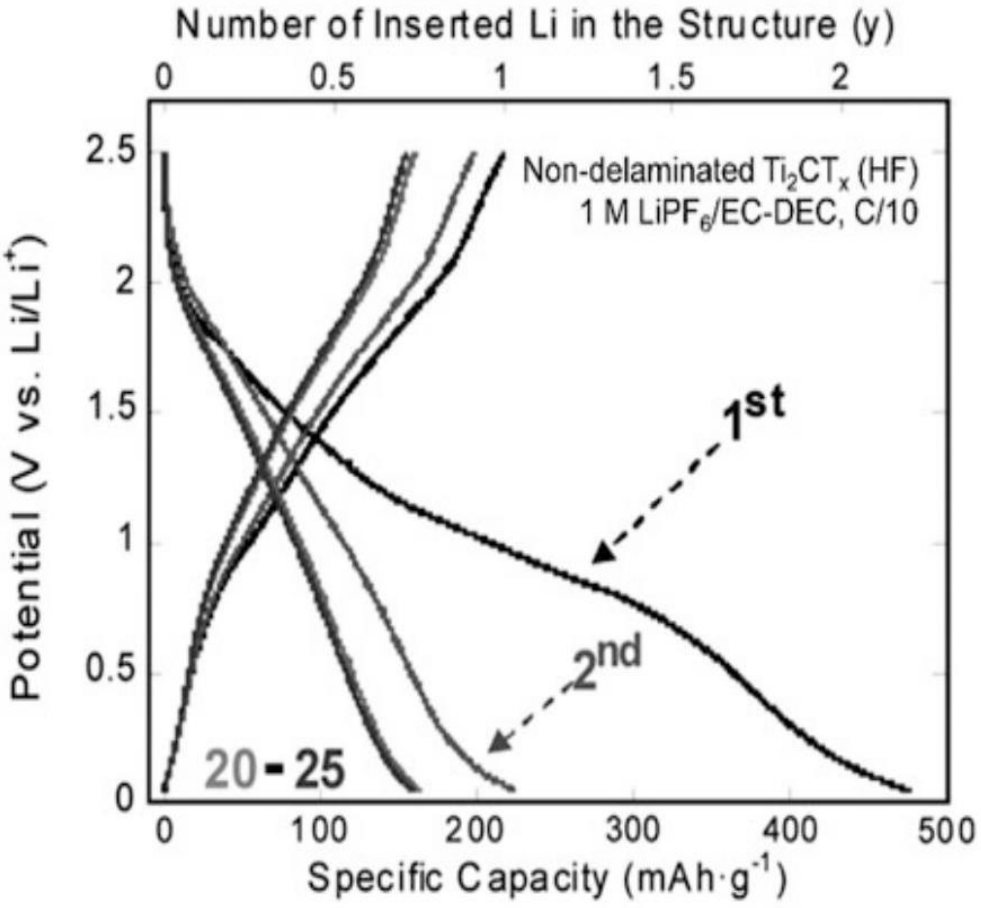


Figure II. 10: Charge-discharge curves of non-delaminated Ti_2CT_x synthesized by HF treatment at C/10 rate in a 1 M LiPF6/EC-DEC electrolyte [146].

Considering that lithium is scarce worldwide, making it costly for large-scale applications, it is crucial to develop batteries using more abundant materials such as sodium. Significant efforts are being directed towards the research of sodium-ion battery electrodes, and the use of MXenes has shown promise in this regard [220] .

Sodium-ion batteries (SIBs) show great potential for large-scale energy storage due to the abundance and low cost of sodium [221]. MXenes and their nanocomposites have emerged as excellent electrode materials for high-performance sodium-ion batteries, offering promising prospects in this field [222] .

When 2D titanium carbide (TiC_3) is reduced to a monolayer thickness, it exhibits a remarkable theoretical capacity of up to 1278 mAh g^{-1}. These distinctive characteristics

establish monolayer TiC_3, a metal-rich MXene, as a highly promising anode material for sodium-ion batteries (SIBs) in comparison to other multilayered MXenes [222].

Based on studies on MXenes as electrodes for electrochemical storage, such as lithium-ion and sodium-ion batteries, the important interlayer spacing of MXenes for ion storage (high energy) and their high electronic conductivity are notable. However, MXenes are characterized by a significant irreversible capacity in the initial cycle, resulting in an initial coulombic efficiency of less than 60%. An interesting alternative to address this characteristic is the control of the MXenes' surface state [223] .

2.4.2.2 Super Capacitor

Supercapacitors store electrical energy in the porous surface of carbon electrodes through the electro-sorption of charge-carrying ions [148] .

MXenes are highly interesting as materials for use as electrodes in supercapacitors, given their excellent electrical conductivity and two-dimensional structure, which enable rapid ion transport and a large accessible surface area for ions [219].

Lukatskaya et al. [224] investigated the effect of electrochemical intercalation of various cations, such as Na^+, K^+, NH^{4+}, Mg^{2+}, and Al^{3+}, on the storage capabilities of $Ti_3C_2T_x$ MXene. By immersing $Ti_3C_2T_x$ MXene in aqueous salt solutions, spontaneous intercalation of cations was achieved.

This led to a significant increase in capacitance, with the $Ti_3C_2T_x$ electrode exhibiting approximately 300 Fcm^{-3}, surpassing the capacitance values of porous carbon materials. These findings prompted researchers to explore the potential of MXenes in supercapacitors [182]

$Ti_3C_2T_x$ loaded onto silk-derived carbon cloth was utilized as an electrode material for flexible supercapacitor fabrication. It exhibited an areal capacitance of 362 $mFcm^{-2}$, demonstrating excellent flexibility and cyclic stability [157] . MXene-based supercapacitors have consistently shown excellent cyclic stability due to the strong M-X bond and superior specific capacitance [157,225,226]

Dall'Agnese et al. investigated the effect of chemically modified surfaces of $Ti_3C_2T_x$ MXenes with dimethyl sulfoxide (DMSO). The introduction of oxygen terminations on the surfaces improved the specific capacitance of these materials. When tested in H_2SO_4 acid

electrolyte, $Ti_3C_2T_x$ MXene exhibited a capacitance of 415 Fcm^{-3} at 5 Ag^{-1}, with no significant degradation observed even after 10,000 cycles [227].

2.4.2.3 Electromagnetic Interference Protection System

into avoid electromagnetic interference pollution (EMI) [228,229] . which pose a significant impact on human health, with a potential risk of long-term exposure to EMI leading to cancer [183,219]

there is a need to minimize these interferences through EMI protection systems, [228,229]. by using materials with high electrical conductivity. MXenes with their excellent electrical conductivity emerge as potential candidates for EMI shielding applications [230].

Shahzad et al. [231] mentioned three types of MXenes films ($Ti_3C_2T_x$, $Mo_2Ti_2C_3T_x$, and $Mo_2TiC_2T_x$) that demonstrate excellent performance as EMI protection systems, Liu et al. [232] presented a simple and effective method for producing freestanding, flexible, and lightweight $Ti_3C_2T_x$ MXene foams with satisfactory mechanical strength and low density. MXene foams demonstrated higher electromagnetic interference shielding effectiveness (EMI SE) values compared to their bulk counterparts.

2.5 Summary:

Through this literature review chapter on MXenes, we have been able to demonstrate the richness of this new class of 2D materials, they are derived from layered ternary carbides, nitrides, or carbonitrides known as MAX phases through a selective etching process. MXenes exhibit excellent electrical conductivity, mechanical strength, high surface area, Tunable surface chemistry, Selectivity, Regeneration and Stability that make them excellent candidates for adsorption applications and author applications such as energy storage, catalysis, sensing and electromagnetic shielding.

3. Chapter 3: Materials and methods

3.1 Chemical products

All chemical products used during this study are regrouped in Table III.1.

Table III. 1 : Characteristics of the powders used.

	Source	**Purity %**
Chromium (Cr)	Biochem	99.5
iron (Fe)	Biochem	99.5
aluminum (Al)	Biochem	98
graphite (C)		98
boron (B)	Alpha Aesar	95
Tin (Sn)	Biochem	98.9
Potassium bromide KBr	Honeywell	99,9
sodium chloride NaCl	Honeywell	99.5
Potassium chloride KCl	Honeywell	99.5
Sodium bromide NaBr	Honeywell	99
hydrofluoric acid HF	Biochem	43
Sulfuric acid H_2SO_4	Honeywell	97
Hydrochloric acid HCl	Biochem	35
Sodium hydroxide NaOH	Honeywell	99.8

3.2 Synthesis of MAX and MAB phases

MAX or MAB phase was synthesized using a mixture of M= (Fe,Cr) , A=(Al) , (C ,B) and Sn . Salt like KBr, NaCl, NaBr and KCl in a 1:1 weight ratio was added to the resulting mixture.

The syntheses are carried out from the commercial powders described in Table III. 1 without further purification steps.

The starting powders were initially mixed using an agate mortar for 1 h. As shown in Figure III.1a, the powders were uni-axially cold pressed in a stainless-steel die under 200 MPa pressure to form compacts of 16 mm diameter and 5 mm height. The compacts were further encapsulated with KBr or (KCl, NaCl, NaBr) salt in a larger steel die of 32 mm diameter as showed in Figure III.1b.

Shortly after, the sample was emerged in a KBr salt bed inside a cylindrical alumina crucible (as depicted Figure III.1c) to avoid oxidation.

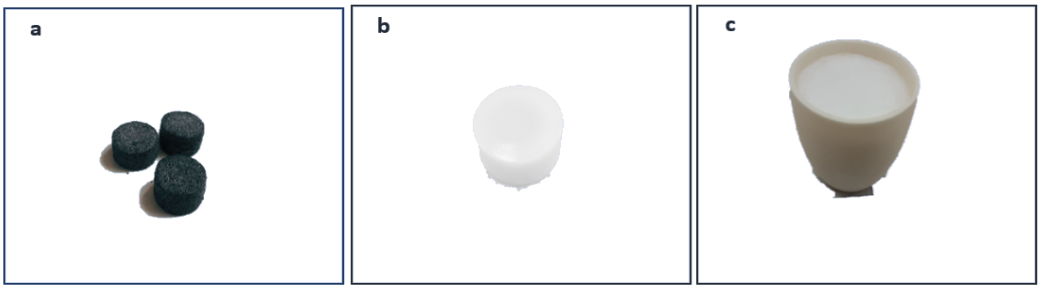


Figure III. 1 : Step used in MAX and MAB phases synthesis. (a) Compact powder of MAX and MAB phases, (b) Encapsulated compact powder with salt (KCl or KBr, NaBr and NaCl), (c) Salt bed in cylindrical alumina crucible,

The samples were heated in a resistance furnace (NABERTHERM B180), in an open-air atmosphere at a 900-1200 °C temperature range. The heating rate was 5 °C min^{-1} until reaching the synthesis temperature and held for 1 h. The samples were allowed to cool inside the furnace until room temperature.

To collect the Cr_2AlC and Fe_2AlB_2 powders, the alumina crucible was submerged in boiling distilled water inside a beaker. After salt dissolution, the remaining solution was stirred for 1 h. The powder was then filtered, washed five times with deionized water, and dried at 80 °C for 18 h. All the synthesis steps are illustrated in Figure III.2.

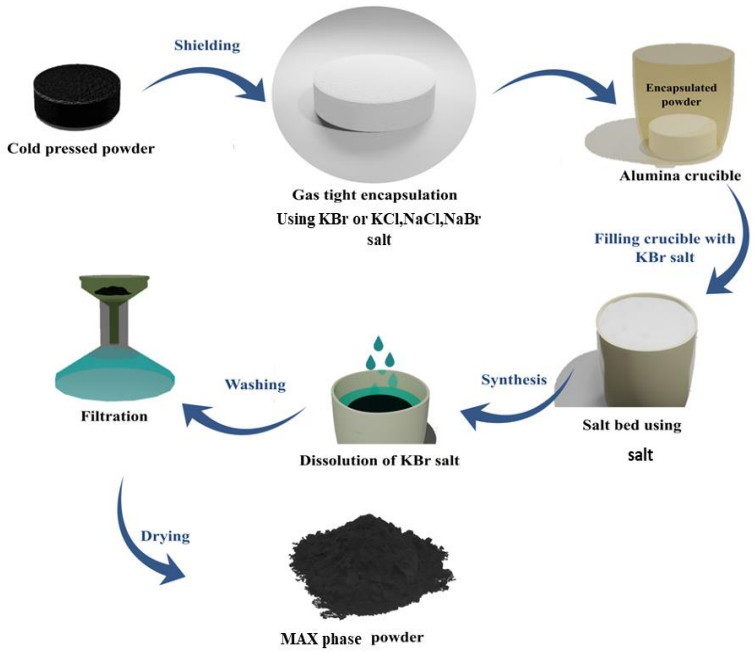


Figure III. 2: Schematic view of the MAX and MAB synthesis by the Molten Salt Shielded Synthesis "MS[3]" process using KBr or KCl, NaCl, NaBr.

3.3 Initial mixture powders composition

The following table presents the stoichiometry of the initial powder mixture with an excess of Al is often used in the synthesis of MAB and MAB phases. It minimizes the content of byproducts and compensates for its loss due to high-temperature evaporation [140].

Table III. 2: Proportions used in the initial powder mixtures.

	Salts	**Molar ratio**
Fe_2AlB_2	KBr	Fe=2, Al=2, B=2
		Fe=2, Al=2, B=2 and Sn=0.2
Cr_2AlC	KBr	Cr=2, Al=1.2, C=1
	KCl	
	NaBr	
	NaCl	

3.4 Preparation of MXenes

3.4.1 Synthesis of Cr_2CT_x

Cr_2CT_x was elaborated according to reference [233]: A mixture of 75,5 mL of 2M H_2SO_4 solution and 2.2 g of LiF were stirred for 5 min to get a homogenous solution. 3.3 g of Cr_2AlC were added into to the mixed (LiF and H_2SO_4) solution gradually to avoid the violent exothermal reaction, and then the system was allowed to react for 30 minutes with magnetic stirring in an oil bath at 30 °C. Ultrasonication assistance was used to disperse the powder in deionized water and ethanol. The resultant suspension was washed at least five times using deionized water and ethanol with separating powder from supernatant at 4000 rpm centrifugation for 6 min for each washing operation. Finally, the hydrous sediment was dried at 80 C for 24 h.

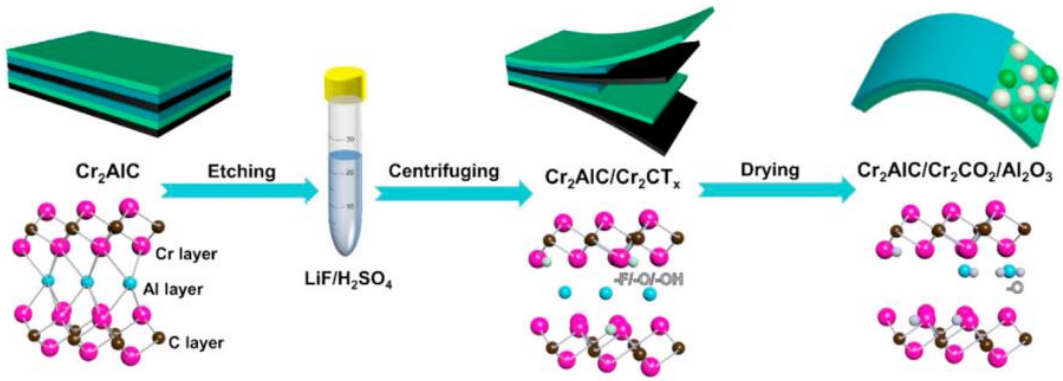


Figure III. 3: The proposed schematic illustrates the etching process from Cr_2AlC MAX phase to Cr_2CT_x MXene [233]

3.4.2 Synthesis of $Ti_3C_2T_x$

3g of Ti_2AlC was immersed in 60 mL of 40 wt% hydrofluoric acid and the mixture was stirring for 2 h. The resultant suspension was then washed with distilled water and centrifuged to remove the remaining impurities and HF until the solution reached a pH of 5−6, after that, the wet sediment was washed twice using ethanol. The final product was dried in a vacuum oven at 50 °C for 24 h.

3.5 Characterizations of MXene, MAX and MAB phase

3.5.1 X-Ray Diffraction (XRD)

In our work we have used a Panalytical X'pert Pro diffractometer with Cu-Kα radiation 1.54Å) and a step of 0.02° at CRTI, Chéraga. The samples to be analyzed are treated under a range of 2θ going from 0 to 90°

3.5.2 Scanning electron microscope

The scanning electron microscope used for this thesis is (Quanta 650), equipped with an EDS, (Brucker X-Flash 6/10) for morphological and phase analysis. EDS analysis was performed using 10Kv voltage and 90s acquisition time.

3.5.3 Thermogravimetric and differential thermal analysis (TGA), (DTA).

TG-DTA modes can be used to determine the following:

• Melting points

• Glass transition temperatures

• Crystallinity

• Moisture/ volatile content

• Thermal and oxidative stability

• Purity

• Transformation temperatures

The apparatus used was SETARAM Labsys EVO in the temperature range of 50-1200 °C under N_2 gas and using 10 °C/min heating rate.

3.5.4 BET Analysis.

The procedure implies the determination of the volume of nitrogen needed to create a monolayer of nitrogen molecules on the sample's surface. The principle is based on a gas adsorption theory (multilayer isotherm) developed by Brunauer, Emmett, and Teller in 1939.

The measurement is carried out using a Quantachrome Instruments version 5.2 apparatus. Before each test, the materials undergo degassing at 150°C for 5 hours.

3.5.5 Determination pf pH_{pzc}

The pH of the point of zero charge (pHpzc) is defined as the pH at which the net surface charge of a solids is zero. This means that the positive and negative charges on the surface are balanced, resulting in an absence of electrostatic force on the ions in solution that interact with the solid surface.

The pHpzc depends on several factors, including the nature of the solid surface, the concentration and nature of ions in the solution, temperature, etc.

Generally, pHpzc is experimentally determined by measuring the electric charge of the solid surface at different pH values and plotting a charge curve or zeta potential curve. It is important to know the pHpzc because it allows us to understand the behavior of the solid surface in the presence of acidic or basic solutions. If the pH of the solution is lower than the pHpzc, the solid surface will have a net positive charge, which will favor the adsorption of anions and repulsion of cations. If the pH of the solution is higher than the pHpzc, the solid surface will have a net negative charge, which will favor the adsorption of cations and repulsion of anions.

The acid-base properties of the prepared MXenes, MAX and MAB phases powders were determined by potentiometric titration according to the Kummert and Stumm protocol [234].

Titration was carried out using hydrochloric acid HCl (0.01 M) and sodium hydroxide NaOH (0.01 M). The solution to be titrated (100 mL of distilled water containing MXenes, MAX and MAB phases) was then titrated with HCl or NaOH. pH monitoring was done using a pH meter (OHAUA STARTER 2100).

The surface acidity constants were determined using the surface complexation model which is based on the Gouy-Chapman double layer theory. It shows that the electrostatic surface charge of the solid results from surface acid-base reactions.

These reactions are described only by the mass conservation equation based on the surface hydroxyl groups and which are determined by analogy with amphoteric compounds [235,236].

$$[S\text{-}OH_2^+] \Leftrightarrow SOH + H^+$$

$$SOH \Leftrightarrow SO^- + H^+$$

$$Ka_1 = [H^+].[SOH]/[S - OH_2^+] \ldots\ldots\ldots\ldots\ldots\ldots \text{III.1}$$

$$Ka_2 = [H^+].[SO^-]/[S - OH] \ldots\ldots\ldots\ldots\ldots\ldots\ldots \text{III.2}$$

The total number of surface sites

$$[S]tot = [S^-OH_2^+] + [S\text{-}OH] + [S\text{-}O^-] \ldots\ldots\ldots\ldots \text{III.3}$$

It is then possible to determine the pHpzc, which is the pH at which the charge of the solid is overall neutral.

$$pH_{pzc} = ½ (pKa1 + pKa2) \ldots\ldots\ldots\ldots\ldots\ldots\ldots \text{III.4}$$

For each acid-base titration point, the surface charge QS is obtained:

$$Qs = \frac{Ca - Cb + [OH-] - [H+]}{m} \ldots\ldots\ldots\ldots\ldots\ldots\ldots\ldots\ldots\ldots \text{III.5}$$

Where the following parameters represent:

Q_S: Surface charge in mol. g^{-1}.

C_a: Concentration of acid added in mol. L^{-1}.

C_b: Base concentration added in mol. L^{-1}.

m: mass in g.

Or respectively for an addition of acid or base:

$$Qs = \frac{Ca + [OH] - [H+]}{m} \ldots\ldots\ldots\ldots\ldots\ldots\ldots\ldots \text{III.6}$$

$$Qs = \frac{-Cb + [OH-] - [H+]}{m} \ldots\ldots\ldots\ldots\ldots\ldots\ldots \text{III.7}$$

So the average surface charge of the solid can be obtained as a function of pH [237].

3.6 Adsorption of Malachite Green

In this study, the effectiveness of the MAX, MAB and MXenes phases is achieved through the adsorption of Malachite Green (MG) chosen as a pollutant. MG is generally used in the treatment of parasites, fungal infections and bacterial infections in fish and their eggs. It is a toxic chemical primarily known for its blue-green dye qualities.

From a chemical point of view, it is considered to be a cationic (or basic) dye of the chemical class triphenylmethane and having a chemical formula $C_{23}H_{25}N_2Cl$.

The MG used (Fluka AG) is soluble in water in the form of oxalate. Its semi-developed formula is as follows:

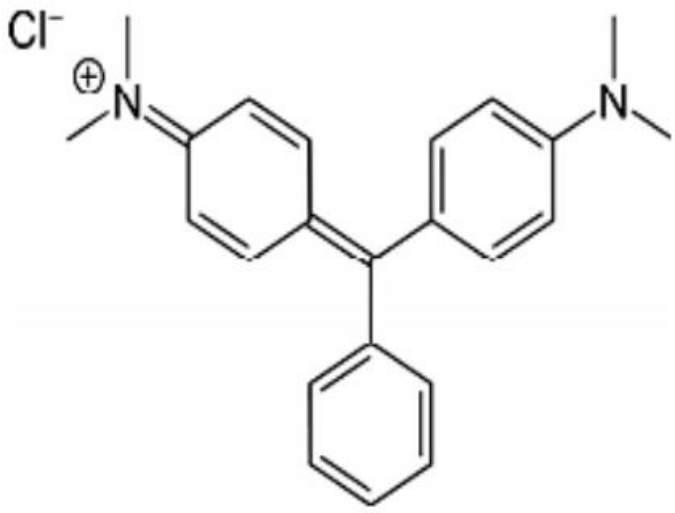


Figure III. 4 : Structure of Malachite Green used.

3.6.1 Preparation of the calibration curve of MG

The method used to establish the calibration curve for MG involves first preparing a stock solution with a concentration of 0.1 g/L, from which we prepare a series of daughter solutions with well-defined concentrations (ranging from 1 to 10 mg/L) through successive dilutions, all at the same pH.

The calibration curve can be found in Annex 1

3.6.2 UV-Vis absorption of MG

The residual concentrations of VM are determined by spectrophotometric analysis in the visible range. The UV-visible spectrophotometer used is a (UV-1700 pharma spec / Shimmadzu) equipped with a quartz cuvette of 1 cm width.

The MG strongly absorbs in the visible range of the spectrum at a maximum wavelength of 617 nm.

3.6.3 Adsorption kinetics

The adsorption study was conducted in batch mode at room temperature . The operation consists in mixing in a series of flasks (Capacity of 250 mL) 10 mg of sorbent (Cr_2AlC, Ti_3AlC_2, Fe_2AlB_2, Cr_2CT_x, $Ti_3C_2T_x$) and a series of 50 mL of MG aqueous solution (10 mg/L) in dark environment.

All flasks are shaken at 225 cpm in a shaking table (Edmund Bühler GmbH)(225r/min) at pH (6). Samples of 10 mL of solution are taken and then filtered with a 0.45 µm hydrophilic polyvinylidene fluoride syringe filter.

The sorption efficiency of the MG dye as a function of time is evaluated using Equation III.8. The corresponding removal capacity (q_t , mg/g) is estimated using Equation III.9.

$$\% \, adsorption = \frac{Co - Ct}{Co} \quad \text{.....III.8}$$

$$qt = \frac{V \times (Co - Ct)}{m} \quad \text{.....III.9}$$

Where Co and Ct represent the concentration of the MG dye at time zero and any time, respectively, in the solution (mg/L), V is the volume of the solution (L), and m is the sorbent dose (g).

3.6.4 Effect of pH

A series of seven identical suspensions of MG solutions at 10 $mg.L^{-1}$ and 0.01 g of sorbent are prepared at different pHs ranging from 2 to 10 by adding either a few drops of 0.1M HCl or 0.1M NaOH.

All these suspensions are subjected to stirring at 225 cpm for a period of 24 h at room temperature. Samples of these suspensions are filtered with a 0.45 µm hydrophilic polyvinylidene fluoride syringe filter and then analyzed by UV-visible spectrophotometer at 617 nm.

3.6.5 Effect of initial concentration

In order to verify the effectiveness of the MAX, MAB phases and their byproduct towards MG molecules in low or high concentration solutions, this study was carried out by examining the effect of the concentration ranging from 10 to 100 $mg.L^{-1}$ of a series of Five suspensions (0.01g of adsorbent in 50 mL of MG solution).All mixtures are kept in shaker for 20h at room temperature .

The solution mixtures were taken and filtered with a 0.45 µm hydrophilic polyvinylidene fluoride syringe filter and analyzed in UV-visible spectrophotometer at 617 nm.

3.6.6 Adsorption Isotherms

The MG sorption isotherms were obtained using the same conditions of temperature, stirring speed, darkness, suspension filtration, spectrophotometric analysis, etc. used in the kinetic study. The tests are carried out by mixing in dark environment a series of five quantities of sorbent varying from 10 to 100 mg into flaks to which are added identical volumes of 50mL of MG (10 $mg.L^{-1}$). These bottles are subjected to the same agitation for a period of 20 hours.

3.6.7 Adsorption Modeling

3.6.7.1 Modeling Adsorption Kinetics

modeling adsorption kinetics involves describing and predicting how the adsorption of a solute onto an adsorbent material change over time. Different models are used to understand and quantify the rate at which adsorption occurs. Two common kinetic models are the pseudo-first order and pseudo-second-order models:

a) pseudo-first order

In this model, it is assumed that the adsorption rate at time t is proportional to the difference between the quantity adsorbed at equilibrium, Q_e, and the quantity Q_t adsorbed at that moment, and that adsorption is reversible. Many authors have used this kinetic model to describe the adsorption of organic and inorganic solutes on heterogeneous solid surfaces. The first-order kinetic rate constant, K_1, is deduced from the model established by Lagergren[238].

This equation in its nonlinear form is written as follows:

$$Q_t=Q_e=(1-e^{-K_1 t}) \quad \text{.....III.10}$$

Where:

Q_e and Q_t represent, respectively, the quantities of the adsorbed pollutant at equilibrium and at time "t" per gram of adsorbent in mg.g-1.

K_1 represents the first-order kinetic rate constant of the chemical reaction in time^{-1}.

b) pseudo-second order

The equation of the pseudo-second order is often successfully used to describe the kinetics of pollutant adsorption on the adsorbent [239]. This irreversible model allows for characterizing adsorption kinetics by taking into account both the case of rapid binding of solutes to the most reactive sites and that of slow binding to low-energy sites. The model equation can be written in the following form:

$$Q_t=\frac{Qe^2 K_2 t}{1+Qe^2 K_2 t} \quad \text{.....III.11}$$

Where:

K_2 represents the kinetic constant of order 2 of the chemical reaction in g.mg^{1}. time^{1}.

3.6.7.2 Adsorption Equilibrium Modeling

Among the models representing the equilibrium relationship between the adsorbed quantity Qe and the solute concentration in solution Ce, two classic models can be mentioned: these are the Langmuir and Freundlich models.

a) Langmuir Adsorption Isotherm

The Langmuir model assumes that the surface of the adsorbent is homogeneous in terms of energy and does not take into account interactions between adsorbed molecules [240] . At equilibrium, the equation of the Langmuir model is given as follows:

$$Q_e = (K_L \times Q_m C_e)/(1+K_L Ce) \text{……..III.12}$$

Where the following parameters represent:

- Q_m: Maximum adsorption capacity in $mg.g^{-1}$.
- K_L: Ratio of the adsorption and desorption rate constants in $L.mg^{-1}$.

b) Freundlich model

The Freundlich model is semi-empirical. It assumes of a heterogeneous surface of the adsorbent with an exponential distribution of active sites based on adsorption energies[240]

. The equation of the model is written as follows:

$$Q_e = K_F \times Ce^{1/n} \text{……III.13}$$

Where the following parameters represent:

K_F: Parameter related to adsorption capacity in $mg^{1-1/n}. L^{1/n}. g^{-1}$.

1/n: Parameter related to the distribution of adsorption energies.

These Freundlich parameters are characteristic constants of the (adsorbent/adsorbate) pair, experimentally determined at a given temperature. However, this model does not assume the existence of a maximum adsorption capacity. It is limited to dilute environments and only takes into account adsorbate-adsorbent interactions. The coefficient 1/n is a measure of the intensity of adsorption or surface heterogeneity. Therefore, if 1/n = 1, the partition between the two phases is independent of concentration. On the other hand, if 1/n < 1, adsorption is quantitatively more significant, and for 1/n > 1, the intensity of adsorption is weaker.

For this study, we conducted the modelling of our experimental results through nonlinear regressions using Pro ORIGIN 2022 software.

4. Chapter 4: Results and discussion

This chapter represents the most important results of this thesis. which are divided into three parts:

The first part focuses on studying the synthesis of MAB and MAX phases. We investigated the impact of temperature and the addition of Sn during the synthesis of Fe_2AlB_2 using the molten salt shielded sintering method with KBr salt. Additionally, we examined the influence of salts and temperature on the synthesis of Cr_2AlC.

The second part of this chapter discusses the synthesis of two-dimensional materials MXenes, specifically Cr_2CT_x and $Ti_3C_2T_x$.

The third part explores the application of these materials in the removal of malachite green through adsorption method.

4.1 Synthesis of MAB and MAX phases

4.1.1 Synthesis of MAB phases

In the Figure IV.1, it is evident that when the sample is taken out of the furnace, the salt effectively covers the sample. This indicates that the salt has prevented air from entering the sample. Once the salt is melted in a beaker, the MAB phase is observed to have a slightly brownish gray color. This implies that there has been no oxidation (orange color), confirming that KBr is a reliable air-tight salt.

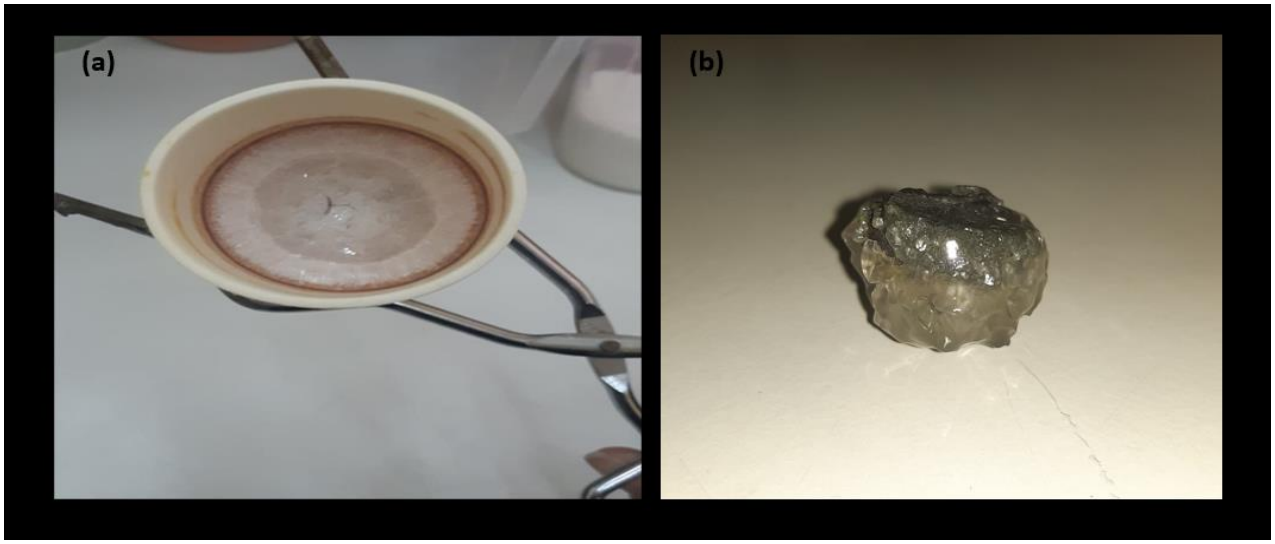


Figure IV. 1: Digital photographs showing (a): sample Fe_2AlB_2 taken from the oven, (b): the sample of Fe_2AlB_2 after salt removal.

4.1.2 Characterization of MAB phases

4.1.2.1 X-Ray Diffraction (XRD)

4.1.2.1.1 Effect of temperature and Sn additive on Synthesis of Fe_2AlB_2

Figure IV.2 shows the X-ray diffraction analysis of the synthesized Fe_2AlB_2 powder starting from Fe/Al/B (2/2/2, molar ratio). The temperature varied between 900 °C to 1200 °C with (Fig IV. 2a) and without (Fig IV.2b) Sn addition. For the synthesized sample at 900 °C using 0.2 Sn, the pattern shows two major phases: FeB and $FeAl_6$ (FigIV.2a). Some peaks of Fe_2AlB_2 and Sn are also present. At 1000 °C, the XRD revealed successful synthesis of predominantly single-phase Fe_2AlB_2 powder in the Fe-Al-B system. Fe_2AlB_2 is the predominant phase, accompanied by Sn.

When rising temperature up to 1100 °C, Fe_2AlB_2 is still the major phase. However, some small peaks of FeB and $FeAl_6$ are present. Up to 1200 °C, even though Fe_2AlB_2 was predominant, it is discernible that FeB and $FeAl_6$ peaks intensity increased. According to the

above results, it can be concluded that highly pure Fe_2AlB_2 powder is synthesized using Fe/Al/B/Sn mixture at 1000 °C.

To confirm the influence of Sn powder on the Fe_2AlB_2 formation, a mixture of 2Fe/2Al/2B was heated by keeping the same previous conditions (without using Sn additive). The formation of Fe_2AlB_2 starts at 900 °C. However, the major phases are FeB and $FeAl_x$, as shown in Fig IV.2b. For the samples produced at 1000 °C and 1100 °C, a large quantity of unreacted FeB, Fe_2B, and $FeAl_x$ remained in the samples with relatively higher Fe_2AlB_2 content. Increasing temperature up to 1200 °C showed a continued consumption of FeB, $FeAl_x$, and Fe_2B, as shown by the decrease of the intensities of respective phases peaks. The major phase, in this case, was Fe_2AlB_2, as shown by its relatively higher peak intensities.

Based on the aforementioned results, it is reasonable to conclude that even at 1200 °C, the reaction is still in progress. Knowing that the synthesis of single-phase Fe_2AlB_2 requires a very long time to be achieved [15], according to the present XRD results, as shown in Fig IV.2a, the sample synthesized by adding Sn powder was nearly single-phase Fe_2AlB_2. The powder was obtained at the lowest temperature and time reported to date. Recently, M. Dey et al. [15] reported that Fe_2AlB_2 could be produced in a KBr salt bath at 1000 °C. Yet, it took 12h synthesis time to be achieved in a single phase. It must be noted that in their report, the synthesis was done without salt assisting. The salt was used only to protect initial powders from oxidation and was not mixed with reactive powders.

It can reasonably be concluded that the Sn additive played a major role during Fe_2AlB_2 formation, as seen by the increased reactivity of the starting powders. Our results are in contestation with the study done by Jie Lui et al. [12]. They studied the effect of Sn on the final purity of the Fe_2AlB_2 phase using a mixture of 2Fe/xAl/2B/0.2 Sn, where (x=1, 1.3, and 1.5). They concluded that the Sn additive could not effectively improve the purity of Fe_2AlB_2. Their

conclusion was based only at one synthesis temperature (at 1150 °C for 1h). Besides, they used a smaller amount of Al in the starting powders, without salt assisting. Other conditions compared to Jie. Liu et al. [12] work might have influenced the Fe_2AlB_2 formation: 1) the difference in initial powder granulometry; 2) the reaction medium (the KBr salt bath and its presence in the initial reactive powders); 3) the heating rate.

We have shown in our XRD results (Fig IV.2b), up to 1100 °C, some peaks of FeB and $FeAl_x$ appear and increase with further increase in temperature. It probably means that Fe_2AlB_2 started decomposing [11], which is likely the case in Jie Lui et al. study [12]. Hence, it is reasonable to conclude that Sn powder is an effective synthesis aid that accelerates the formation of Fe_2AlB_2 using the MS^3 process. The Fe_2AlB_2 powder produced using this method is less expensive than pressureless sintering using an argon atmosphere and provides a higher-purity product in a shorter time. To put it in perspective, the cost of a bottle of argon, which lasts for 7 days, is approximately 200,000 Da, whereas 1 kg of KBr is only 1,200 Da.

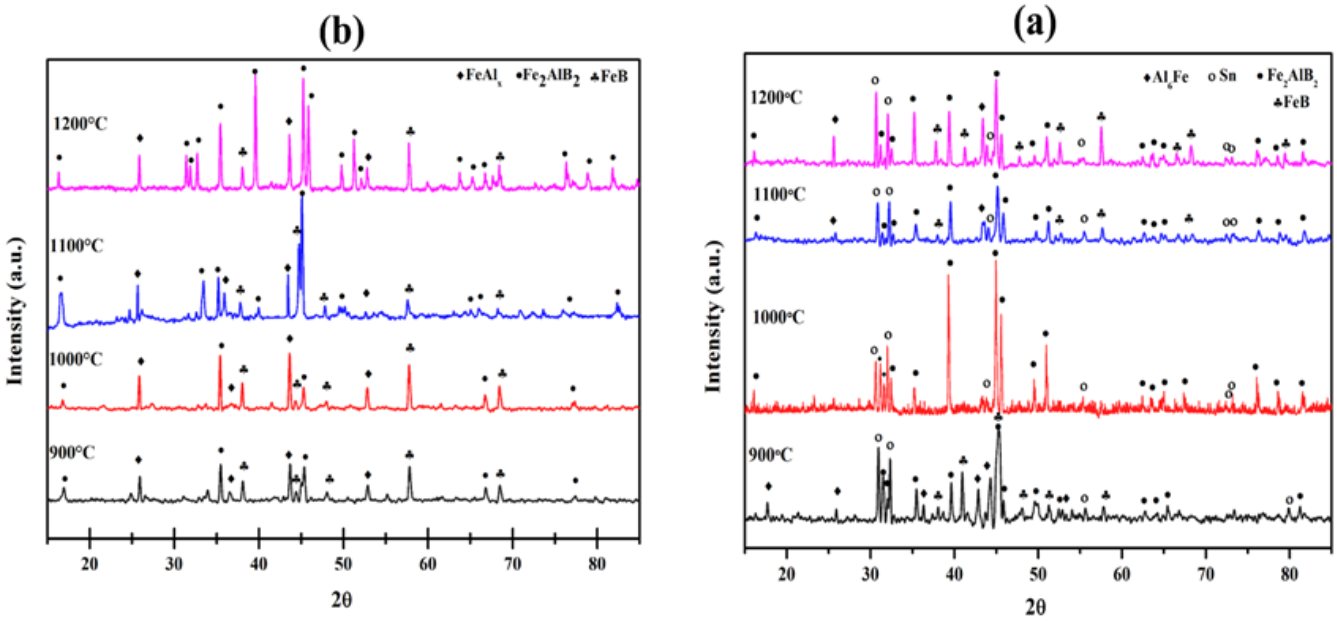


Figure IV. 2 :XRD patterns of (a) 2Fe/2Al/2B/0.2Sn mixture and (b) 2Fe/2Al/2B mixture, synthesized by the MS^3 process using KBr salt at 900, 1000, 1100, and 1200 °C, for 1h synthesis time.

4.1.2.2 Thermogravimetric and differential thermal analysis (TGA),(DTA)

The Fe_2AlB_2 formation mechanism, TDA/TGA curves in the 200-1200 °C temperature range are shown in Fig IV.3. For the Fe/Al/B/Sn mixture, there are two endothermic and three exothermic peaks, as shown in Fig IV.3.a. The first endothermic peak is observed at 230 °C, which corresponds to the melting point of Sn. While the second peak, around 738 °C, corresponds to the melting point of potassium bromide. Besides, the two exothermic peaks, at 511 °C and 641 °C, could be attributed to the formation of Fe-Al and Fe-B phases, respectively [241]. The last exothermic peak at 1170 °C could probably indicate the decomposition of the Fe_2AlB_2 phase [242]. On the other hand, the synthesized sample without using Sn additive Fig IV.3.b has one endothermic peak at 740 °C, which corresponds to the melting point of KBr. The two exothermic peaks at 613 °C and 727 °C might be assigned to Fe-Al and Fe-B temperature formation respectively.

The synthesis reaction of Fe_2AlB_2 starts by Al reacting with Fe to form the $FeAl_6$ phase, as shown in Eq. (IV.1). This reaction took place below the melting temperature of Al. It might explain the absence of the endothermic peak of the Al melting point (667 °C) in the TDA/TGA curves (Fig IV.3). Subsequently, Fe reacts with B to form the FeB phase (Eq. IV.2). Both phases were seen to react at lower temperatures than reported earlier[241]. This was probably triggered by the presence of both KBr salt and Sn additive in the reaction medium.

$$Fe + 6Al = FeAl_6 \quad \text{……...……IV.1}$$

$$Fe + B = FeB \quad \text{…….....…IV.2}$$

Fe_2AlB_2 phase is formed by the consumption of $FeAl_6$ intermetallic and FeB according to Eq. (IV.3).

$FeAl_6 + 11FeB + B = 6Fe_2AlB_2$ ……IV.3

Our results agree with a previously reported study on the Fe_2AlB_2 formation mechanism [95]. The Fe_2AlB_2 reaction path consists of the consumption of transient phases (FeB, Fe_xAl_y, and B) to form the Fe_2AlB_2 phase. Even though the authors used FeB and Al powders as starting reactants, Al did not intercalate into the FeB structure. Al and iron boride reacted to form Fe_4Al_{13} intermetallic, leaving free boron and remaining FeB phase.

Previously, it was shown that the KBr molten salt accelerates the reaction of several MAX and MAB phases [18]. According to the present TDA results, the formation of Fe-Al intermetallic and Fe-B in the sample with the Sn presence (Fig.IV.3a) did form at lower temperatures (511 °C and 641 °C, respectively) compared to the sample synthesized without Sn (613 °C and 727 °C, respectively). Hence, it is reasonable to conclude that the Sn additive is a good choice to lower the formation temperature of the Fe_2AlB_2 compound since it decreases the formation temperature of its reactive intermediate phases ($FeAl_6$ and FeB).

TGA curves (Fig IV.3c and IV.3d) show a decrease in mass of both samples (2Fe/2Al/2B/Sn and 2Fe/2Al/2B) by about 50% during heating above 740 °C, which is mainly caused by the evaporation of liquid KBr. After the loss of all KBr, the weight of both samples is stable [18].

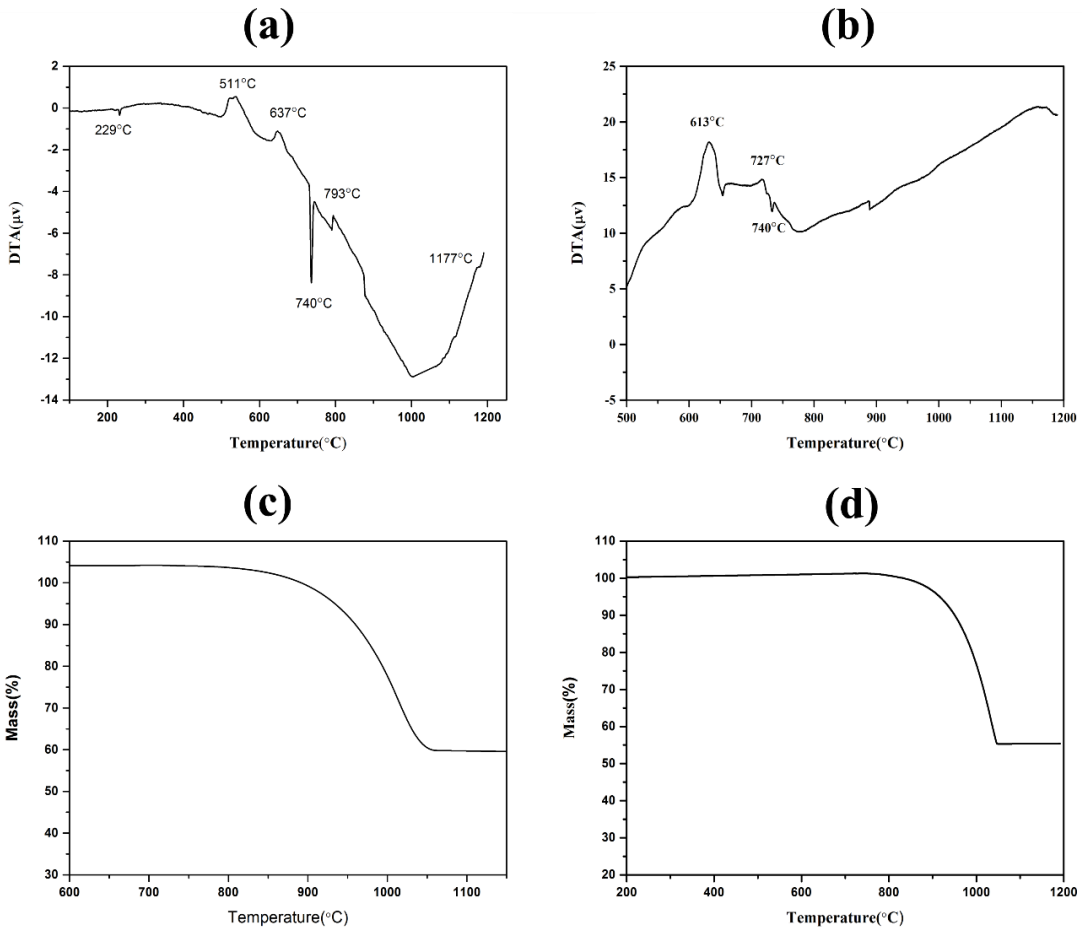


Figure IV. 3: DTA curves of (a) 2Fe/2Al/2B/0.2Sn, (b) 2Fe/2Al/2B initial powder mixtures. TGA curves of (c) 2Fe/2Al/2B/0.2Sn, and (d) 2Fe/2Al/2B initial powder mixtures.

4.1.2.3 Scanning electron microscopy of MAB phase

4.1.2.3.1 Synthesis of Fe_2AlB_2 without Sn additive

SEM micrographs of the synthesized sample at 1200 °C without Sn addition are shown in Figure IV.4. Fe_2AlB_2 particles are randomly shaped, with traces of spindles identified by EDS as $Fe_xAl_yO_z$ (Spinel oxides). Moreover, elemental mapping conducted on the same area (Fig IV.8b-5d) confirms the successful synthesis of the Fe_2AlB_2 phase.

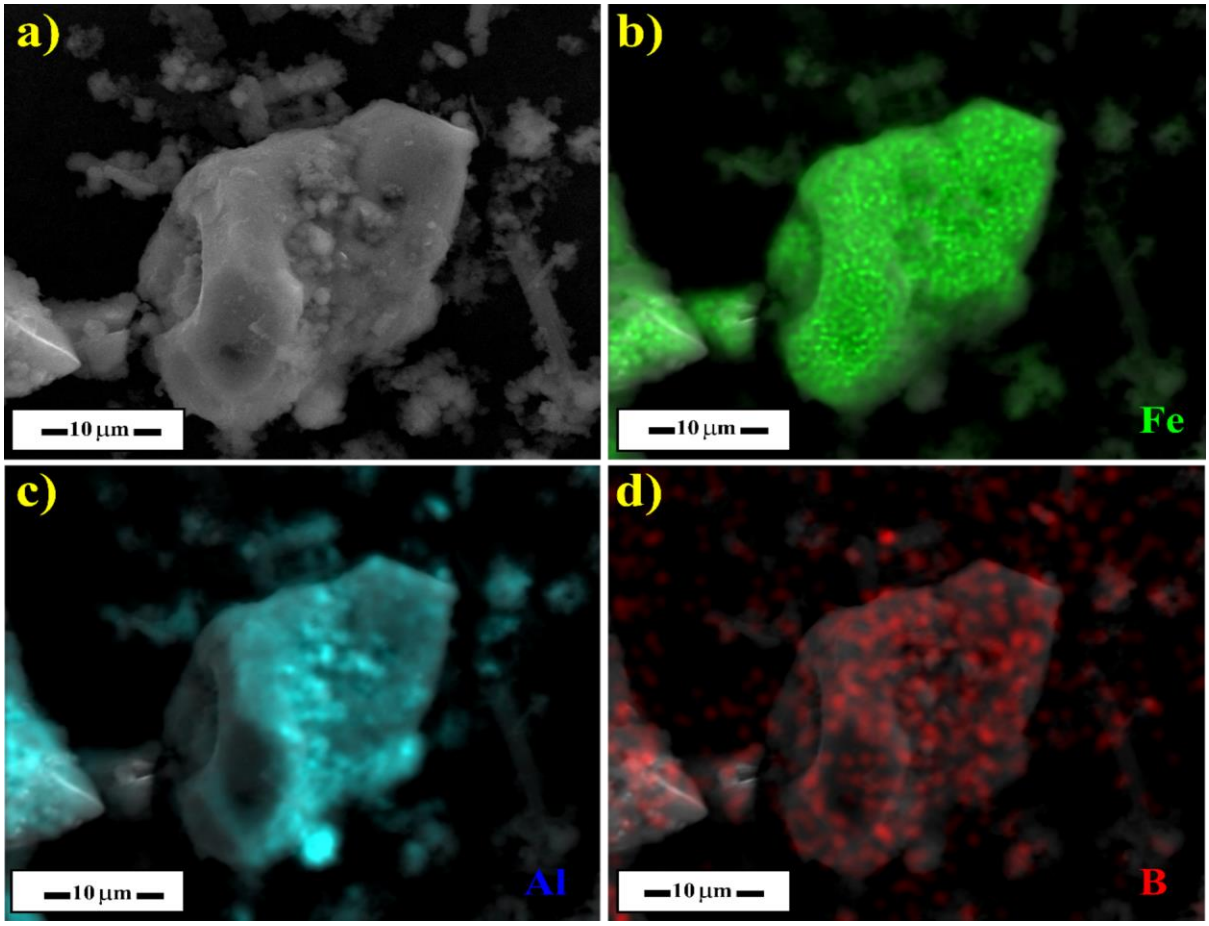


Figure IV. 4 : SEM micrographs of synthesized Fe_2AlB_2 powder at 1200 °C prepared starting from 2Fe/2Al/2B, without Sn additive. SEM-EDS elemental mapping of (b) iron, (c) aluminum and (d) boron.

4.1.4.1.1 Synthesis of Fe_2AlB_2 with Sn additive

Figure IV.5 shows SEM micrographs of the sample synthesized at 1000 °C with Sn addition. The synthesized powders have a sub-spherical shape with an average particle size of 60 µm, as shown in Fig IV. 5a. Higher magnification of X area (Fig IV. 5b) shows the sub-spherical powders to be agglomerates of smaller particles bindered together by what resembles to a re-solidified phase. EDS analysis (spot B), conducted on the latter, revealed it to contains mostly Sn (Sn 95 at. %, Al 3 at. %, Fe 1.5 at. %, and B 0.5 at. %). Note that EDS is not effective in quantifying boron accurately [243,244].Moreover, spot C (small particles) contain Fe, Al, and B. For a better presentation, EDS- Elemental mapping was performed on the sample. It shows elements distribution of Fe, B, Al, and Sn, in Fig IV. 5c-5f, respectively. It gives a clearer view of Fe_2AlB_2 particles surrounded by re-solidified Sn. This agglomeration is due to the low solidification temperature of liquid Sn during the cooling process.

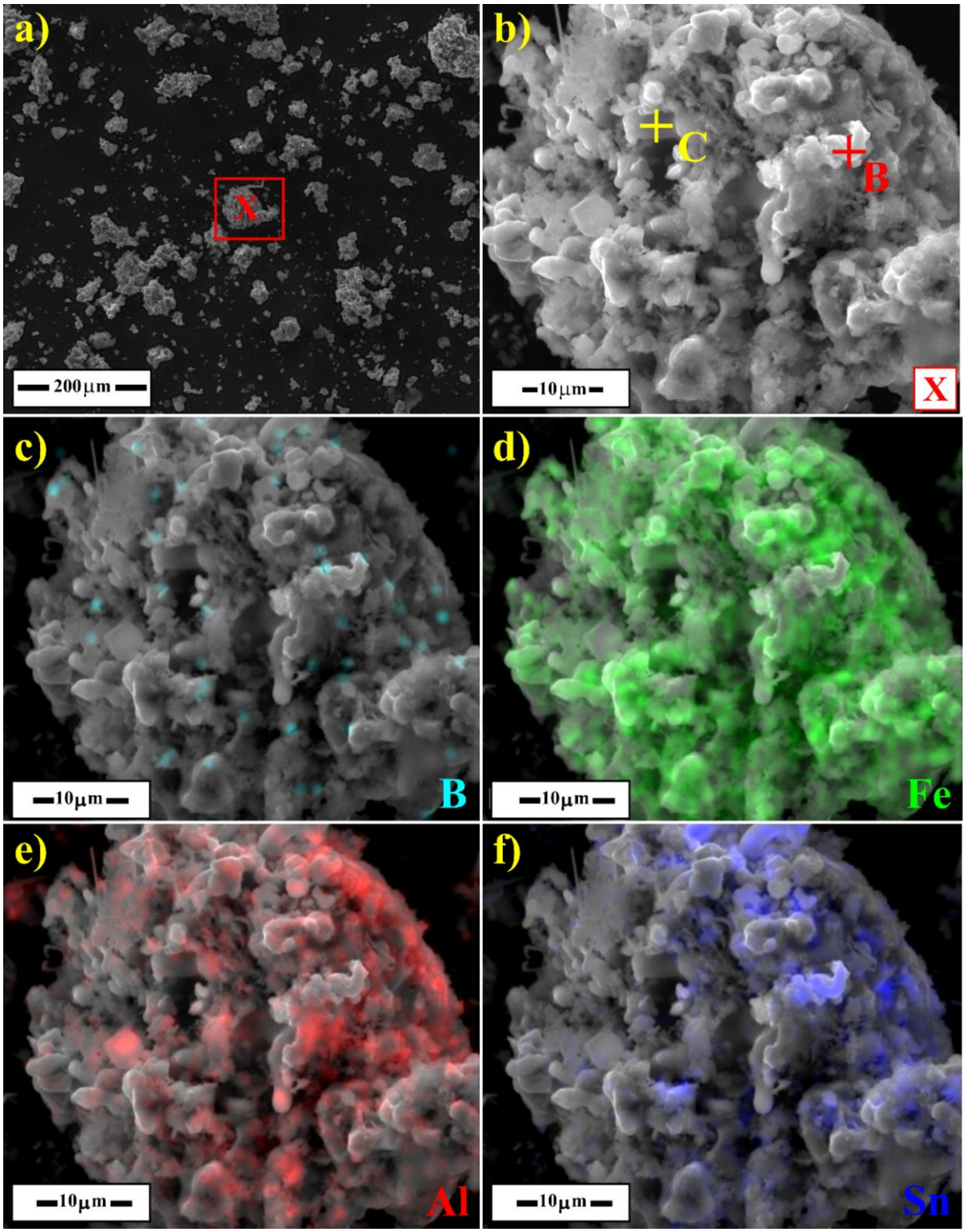


Figure IV. 5: SEM micrographs of synthesized Fe_2AlB_2 with Sn additive at 1000 °C. (b) Higher magnification of inset in (a). SEM-EDS elemental mapping of: (c) boron, (d) iron, (e) aluminum, and (f) tin.

Elemental mapping of non-agglomerated free Fe_2AlB_2 particles synthesized with Sn additive at 1000 °C is shown in Figure IV.6a-6e. The presence of another phase that contains only Al and B was detected, probably Al_xB_y intermetallic (Spot E: Al 62 at. %, B 37 at. %, and Fe 0.6 at. %). This latter did not appear in the XRD diffractogram owing to its small content in the synthesized powder. This phase was not considered in this work and was not reported previously. Thus, more work is needed to show whether this phase plays a role in the reaction mechanism of Fe_2AlB_2 formation.

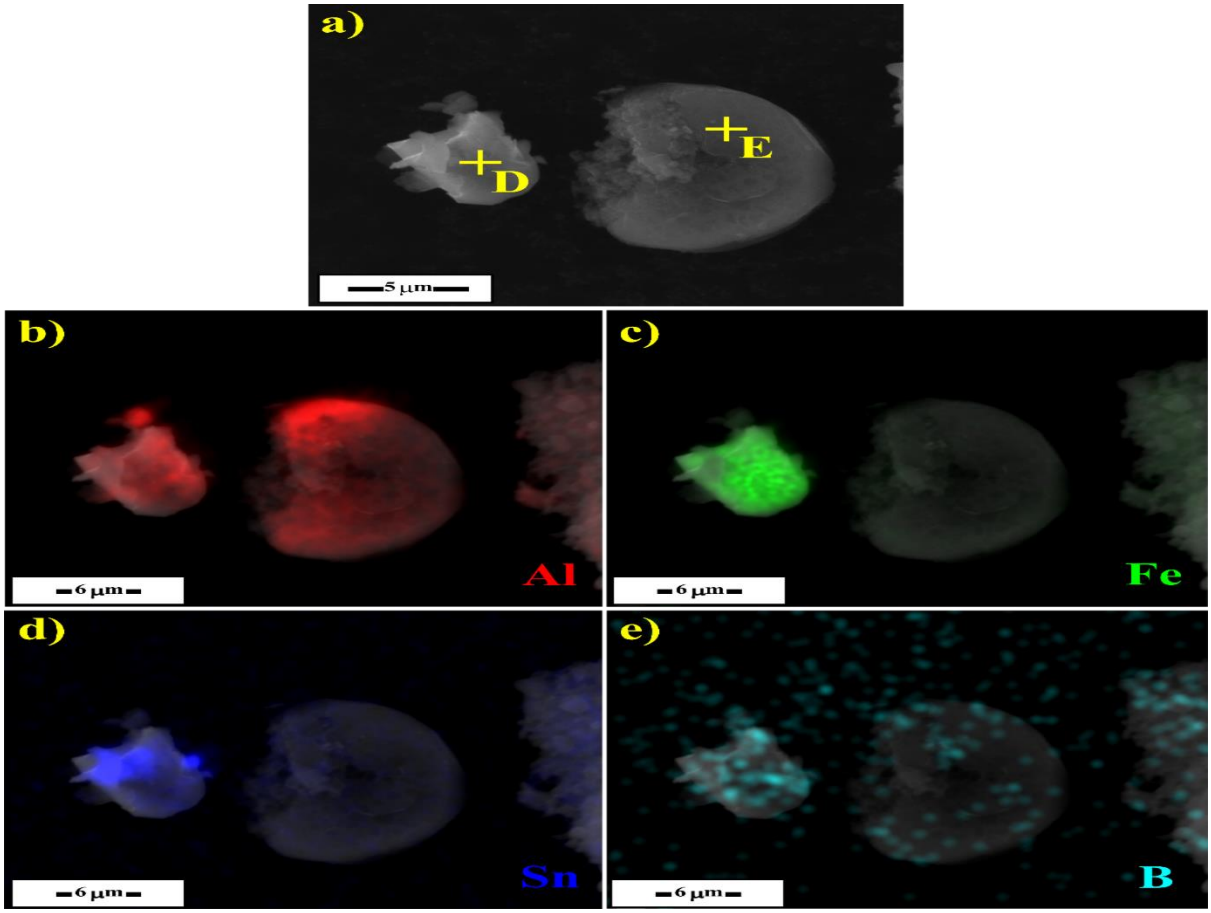


Figure IV. 6 : SEM micrographs of synthesized Fe_2AlB_2 with Sn additive at 1000 °C. SEM-EDS elemental mapping of: (b) aluminum, (c) iron, (d) tin, and (e) boron.

4.1.5 Synthesis of MAX phases

The Figure IV.7a depicts the Cr_2AlC sample taken out of the furnace with KCl salt. The salt appears slightly transparent and remains white in color.

In Figure IV.7b, After the removal of the salt, we observed that the Cr_2AlC with KCl surface sample became transparent. In contrast, when we examined the Cr_2AlC sample with KBr Fig IV.7c salt after taking it out of the furnace, the salt appeared white and transparent. However, once we removed the salt, we noticed a greenish color on the sample's surface Fig IV.7d, which suggests a slight degree of oxidation. As for the sample with NaCl Fig IV.7e, there was a greenish tint due to the presence of the salt, but this color disappeared from the sample's surface upon salt removal Fig IV.7f.

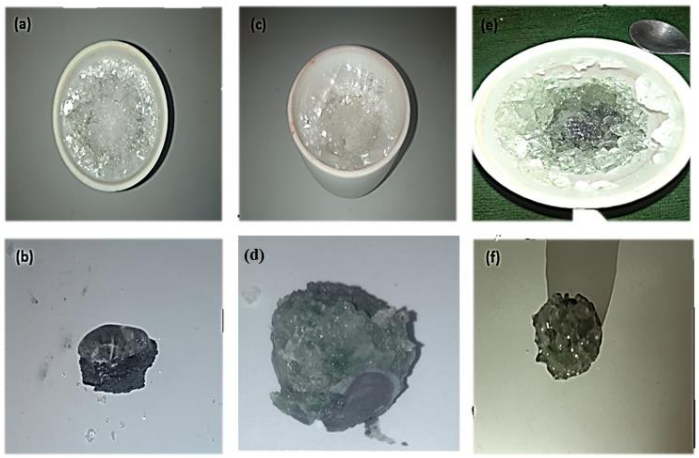


Figure IV. 7*:* Digital photographs showing (a),(c),(e) : sample of Cr_2AlC taken from the oven with KCl ,KBr and NaCl salt respectively ,(b),(d),(f) : the sample of Cr_2AlC after salt removal.

4.1.5.1 Synthesis of Cr_2AlC

To clearly display the effect of salt shielding on the synthesis of MAX phase Cr_2AlC, we have tested four different salts namely KCl, NaCl, KBr and NaBr. We have monitored synthetized samples with XRD.

4.1.6 Characterization of MAX phases with X-Ray Diffraction

4.1.6.1 Synthesis of Cr_2AlC with KCl shielding

Figure IV.8: presents the X-ray diffraction analysis of the synthesized Cr_2AlC at various temperature 900 °C to 1200 °C for 1h with molar ratio of 2Cr/1.2Al/1C. For the synthesized sample at 900 °C using KCl the pattern shows the major phases is Cr_2AlC with some peaks of Cr_2Al and Cr_3C_7. At 1000 °C.

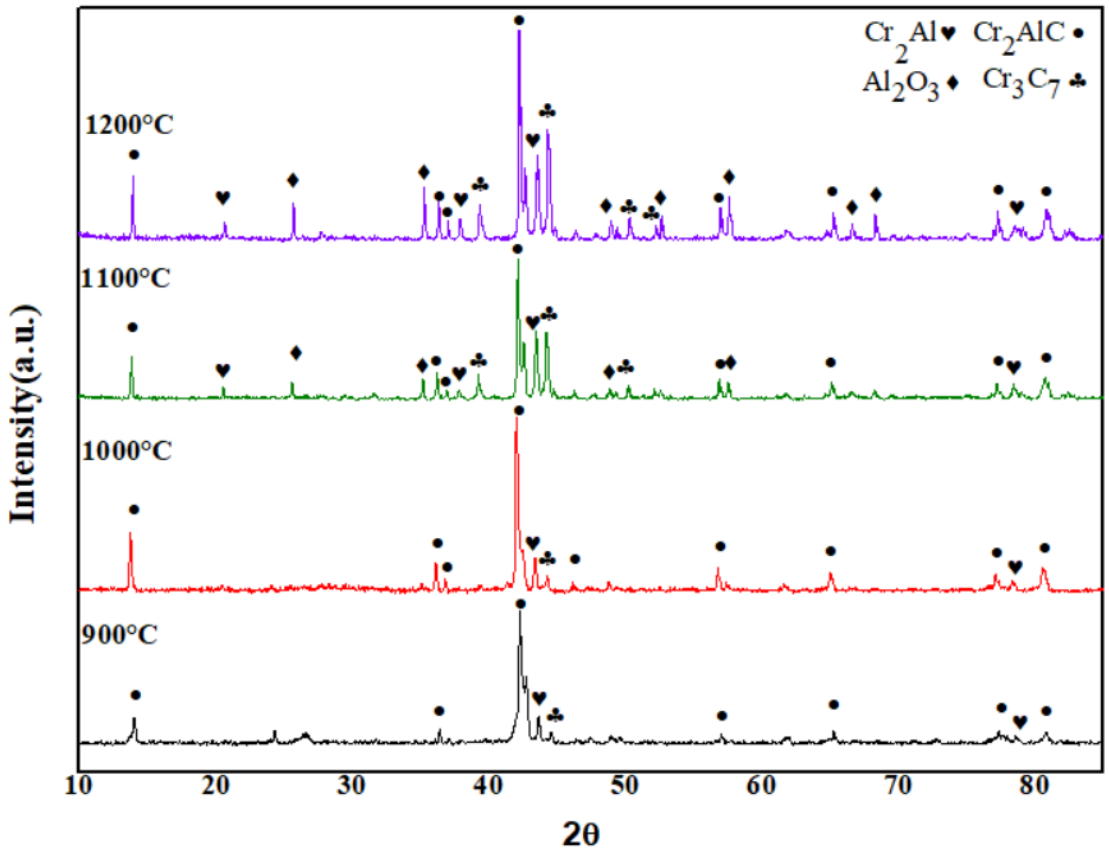


Figure IV. 8: X-ray diffraction analysis of the synthesized Cr_2AlC at various temperature 900 °C to 1200 °C for 1h with molar ratio of 2Cr/1.2Al/1C.

The XRD revealed successful synthesis of single-phase of Cr_2AlC accompanied with small amount of Cr_2Al and Cr_3C_7. With increasing the temperature at 1100°C the peaks intensities of Cr_2Al and Cr_3C_7 increase and some peaks of Al_2O_3 appears with major phase of Cr_2AlC. up to 1200°C Cr_2AlC is still the major phase however peaks intensity of Cr_2Al, Al_2O_3 and Cr_3C_7 increased, this probably means that Cr_2AlC start decomposing.

The above results indicate that nearly single-phase Cr_2AlC samples can be obtained by pressureless sintering of the 1.2Al/2Cr/1C with KCl mixture at 1000 ºC for only 1 h.

4.1.6.2 Synthesis of Cr_2AlC with NaCl shielding

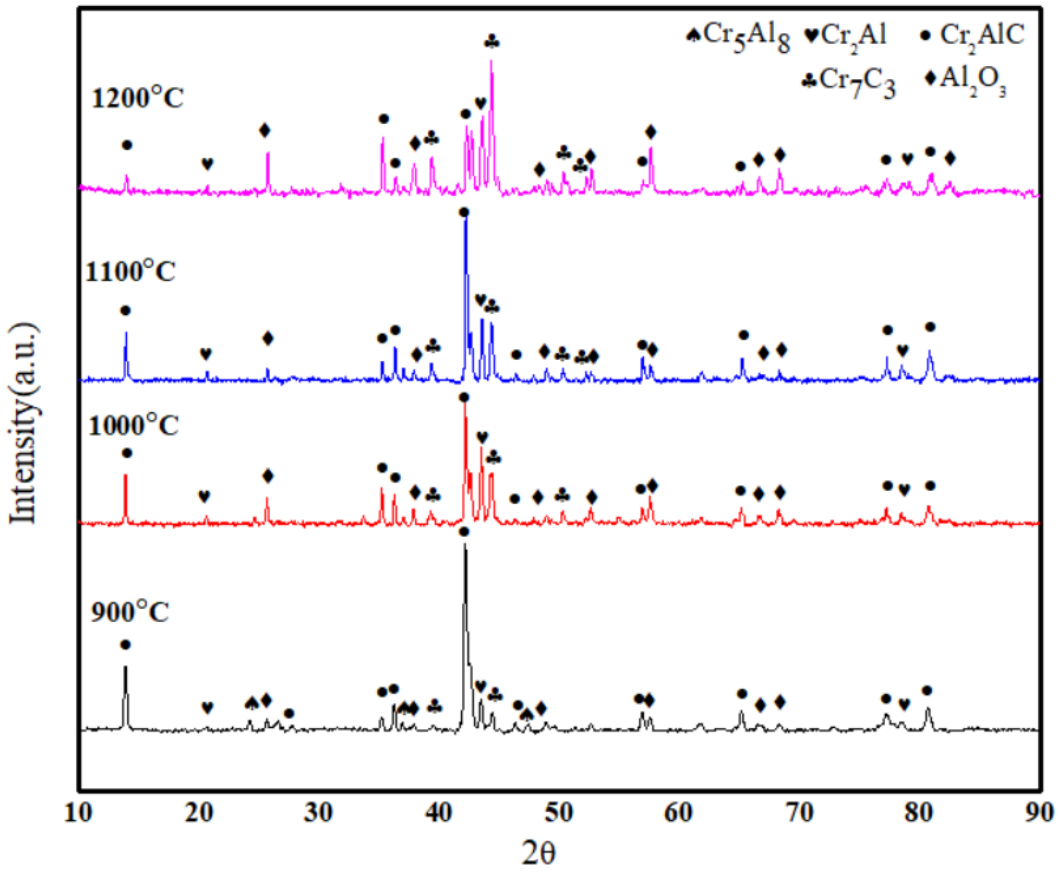


Figure IV. 9 : XRD patterns of 2Cr/Al/C, synthesized by the MS^3 process using NaCl salt at 900, 1000, 1100, and 1200 °C, for 1h synthesis time.

Figure IV. 9: illustrate the XRD patterns of synthesized Cr_2AlC with NaCl molten salt at different temperatures, as we can see at for all temperature the major phase is Cr_2AlC, at 900 the impurities (Cr_5Al_8 , Cr_2Al , Cr_7C_3 and Al_2O_3) exist with a small amount , with the increasing the temperature the intensity of impurities increased .

4.1.6.3 Synthesis of Cr_2AlC with KBr shielding

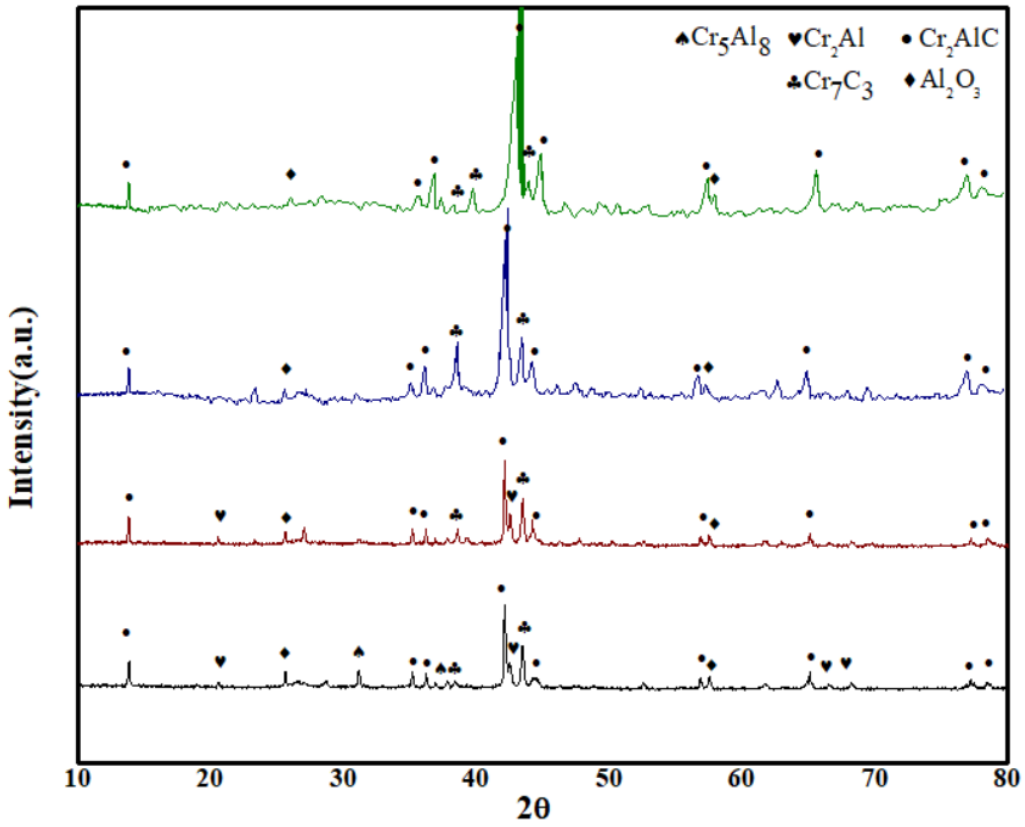


Figure IV. 10 : XRD patterns of 2Cr/Al/C, synthesized by the MS^3 process using KBr salt at 900, 1000, 1100, and 1200 °C, for 1h synthesis time.

Figure IV. 10: shows the XRD patterns of synthesized Cr_2AlC with KBr molten salt at different temperatures 900 to 1200 for 1h as we can see at the temperature 900 Cr_2AlC is the main phase with some peaks of Cr_5Al_8 , Cr_2Al , Cr_7C_3 and Al_2O_3 when racing the temperature we noticed than the peaks of Cr_5Al_8 dispersed , up to 1100 Cr_2Al disappeared and there are some peaks of Cr_7C_3 and Al_2O_3 , at 1200 the intensity of Cr_7C_3 decreased and Cr_2AlC increase which mean the high purity synthesized in the case of KBr salt was at 1200C for 1h .

4.1.6.4 Synthesis of Cr_2AlC with NaBr shielding

Figure IV.11 shows the X-ray diffraction patterns of the samples synthesized by molten salt method at various temperatures in the range of 900-1150°C for 1h with NaBr for the temperature 900°C there are some peaks of Cr_2AlC , Cr_5Al_8,Cr_7C_3,Cr_2Al and Al_2O_3 when increasing the temperature at 1000°C some peaks of Cr_7C_3 and Cr_5Al_8 disappears and Cr_2AlC

appears , up to 1050°C the intensity of Cr_2AlC increase but with some peaks of Al_2O_3 , Cr_2Al and Cr_2C_7 .

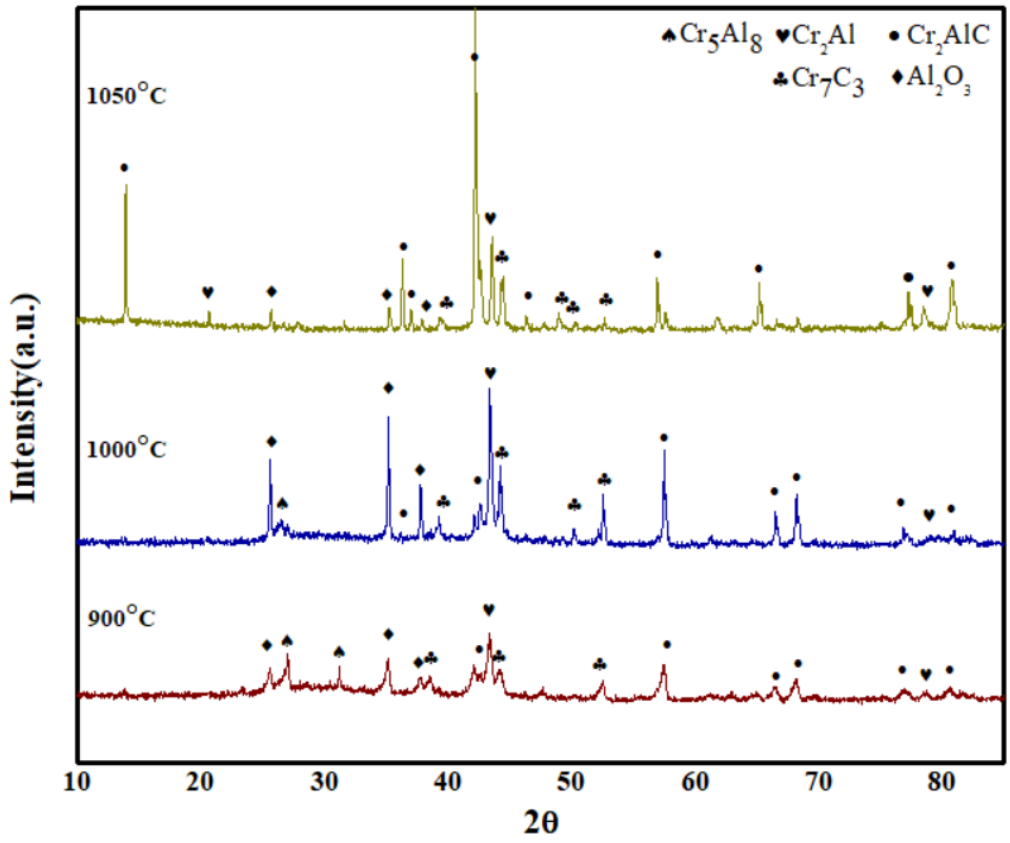


Figure IV. 11: XRD patterns of 2Cr/Al/C, synthesized by the MS[3] process using NaBr salt at 900, 1000, 1100, and 1200 °C, for 1h synthesis time.

Based on the above results it can be concluded that the Cr_2AlC with high purity can be synthesized with molten salt shielded sintering with KCl as salt at 1000°C and with KBr salt at 1200°C for 1h.

For the salts NaCl and NaBr (figure IV.9,11) respectively the main phase was Cr_2AlC at the temperature 1000°C for NaCl and 1050°C for NaBr but with a lot of impurities.

As the temperature rises beyond the optimal temperature for the formation of Cr_2AlC, (1000°C for KCl, 1200°C for KBr and 900°C for NaCl) a notable phenomenon emerges whereby the stability of Cr_2AlC becomes compromised due to an increase in impurities. This phenomenon is linked to the decomposition of Cr_2AlC. Xao et al. [5] conducted the thermal stability of Cr_2AlC. Their research highlighted that as the temperature surpasses a critical threshold, Cr_2AlC undergoes decomposition, resulting in the emergence of two distinct binary

phases: Cr_5Al_8 and $Cr_{23}C_6$.the same thing with Dan et al. [17] where the Cr_2AlC phase was synthesized at 1250°C with high purity; however, upon elevating the temperature to 1300°C, the presence of the impurity phase Cr_7C_3 is increased. This implies that Cr_2AlC initiates decomposition into Cr_7C_3 as the temperature is raised.

From the above result we can conclude that the influence of potassium chloride (KCl) on phase synthesis is multiple, making it the optimal choice among other salts (NaCl, NaBr and KBr) in a reactive medium. It demonstrates superior capabilities in expediting the phase formation process, resulting in a notable reduction in the required formation temperature.

Scanning electron microscopy of MAX phase Figure IV.12 shows SEM micrographs of sample synthesized at 1000°C with KCl salt for 1h, the result reveal that the particle size (Figure IV12.a) is 10-50 µm as shown at higher magnification in Fig IV.12.b where the Cr_2AlC particle present a randomly shaped with size of 4 µm. Tian et al.[16]also find the size of Cr_2AlC synthesized by molten salt assisted method (KCl, NaCl) about 2-8µm.

It has been demonstrated that the molten salt method decreases particle size as the mass ratio of salt to precursor material increases. The particle size of the MAX phase decreases dramatically [245], and this is attributed to the molten salt penetrating between MAX phase grains to prevent their agglomeration and sintering [140].

The elemental mapping conducted on the same area (Fig IV.12c, e) confirms the successful synthesis of Cr_2AlC phase .

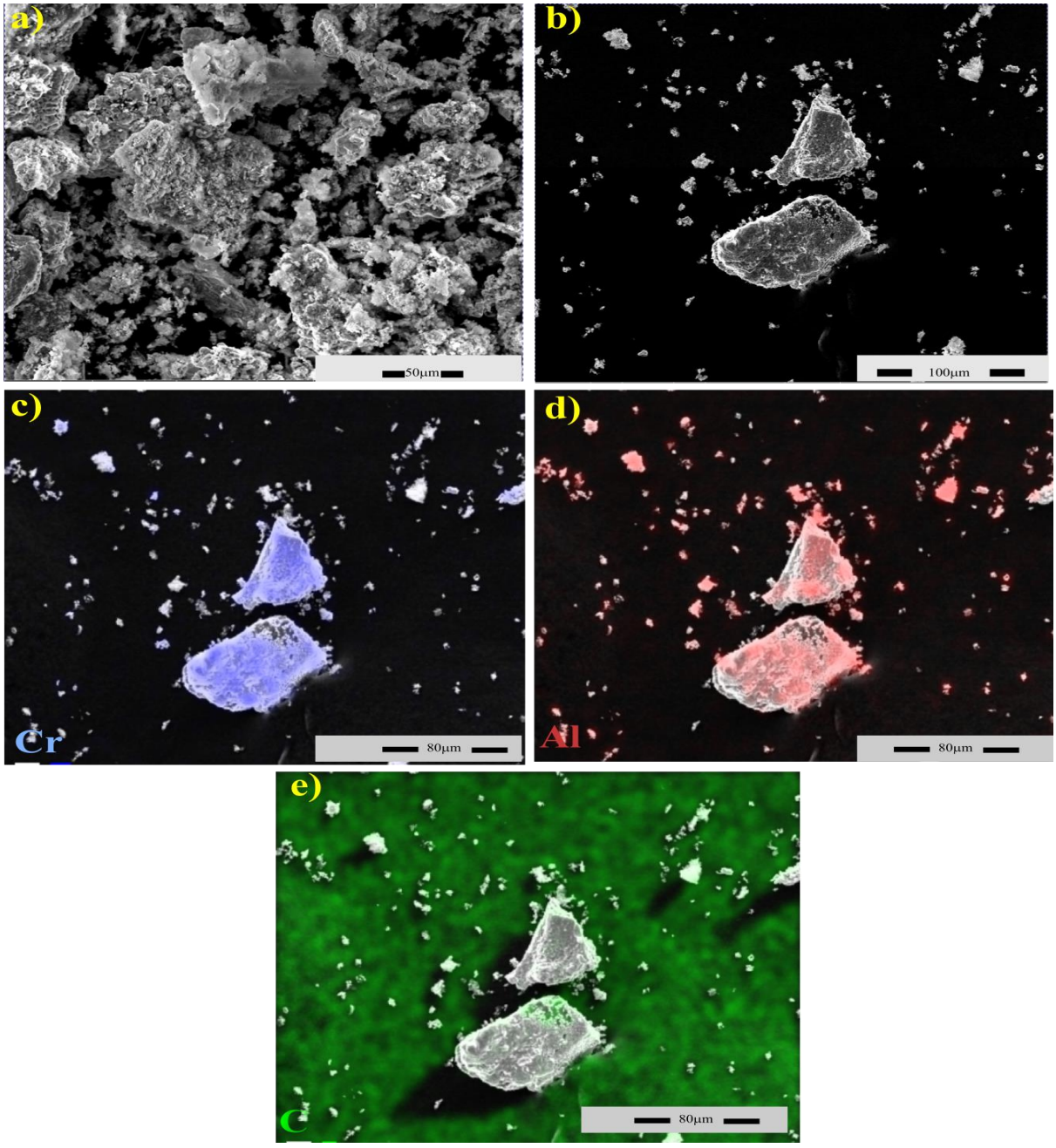


Figure IV. 12: (a) SEM micrographs of synthesized Cr_2AlC with KCl salt at 1000 °C, b) Higher magnification. SEM-EDS elemental mapping of: (c) Chromium, (d) aluminum, and (e) Carbon.

4.2 Synthesis of two-dimensional material MXenes

4.2.1 Synthesis of two-dimensional Cr_2CT_x

The X-ray powder diffraction (XRD) patterns Fig IV.13 reveal the presence of both the precursor MAX phase (Cr_2AlC) and MXene (Cr_2CT_x). In the XRD pattern of Cr_2CT_x, some peaks of Al_2O_3 are observed, which can be attributed to the interaction of etched Al and Cr atoms with -O and -OH bonding in an acidic solution. This interaction leads to the formation of Al_2O_3 and Cr_2CO_2. The replacement of A element by a surface termination after etching is noticeable through a shift in the XRD pattern, indicating exfoliation [164,165].

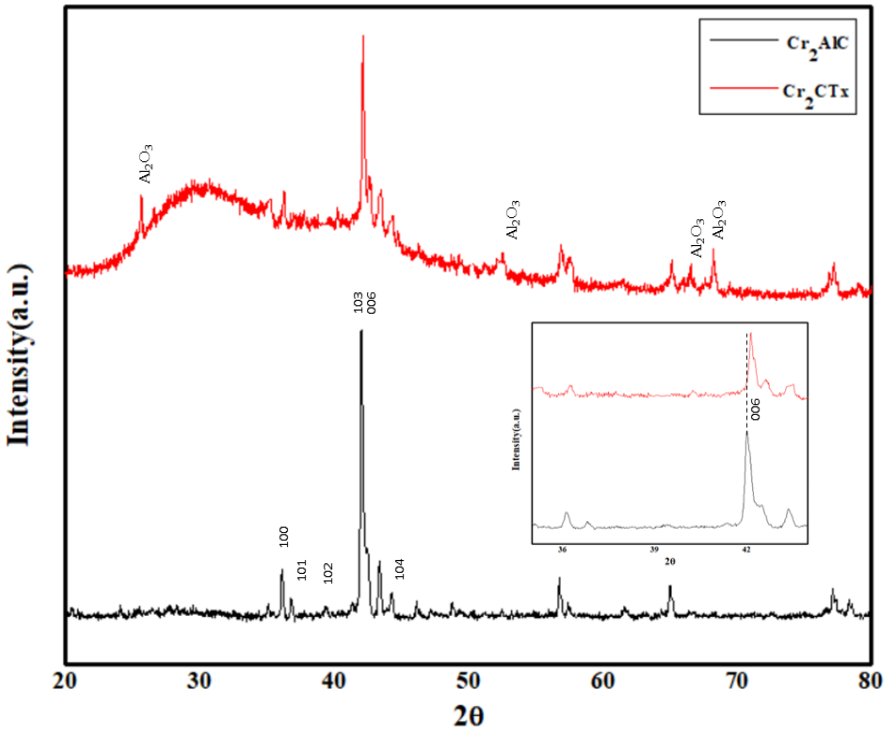


Figure IV. 13 : XRD patterns of the MAX (Cr_2AlC) and its MXene (Cr_2CT_x).

Zooming in on the XRD data, a significant shift is observed in the most intense characteristic diffraction peak at θ=42.26, corresponding to plane 006. These results bear similarities to [165].

4.2.2 Synthesis of two-dimensional $Ti_3C_2T_x$

The Figure IV.14 presents the XRD patterns of MAX phase and MXene. The diagram illustrates the phases of MAX Ti_3AlC_2. In diagram (b) corresponding to the powder after etching $Ti_3C_2T_x$. It can be observed that the crystallinity and structural order of the MAX phase decrease, as evidenced by the broadening and noticeable shift to a smaller value of the characteristic peak (002) at 9.5 in Ti_3AlC_2. This shift is a result of the larger d-spacing caused by the structural expansion during etching and the substitution of Al with end groups such as F and OH/O. The most prominent peak at 2θ = 39° almost disappears, providing stronger evidence for the removal of Al layers from Ti_3AlC_2 [246].

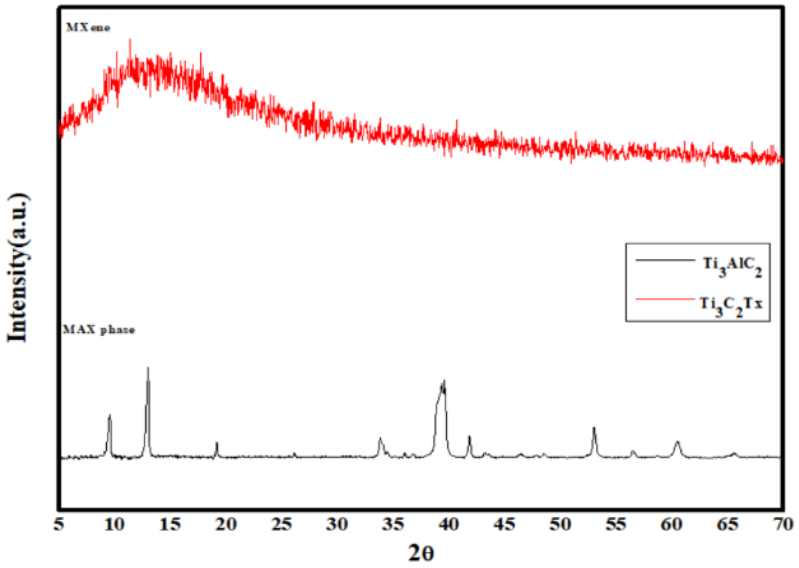


Figure IV. 14 : XRD patterns of the MAX (Ti_3AlC_2) and its MXene ($Ti_3C_2T_x$).

4.3 Adsorption studies

4.3.1 BET Analysis

As shown in Figure 15, the adsorption-desorption isotherms of nitrogen on the prepared solid matrices give relatively low specific surface areas of the order of 12.406 m^2/g for Cr_2CT_x, 48.25 m^2/g for $Ti_3C_2T_x$ and 8.286 m^2/g for Cr_2AlC.

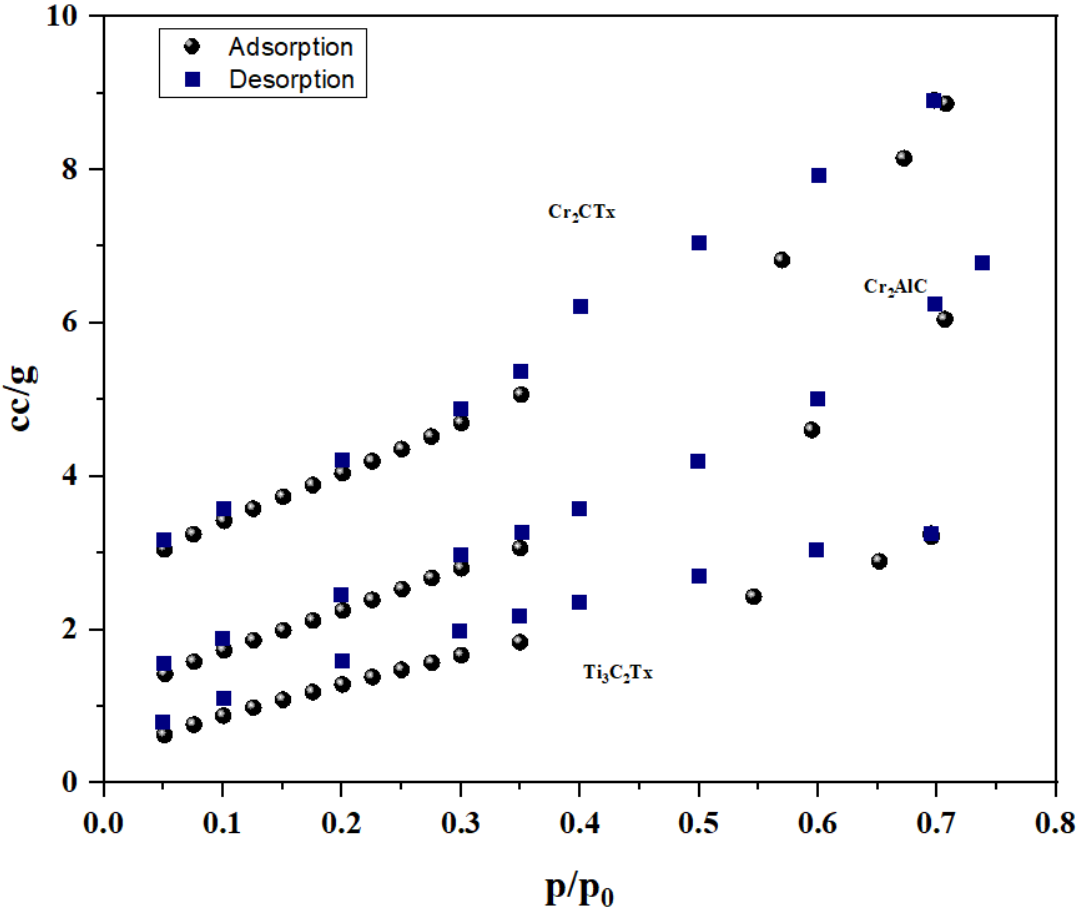


Figure IV. 15 :Nitrogen adsorption–desorption isotherms of Cr_2AlC, Cr_2CT_x and $Ti_3C_2T_x$ samples.

4.3.2 Adsorption of MG in batch mode

In this section, a series of adsorption tests, in discontinuous mode, of malachite green (MG) on each MAX, MAB and MXene phase, was carried out in order to select the most effective phase.

The corresponding conditions are as follows:

- Medium pH: 6
- Oscillation speed: 225
- Temperature: 20 °C
- Contact time: 0 to 24h
- Initial concentration: 10 mg/L
- Mass of adsorbent: 0.01g

The MXenes and MAX, MAB phases are used without any treatments.

4.3.2.1 Effect of contact time

The results of the adsorption kinetics of the different MAX, MAB and MXenes phases are presented in the Figure IV.16.

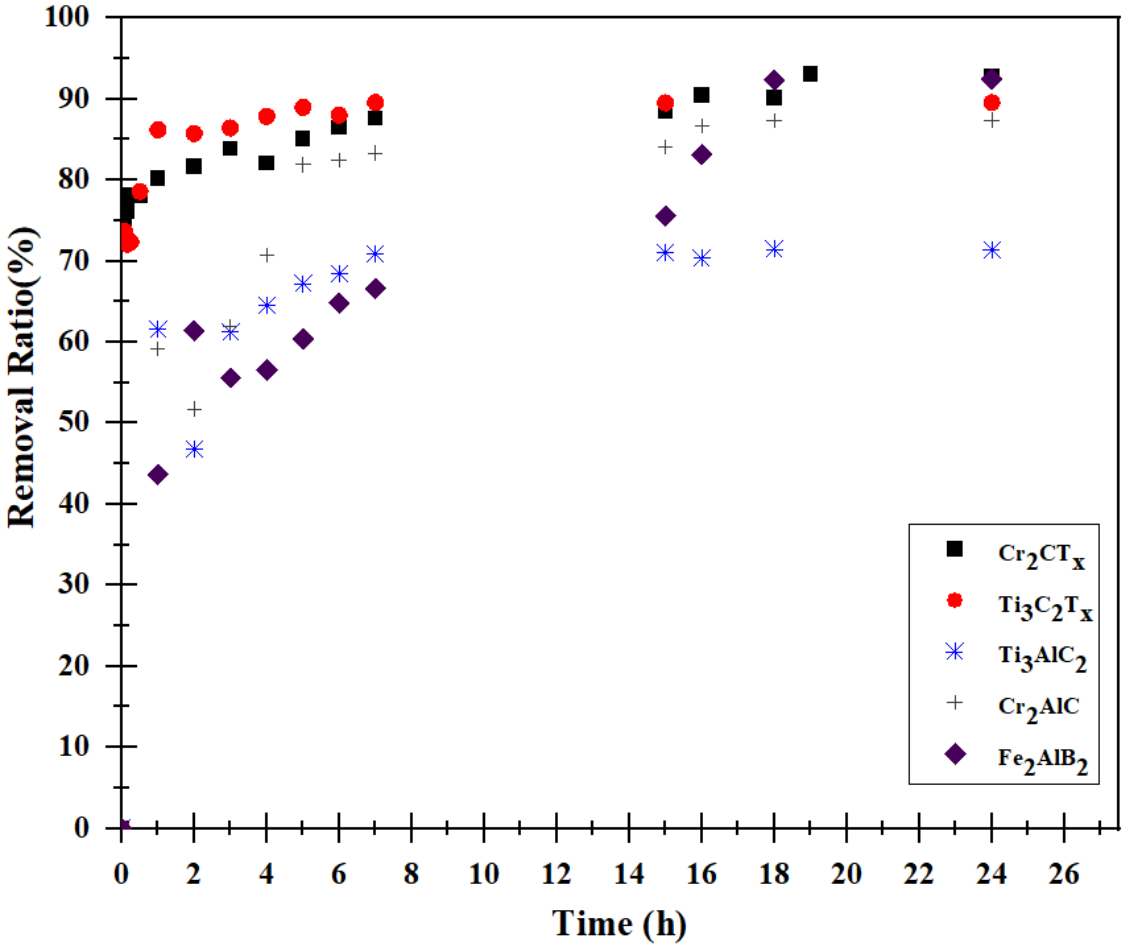


Figure IV. 16 :Kinetics of adsorption of MG on different MAX, MAB and MXenes phases.

These results allow us to draw the following information:

• Initially, the MG removal efficiency increases dramatically for MXenes ($Ti_3C_2T_x$ and Cr_2CTx) unlike the MAB and MAX phases. However, this increasing rate slows down as time increases.

• The kinetics of MG adsorption by MXene "$Ti_3C_2T_x$" is faster compared to the others while the highest elimination rate is obtained by Cr2CT_x. However, Cr_2CT_x is in 2nd position in terms of rapidity.

• Indeed, the Fe_2AlB_2 support is the slowest to eliminate of all the other materials used, however it achieves the highest elimination rate like Cr_2CT_x in 24 hours.

• The removal efficiency reaches 92.99% for Cr_2CT_x, 89.53 for $Ti_3C_2T_x$, 71.44 for Ti_3AlC_2, 87.73 for Cr_2AlC and 92.45 for Fe_2AlB_2.

4.3.2.2 Adsorption kinetics

Adsorption kinetics are very important since they allow us to understand the mechanism and speed of the adsorption process. In this regard, there are different types of models, and each model is hypothesis-driven and aims to understand the adsorption mechanism. Among these models the most commonly used are the Lagergren pseudo-first order model and the pseudo-second order model. The results obtained clearly show that the pseudo-second order model fits best since the correlation coefficients are close to unity.

As shown in Table IV.1, the calculated and experimental Qe values are close to each other. The high correlation coefficients and good agreement of the experimental and calculated Qe values suggest that the adsorption kinetics of MG on the MXene and MAX phases follow the pseudo-second-order model and interact via a chemisorption process. These results are in perfect agreement with those obtained by Kadhom et al. [267] in their study relating to the elimination of MG by $Ti_3C_2T_x$.

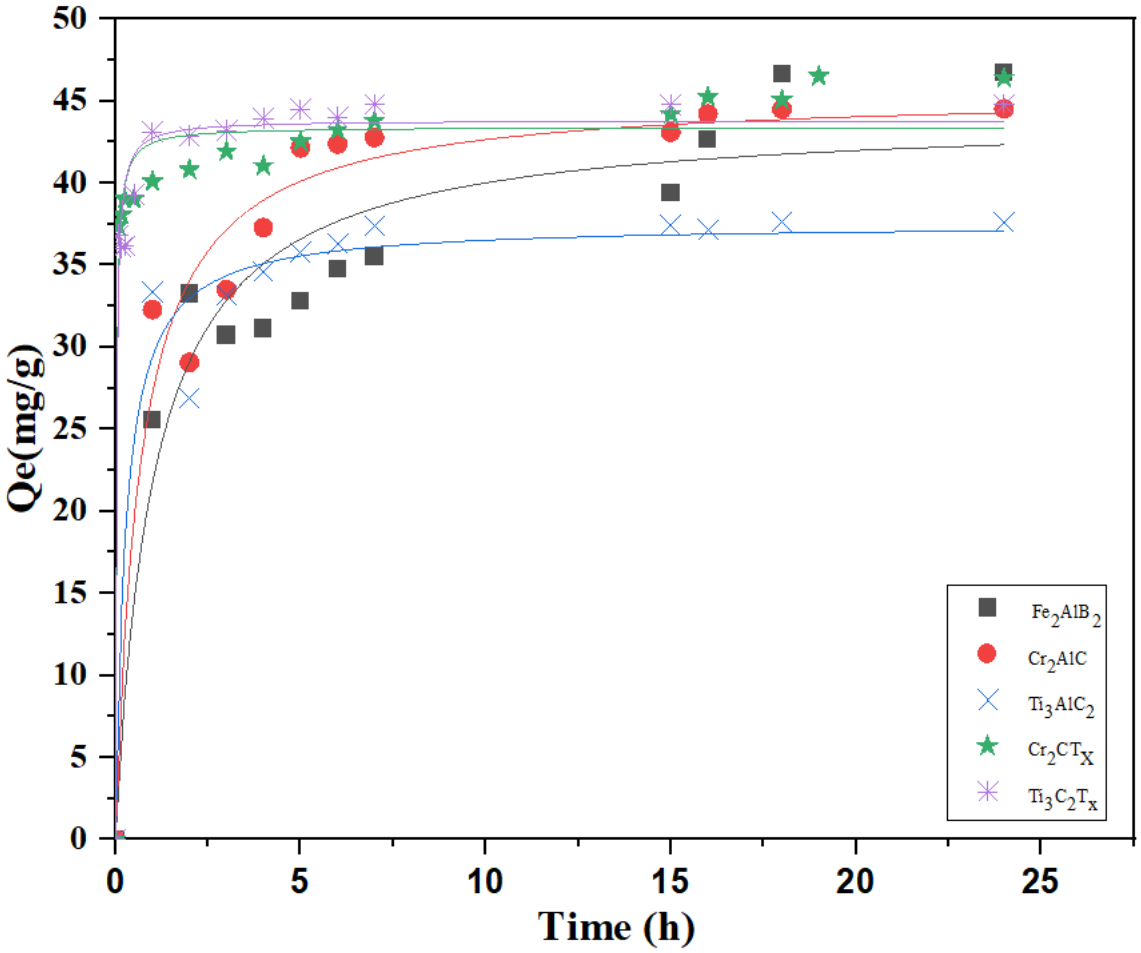


Figure IV. 17: Adsorption Kinetics of MG on MAB, MAX phases and MXenes.

The use of these two kinetic models in the adjustment of the points experiments allowed us to arrive at the following results.

- All materials used followed the pseudo second order model.
- The calculated adsorbed quantities of MG at equilibrium remain very close to the experimental values for all materials.

Table IV. 1: Kinetic parameters for second order model.

Adsorbent	Q_{exp} *(mg.g-1)*	*Qe (mg.g-1)*	K_2 *(min-1)*	R^2_2
Cr_2CT_x	46.49	46.1041	0.1020	0.999
$Ti_3C_2T_x$	44.76	44.83	0.35289	0.999
Ti_3AlC_2	35.72	44.83	0.35289	0.999
Cr_2AlC	43.68	45.0653	0.02898	0.996
Fe_2AlB_2	46.22	49.11	0.0082	0.9782

4.3.2.3 Effect of initial pH of solution

The adsorption process is notably affected by the pH of the solution, playing a crucial role in determining both the surface charge of the adsorbent and its overall state. The influence of pH is particularly pronounced in the adsorption of MG dye due to the existence of two distinct forms of the dye—chromatic and leuco—which are contingent upon the pH level of the solution.

As indicated by Figure IV.18, the effect of the solution pH on the MG adsorption onto MXenes, MAX and MAB phases was investigated at a contact time of 120 min, solution concentration of 10 ppm, and dose amount of 0.01 g. The studied pH range was from 2 to 10.

The point of zero charge (pHpzc) is characterized as the pH of a solution where the overall surface charge of the adsorbent particle becomes neutral. Understanding the pHpzc provides insight into the ionization behavior of functional groups and how they interact with dye solutions [247]. The pHpzc values are about 4.19, 3.6, 6.4, 5.7, 6.9 for Ti_3C_2Tx, Cr_2CTx, Cr_2AlC ,Ti_3AlC_2 and Fe_2AlB_2, respectively. Figure in ANNEXE 2

As observed in these curves, MXenes $Ti_3C_2T_x$ and Cr_2CT_x exhibit similar behavior. They indicate a decrease in the elimination rate since at pH 2, the value is 94%, decreasing to 81.19% at 4.80. Following this, the removal rate starts to rise as the pH increases until it reaches its peak. This result are similar to that obtained by Mohammed Kadhom [248]. In the case of Cr_2AlC and Fe_2AlB_2, as illustrated in the Figure IV.18, the removal rate increases as the pH level rises.

In the Ti_3AlC_2 phase, the elimination rate declines from pH=2 to pH=6 (50%), after which it begins to rise, reaching its maximum value at pH=10.

The results presented in the Figure IV.18 indicate that the increase in adsorption capacity at basic pH depends on both the surface properties of the MAX, MAB phase and MXenes (pHpzc) and those of the MG dye (pKa ~ 10, structure, and cationic form). At a solution pH higher than the pHpzc, the adsorbent surface becomes negatively charged, leading to positive attraction with the cationic dye. This phenomenon accounts for the observed higher value at pH=8.

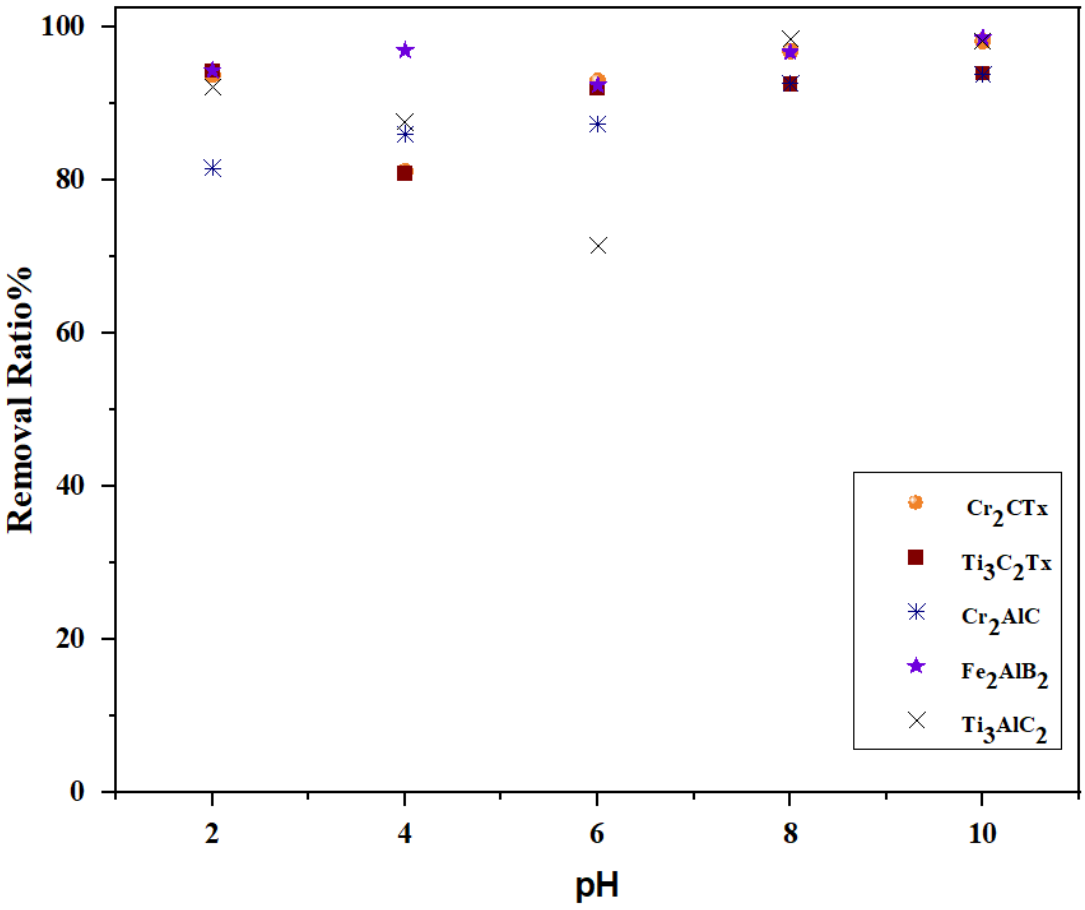


Figure IV. 18: Effect of pH on adsorption of MG onto MXenes, MAX and MAB phases.

4.3.2.4 Effect of adsorbent dose

Adsorbent dose is considered one of the most important parameters in determining the capacity of an adsorbent for a given concentration. The results of the effects of the dose of MXene, MAX and MAB phases (ranged from 0 to 0.1g) at pH=6 as well as the elimination rates of MG. Corresponding results given in Figure IV.19 indicate that the percent adsorption of MG increases with the increasing dose in all used adsorbents and reaches until 99.01 for Cr_2CT_x 91.81% for Cr_2AlC 85%, for Ti_3AlC_2 90.19% and 80.03 % Fe_2AlB_2.

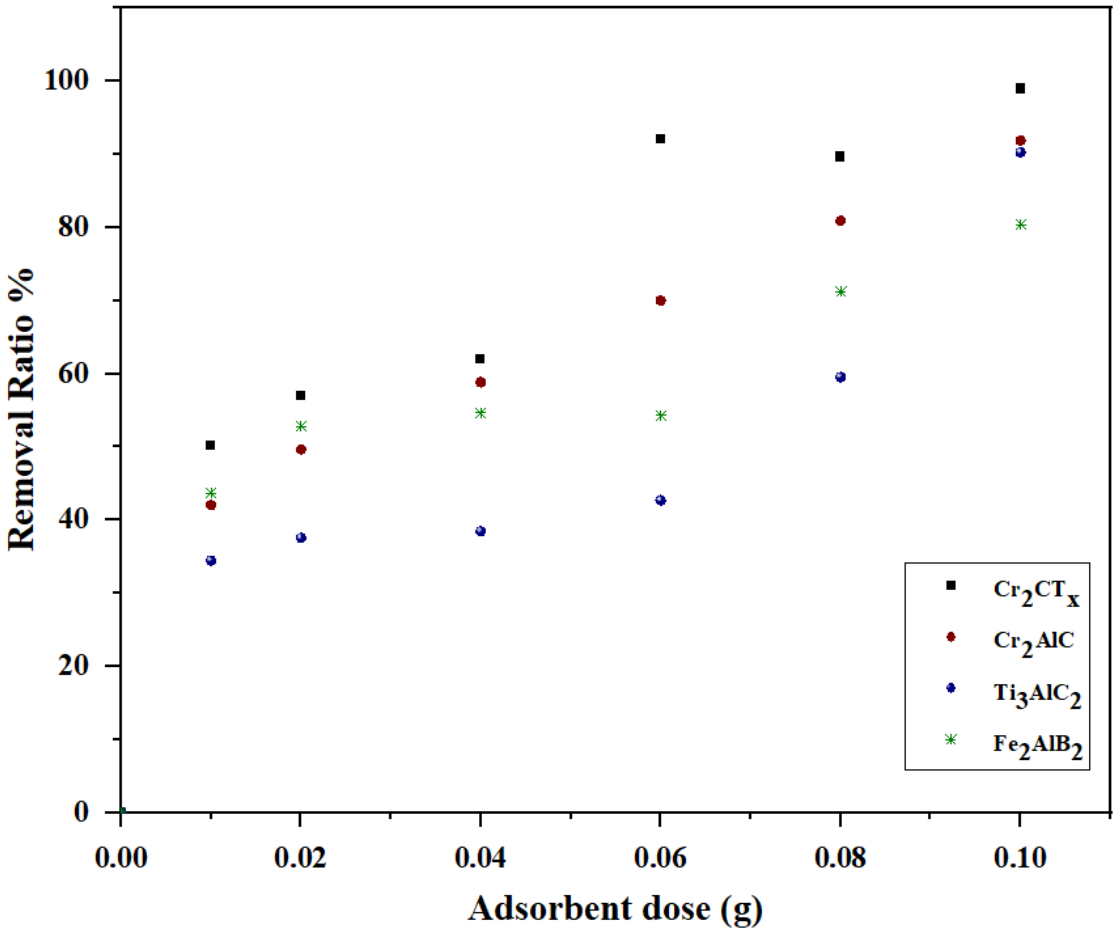


Figure IV. 19 : Effect of adsorbent dose on the adsorption of MG at pH=6.

The increase in adsorption rate with the amount of MXene could be attributed to the abundance of adsorption sites. Indeed, and after etching, the surface of the MXene Cr_2CT_x ends mainly with functional groups of the OH and O type. These groups provide additional adsorption sites for the benefit of the adsorption of new MG molecules on the surface of the

MXene. Similar results are proposed by some authors [267] who obtained a maximum elimination of 93.71% at the experimental conditions used (100 mg; pH = 7, concentration of MG = 5 ppm.

4.3.2.5 Isotherm studies

Isotherm analysis for the adsorption process is an important part of understanding the mechanism occurring between the adsorbent and adsorbate. Langmuir isotherm and Freundlich were used to evaluate the correlation between the adsorption process and the initial concentration of MG. Figures IV.20 present the plots of the equilibrium isotherms of MG adsorption on the different types of MXenes , MAX and MAB phases . The constant values of the corresponding parameters calculated for each isotherm models are listed in Table IV.2. the best fit model that has the highest coefficient of determination (R^2) could clearly explain the adsorption mechanism.

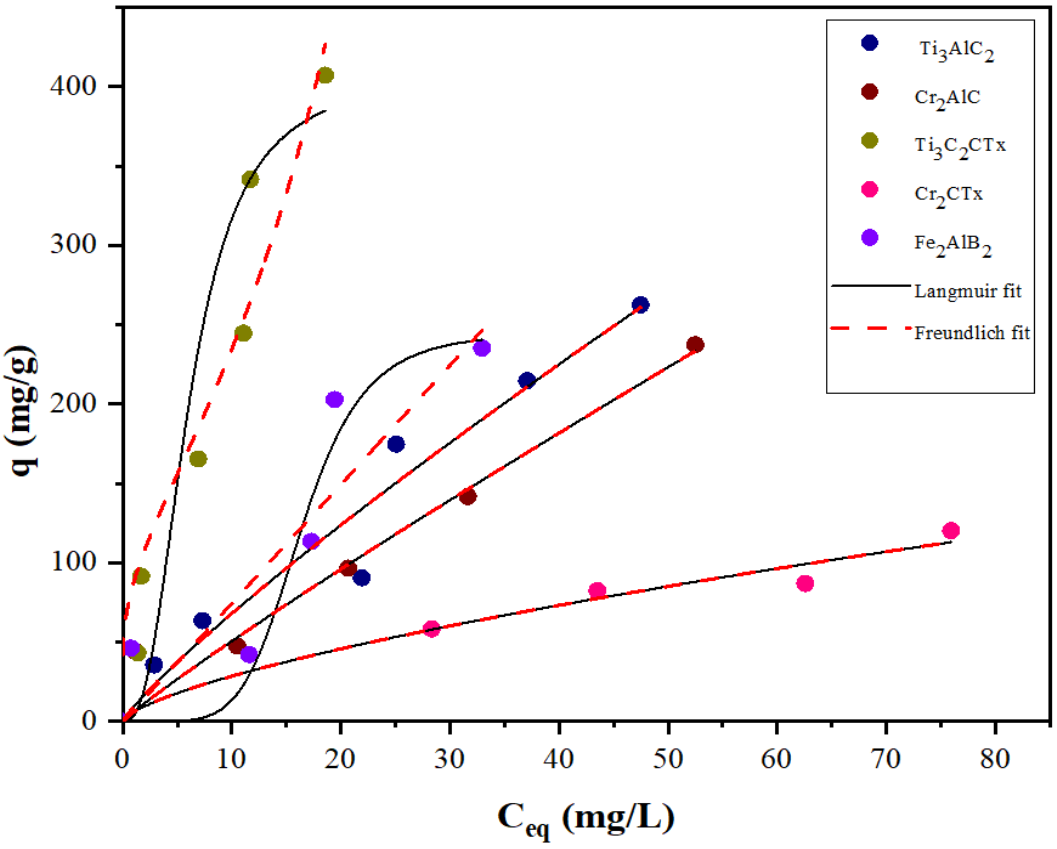


Figure IV. 20 : Adsorption isotherms of MG onto MXene , MAB and MAX phases.

For the isotherm adsorption studies , the highest coefficient of determination R^2 is found in the Freundlich model for all material and this mean that the material has active site with different surface energy it admits formation of multimolecular layer and we have $n > 1$ for all material except for Fe_2AlB_2 which mean that the adsorption is weak , and for the MAB (Fe_2AlB_2) phase the n was between $0.5 > n > 1$ which mean that the adsorption is moderate .

Table IV. 2: Adsorption Isotherm parameters for MG Adsorption onto MXenes, MAX and MAB phases.

Model		***Cr_2AlC***	***Ti_3AlC_2***	***Fe_2AlB_2***	***Cr_2CT_x***	***$Ti_3C_2T_x$***
Freundlich	**R^2**	0.98335	0.915	0.953	0.9629	0.932
	K_f **(mg^{-} $^{1/n}.l^{1/n}.g^{-1}$)**	3.24804	9.37536	2.01224	6.014	42.39
	n	1.07628	1.16068	0.73701	1.475	1.28944
Langmuir	**R^2**	0.98085	0.9097	0.925	0.9588	0.927
	q_m	3296.95	1748.58	4.744	289.81	1277.95
	K_L (mg^{-} $^{1/n}.l^{1/n}.g$-1)	7.7025	0.00373	1.4161	0.0094	0.025

4.4 Summary

This chapter deals with the synthesis of new MAX and MAB phases, as well as the synthesis of the derivative of the MAX phases, MXenes. It also covers the applications of these new materials in the adsorption of malachite green. The results obtained made it possible to propose the following conclusions:

• High purity Fe_2AlB_2 ternary powder is successfully synthesized using 2Fe/2Al/2B mixture with Sn additive at 1000 °C. Above this temperature, the Fe_2AlB_2 phase decomposes into Fe_xAl_y intermetallic and iron borides.

• The sample synthesized at 1200 °C without addition of Sn also shows the production of the Fe_2AlB_2 phase but with a considerable amount of impurities

• Sn metal reduces the formation temperature of intermediate phases like FeB and FexAly and promotes the formation of Fe_2AlB_2 phase with higher purity.

• The mechanism of formation of the compound Fe_2AlB_2 begins with the reaction between Al and Fe to form $FeAl_6$. At a higher temperature, the remaining iron reacts with B to form FeB. The two phases react with each other, forming the Fe_2AlB_2 phase.

• Synthesis of Cr_2AlC using different salts indicates that KCl salt is the best temperature and time reducer and minimizes impurities.

• X-ray diffraction (XRD) analysis of MXenes confirms the formation of this material.

- The applications of these MAX, MAB and MXene phases in the adsorption of malachite green were evaluated by establishing adsorption kinetics and isotherms.

General Conclusions

The main objective of this study is to synthesize new MAB (Fe_2AlB_2) and MAX (Cr_2AlC) phases by the molten salt method, with the aim of reducing the synthesis temperature and obtaining phases free of impurities. To achieve this, investigations were conducted to analyze the effect of adding tin (Sn) additive in the synthesis of the Fe_2AlB_2 phase, as well as the impact of the choice of molten salt in the synthesis of the Cr_2AlC phase. The obtained results revealed significant conclusions.

Regarding the Fe_2AlB_2 phase, the inclusion of tin proved to be a crucial factor in the synthesis process. The addition of tin significantly lowered the required synthesis temperature to as low as 1000 °C, with a holding time of one hour. This temperature and holding duration are among the lowest reported so far. In contrast, samples without tin required a temperature of 1200 °C to observe phase formation.

Concerning the Cr_2AlC phase, results showed that KCl molten salt emerged as the optimal choice compared to alternatives like NaCl, KBr, and NaBr. Synthesis of the Cr_2AlC phase was achieved at 1000 °C using KCl for one hour, and at 1200 °C using KBr. In contrast, NaBr and NaCl salts led to phase formation with a notable level of impurities.

A subsequent step was to remove element A from the MAX phases by a chemical etching to produce two-dimensional MXenes materials ($Ti_3C_2T_x$ and Cr_2CT_X). The diffractograms obtained by X-ray diffraction (XRD) confirmed the successful synthesis of MXenes. These MAX/MAB and MXenes were then evaluated for their adsorption capacity towards malachite green adsorption capacity, with the aim of comparing their adsorption performance. Results indicated that the $Ti_3C_2T_x$-type MXenes is the most efficient in terms of adsorption speed.

Based on the adsorption kinetic results, all MAX, MAB, and MXenes phases followed the pseudo-second-order model. As for adsorption isotherms, all MAX, MAB, and MXenes phases better fit the Freundlich model.

In summary, this study successfully synthesized the MAB and MAX phases using the molten salt method, leveraging the positive effects of tin addition and prudent choice of molten salt. Additionally, the conversion to MXenes was achieved successfully, demonstrating their effectiveness in malachite adsorption. The kinetic and adsorption models provided valuable insights into the underlying mechanisms of the studied processes.

Perspective

Looking ahead, it would be prudent to explore the synthesis of MAX and MAB phases using the molten salt-protected synthesis method. The introduction of a binary system composed of NaCl and KCl offers the potential to significantly reduce both the synthesis temperature and duration, ultimately promoting a more energy-efficient and sustainable production process.

Furthermore, there is ample room for investigation into various MAX, MXenes, and MAB phases regarding their effectiveness in adsorbing substances like malachite green or other dyes. Concurrently, the synthesis of MBene, a class of two-dimensional materials achieved by eliminating element A from the Fe_2AlB_2 phase, can be explored and subsequently applied to the adsorption of pollutants. These multifaceted research avenues hold substantial promise for advancing our understanding of advanced materials and their applications in the realm in water depollution.

Acronyms list

KBs : Kink bands

SOMT : Spin-Orbit magnetic moment transfer

MS^3 : Molten salt shielded sintering

MS : molten salt assisted method

US : Under ultrasound

OTC : Oxytetracyline antibiotic

DMSO : Dimethyl sulfoxide

ML : multilayer

FL : few layer

PVA : Polyvinyl Alcohol

PAM : Polycrylamide

UHMWPE : Ultrahigh Molecular Weight Polythylene

PDOS : Projected density of states

SIBs : Sodium-ion Batterie

EMI SE : Interference Shielding Effectiveness

PVDF : Hydrophilic Polyvinyliden difluride

PES : Poluythersulfone

PAN : Polyacylonitrile

MOFs : Frameworks

DOS : Density of States

RhB : Rhodamine B

MG : Malachite Green

BET : Brunauer-Emmett-Teller

XRD : X-ray Diffraction

TGA : Thermogravimetric

DTA : Differential Thermal Analysis

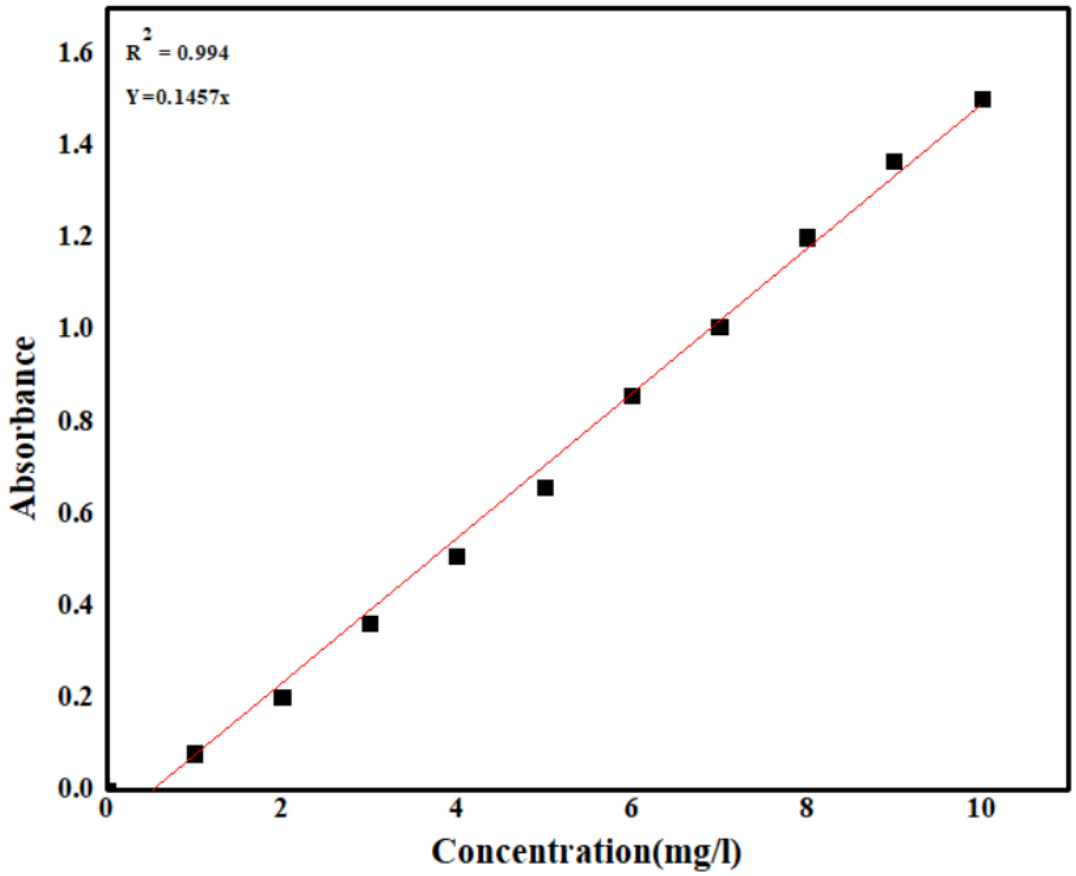
SEM : Scanning Electron Microscope

MB : Methylene Bleu

MG : malachite green

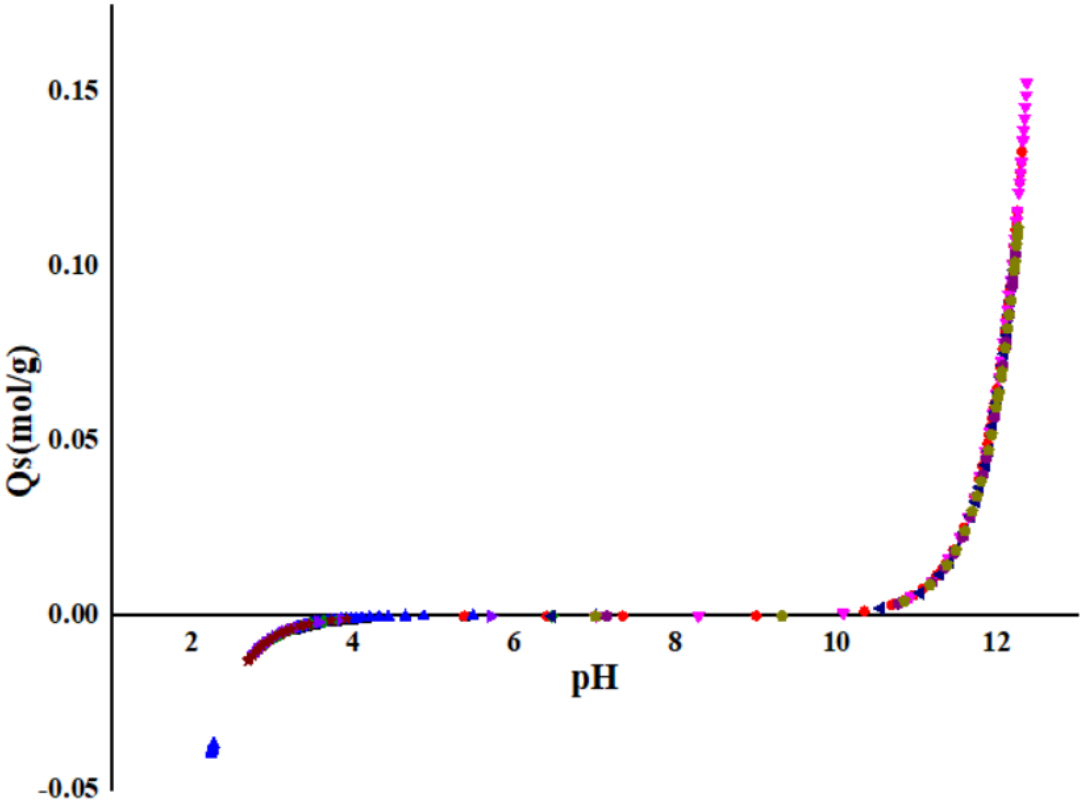
ANNEX 1

Figure 1: Calibration curve of the malachite green used.



ANNEX 2

Figure2: Potentiometric curves of the MAX, MAB and MXenes phases.



References

[1] W. Jeitschko, H. Nowotny, F. Benesovsky, Carbides of formula T2MC, Journal of the Less Common Metals 7 (1964) 133–138. https://doi.org/https://doi.org/10.1016/0022-5088(64)90055-4.

[2] M.W. Barsoum, T. El-Raghy, Synthesis and characterization of a remarkable ceramic: Ti3SiC2, J. Am. Ceram. Soc. 79 (1996) 1953.

[3] T. El-Raghy, A. Zavaliangos, M.W. Barsoum, S.R. Kalidindi, Damage Mechanisms around Hardness Indentations in Ti3SiC2, Journal of the American Ceramic Society 80 (1997) 513–516. https://doi.org/10.1111/j.1151-2916.1997.tb02861.x.

[4] M.W. Barsoum, MAX phases: properties of machinable ternary carbides and nitrides, (2013).

[5] L.-O. Xiao, S.-B. Li, G. Song, W.G. Sloof, Synthesis and thermal stability of Cr2AlC, J Eur Ceram Soc 31 (2011) 1497–1502. https://doi.org/https://doi.org/10.1016/j.jeurceramsoc.2011.01.009.

[6] B. Shalini Reghunath, D. Davis, K.R. Sunaja Devi, Synthesis and characterization of Cr2AlC MAX phase for photocatalytic applications, Chemosphere 283 (2021) 131281. https://doi.org/https://doi.org/10.1016/j.chemosphere.2021.131281.

[7] X. Li, S. Wang, G. Wu, D. Zhou, J. Pu, M. Yu, Q. Wang, Q. Sun, Oxidation and hot corrosion behaviors of MAX-phase Ti3SiC2, Ti2AlC, Cr2AlC, Ceram Int 48 (2022) 26618–26628. https://doi.org/https://doi.org/10.1016/j.ceramint.2022.05.356.

[8] Z. Wang, G. Ma, L. Liu, L. Wang, P. Ke, Q. Xue, A. Wang, High-performance Cr2AlC MAX phase coatings: Oxidation mechanisms in the 900–1100°C temperature range, Corros Sci 167 (2020) 108492. https://doi.org/https://doi.org/10.1016/j.corsci.2020.108492.

[9] M. Ade, H. Hillebrecht, Ternary Borides Cr2AlB2, Cr3AlB4, and Cr4AlB6: The First Members of the Series (CrB2)nCrAl with n = 1, 2, 3 and a Unifying Concept for Ternary Borides as MAB-Phases, Inorg Chem 54 (2015) 6122–6135. https://doi.org/10.1021/acs.inorgchem.5b00049.

[10] S. Kota, M. Sokol, M.W. Barsoum, A progress report on the MAB phases: atomically laminated, ternary transition metal borides, International Materials Reviews 65 (2020) 226–255. https://doi.org/10.1080/09506608.2019.1637090.

[11] J. Liu, S. Li, B. Yao, J. Zhang, X. Lu, Y. Zhou, Thermal stability and thermal shock resistance of Fe2AlB2, Ceram Int 44 (2018) 16035–16039. https://doi.org/https://doi.org/10.1016/j.ceramint.2018.06.042.

[12] J. Liu, S. Li, B. Yao, S. Hu, J. Zhang, W. Yu, Y. Zhou, Rapid synthesis and characterization of a nanolaminated Fe2AlB2 compound, J Alloys Compd 766 (2018) 488–497. https://doi.org/https://doi.org/10.1016/j.jallcom.2018.06.352.

[13] Y. Bai, D. Sun, N. Li, F. Kong, X. Qi, X. He, R. Wang, Y. Zheng, High-temperature mechanical properties and thermal shock behavior of ternary-layered MAB phases Fe2AlB2, Int J Refract Metals Hard Mater 80 (2019) 151–160. https://doi.org/https://doi.org/10.1016/j.ijrmhm.2019.01.010.

[14] S. Kota, E. Zapata-Solvas, A. Ly, J. Lu, O. Elkassabany, A. Huon, W.E. Lee, L. Hultman, S.J. May, M.W. Barsoum, Synthesis and Characterization of an Alumina Forming Nanolaminated Boride: MoAlB, Sci Rep 6 (2016) 26475. https://doi.org/10.1038/srep26475.

[15] M. Dey, S. Javaid, D. Clifford, V. Sharma, R. Barua, S. Gupta, Synthesis of nanolayered ternary borides powders (MAB phases) by sustainable molten salt shielded synthesis/sintering (MS3) process, J Mater Sci 57 (2022) 2436–2454. https://doi.org/10.1007/s10853-021-06779-0.

[16] W.-B. Tian, P.-L. Wang, Y.-M. Kan, G.-J. Zhang, Cr2AlC powders prepared by molten salt method, J Alloys Compd 461 (2008) L5–L10. https://doi.org/https://doi.org/10.1016/j.jallcom.2007.06.094.

[17] J.Z.F.W. and Y.T. Dan Xiao, Synthesis of Nano Sized Cr2AlC Powders by Molten Salt Method, J Nanosci Nanotechnol 15, 7341–7345, 2015 (n.d.).

[18] A. Dash, R. Vaßen, O. Guillon, J. Gonzalez-Julian, Molten salt shielded synthesis of oxidation prone materials in air, Nat Mater 18 (2019) 465–470. https://doi.org/10.1038/s41563-019-0328-1.

[19] M. Naguib, M. Kurtoglu, V. Presser, J. Lu, J. Niu, M. Heon, L. Hultman, Y. Gogotsi, M.W. Barsoum, Two-Dimensional Nanocrystals Produced by Exfoliation of Ti3AlC2, Advanced Materials 23 (2011) 4248–4253. https://doi.org/10.1002/adma.201102306.

[20] J. Nan, X. Guo, J. Xiao, X. Li, W. Chen, W. Wu, H. Liu, Y. Wang, M. Wu, G. Wang, Nanoengineering of 2D MXene-Based Materials for Energy Storage Applications, Small 17 (2021) 1902085. https://doi.org/https://doi.org/10.1002/smll.201902085.

[21] X. Zhan, C. Si, J. Zhou, Z. Sun, MXene and MXene-based composites: Synthesis, properties and environment-related applications, Nanoscale Horiz 5 (2020) 235–258. https://doi.org/10.1039/c9nh00571d.

[22] Y.A.J. Al-Hamadani, B.-M. Jun, M. Yoon, N. Taheri-Qazvini, S.A. Snyder, M. Jang, J. Heo, Y. Yoon, Applications of MXene-based membranes in water purification: A review, Chemosphere 254 (2020) 126821. https://doi.org/https://doi.org/10.1016/j.chemosphere.2020.126821.

[23] M.W. Barsoum, MAX phases: properties of Machinable ternary carbides and nitrides. 1st ed, 2013.

[24] Q. Zhang, Y. Zhou, X. San, D. Wan, Y. Bao, Q. Feng, S. Grasso, C. Hu, Thermal explosion synthesis of first Te-containing layered ternary Hf2TeB MAX phase, J Eur Ceram Soc 43 (2023) 173–176. https://doi.org/https://doi.org/10.1016/j.jeurceramsoc.2022.09.051.

[25] M.M. Ali, M.A. Hadi, I. Ahmed, A.F.M.Y. Haider, A.K.M.A. Islam, Physical properties of a novel boron-based ternary compound Ti2InB2, Mater Today Commun 25 (2020) 101600. https://doi.org/https://doi.org/10.1016/j.mtcomm.2020.101600.

[26] S. Kota, E. Zapata-Solvas, A. Ly, J. Lu, O. Elkassabany, A. Huon, W.E. Lee, L. Hultman, S.J. May, M.W. Barsoum, Synthesis and Characterization of an Alumina Forming Nanolaminated Boride: MoAlB, Sci Rep 6 (2016) 26475. https://doi.org/10.1038/srep26475.

[27] S. Kota, M. Sokol, M.W. Barsoum, A progress report on the MAB phases: atomically laminated, ternary transition metal borides, International Materials Reviews 65 (2020) 226–255. https://doi.org/10.1080/09506608.2019.1637090.

[28] W. Jeitschko, H. Nowotny, Die Kristallstruktur von Ti3SiC2—ein neuer Komplexcarbid-Typ, Monatshefte Für Chemie - Chemical Monthly 98 (1967) 329–337. https://doi.org/10.1007/BF00899949.

[29] W. Jeitschko, Die Kristallstruktur von MoAlB, Monatshefte Für Chemie Und Verwandte Teile Anderer Wissenschaften 97 (1966) 1472–1476. https://doi.org/10.1007/BF00902599.

[30] J. Lis, R. Pampuch, J. Piekarczyk, L. Stobierski, New ceramics based on Ti3SiC2, Ceram Int 19 (1993) 219–222. https://doi.org/https://doi.org/10.1016/0272-8842(93)90052-S.

[31] M.W. Barsoum, T. El-Raghy, Synthesis and Characterization of a Remarkable Ceramic: Ti3SiC2, Journal of the American Ceramic Society 79 (1996) 1953–1956. https://doi.org/https://doi.org/10.1111/j.1151-2916.1996.tb08018.x.

[32] M.W. Barsoum, T. El-Raghy, L.U.J.T. Ogbuji, Oxidation Of Ti3SiC2 in Air, J Electrochem Soc 144 (1997) 2508. https://doi.org/10.1149/1.1837846.

[33] T. El-Raghy, A. Zavaliangos, M.W. Barsoum, S.R. Kalidindi, Damage Mechanisms around Hardness Indentations in Ti3SiC2, Journal of the American Ceramic Society 80 (1997) 513–516. https://doi.org/https://doi.org/10.1111/j.1151-2916.1997.tb02861.x.

[34] S.A. Thomas, J. Cherusseri, Recent advances in synthesis and properties of zirconium-based MXenes for application in rechargeable batteries, Energy Storage n/a (2023) e475. https://doi.org/https://doi.org/10.1002/est2.475.

[35] O. Shi, L. Xu, A. Jiang, Q. Xu, Y. Xiao, D. Zhu, S. Grasso, C. Hu, Synthesis and oxidation resistance of MoAlB single crystals, Ceram Int 45 (2019) 2446–2450. https://doi.org/https://doi.org/10.1016/j.ceramint.2018.10.170.

[36] S. Kota, E. Zapata-Solvas, C. YX, M. Radovic, L. WE, B. MW, Isothermal and Cyclic Oxidation of MoAlB in Air from 1100 degrees C to 1400 degrees C, J Electrochem Soc 164 (2017) C930–C938. https://doi.org/10.1149/2.1891713jes.

[37] S. Kota, Y. Chen, J. Wang, S.J. May, M. Radovic, M.W. Barsoum, Synthesis and characterization of the atomic laminate Mn2AlB2, J Eur Ceram Soc 38 (2018) 5333–5340. https://doi.org/https://doi.org/10.1016/j.jeurceramsoc.2018.07.051.

[38] J. Liu, S. Li, B. Yao, S. Hu, J. Zhang, W. Yu, Y. Zhou, Rapid synthesis and characterization of a nanolaminated Fe2AlB2 compound, J Alloys Compd 766 (2018) 488–497. https://doi.org/https://doi.org/10.1016/j.jallcom.2018.06.352.

[39] Y. Bai, X. Qi, X. He, D. Sun, F. Kong, Y. Zheng, R. Wang, A.I. Duff, Phase stability and weak metallic bonding within ternary-layered borides CrAlB, Cr2AlB2, Cr3AlB4, and Cr4AlB6, Journal of the American Ceramic Society 102 (2019) 3715–3727. https://doi.org/https://doi.org/10.1111/jace.16206.

[40] C. Roy, S. Mondal, P. Banerjee, S. Bhattacharyya, Low temperature atmospheric synthesis of WAlB and Mn2AlB2 MAB phases by modified molten salt shielded synthesis method, Advanced Powder Technology 34 (2023) 103983. https://doi.org/https://doi.org/10.1016/j.apt.2023.103983.

[41] D. Zhang, P. Richardson, M. Wang, L. He, L. Shi, J. Gao, Experimental and theoretical investigation of the damage evolution of irradiated MoAlB and WAlB MAB phases, J Alloys Compd 942 (2023) 169099. https://doi.org/https://doi.org/10.1016/j.jallcom.2023.169099.

[42] T.A. ElMeligy, S. Kota, V. Natu, H. Lind, J. Palisaitis, P.O.Å. Persson, J. Rosen, M.W. Barsoum, Synthesis, characterization, properties, first principles calculations, and X-ray photoelectron spectroscopy of bulk Mn5SiB2 and Fe5SiB2 ternary borides, J Alloys Compd 888 (2021) 161377. https://doi.org/https://doi.org/10.1016/j.jallcom.2021.161377.

[43] D. Pu, Y. Pan, New insight into the structural stability, ductility and melting point of Mo5SiB2 under high-pressure environment, Vacuum 196 (2022) 110727. https://doi.org/https://doi.org/10.1016/j.vacuum.2021.110727.

[44] N. Ni, H. Zhang, Y. Zhou, Electronic structure, bonding characteristics, and mechanical behaviors of a new family of Si-containing damage-tolerant MAB phases M5SiB2 (M = IVB—VIB transition metals), Journal of Advanced Ceramics 11 (2022) 1626–1640. https://doi.org/10.1007/s40145-022-0636-9.

[45] M. Sokol, V. Natu, S. Kota, M.W. Barsoum, On the Chemical Diversity of the MAX Phases, Trends Chem 1 (2019) 210–223. https://doi.org/https://doi.org/10.1016/j.trechm.2019.02.016.

[46] Z.M. Sun, Progress in research and development on MAX phases: a family of layered ternary compounds, International Materials Reviews 56 (2011) 143–166. https://doi.org/10.1179/1743280410Y.0000000001.

[47] L. Fu, W. Xia, MAX Phases as Nanolaminate Materials: Chemical Composition, Microstructure, Synthesis, Properties, and Applications, Adv Eng Mater 23 (2021) 2001191. https://doi.org/https://doi.org/10.1002/adem.202001191.

[48] S. Kota, M. Agne, E. Zapata-Solvas, O. Dezellus, D. Lopez, B. Gardiola, M. Radovic, M.W. Barsoum, Elastic properties, thermal stability, and thermodynamic parameters of MoAlB, Phys. Rev. B 95 (2017) 144108. https://doi.org/10.1103/PhysRevB.95.144108.

[49] M.W. Barsoum, M. Radovic, Elastic and Mechanical Properties of the MAX Phases, Annu Rev Mater Res 41 (2011) 195–227. https://doi.org/10.1146/annurev-matsci-062910-100448.

[50] and elastic properties of the M.T. Scabarozi, T HElectrical, thermal, S. Amini, P. Finkel, O.D. Leaffer, J.E. Spanier, M.W. Barsoum, M. Drulis, H. Drulis, W.M. Tambussi, J.D. Hettinger, S.E. Lofland, Electrical, thermal, and elastic properties of the MAX-phase Ti2SC, J Appl Phys 104 (2008) 33502. https://doi.org/10.1063/1.2959738.

[51] I.M. Low, W.K. Pang, Thermal Stability of MAX Phases, Key Eng Mater 617 (2014) 153–158. https://doi.org/10.4028/www.scientific.net/KEM.617.153.

[52] E. Drouelle, V. Brunet, J. Cormier, P. Villechaise, P. Sallot, F. Naimi, F. Bernard, S. Dubois, Oxidation resistance of Ti3AlC2 and Ti3Al0.8Sn0.2C2 MAX phases: A comparison, Journal of the American Ceramic Society 103 (2020) 1270–1280. https://doi.org/https://doi.org/10.1111/jace.16780.

[53] E. Drouelle, V. Gauthier-Brunet, J. Cormier, P. Villechaise, P. Sallot, F. Naimi, F. Bernard, S. Dubois, Microstructure-oxidation resistance relationship in Ti3AlC2 MAX phase, J Alloys Compd 826 (2020) 154062. https://doi.org/https://doi.org/10.1016/j.jallcom.2020.154062.

[54] C. Guo, E. Wang, S. Wang, X. Hou, Z. He, T. Liang, K.-C. Chou, Oxidation mechanism of MAX phases (Ti3AlC2 powders) with and without Sn doping, Corros Sci 180 (2021) 109197. https://doi.org/https://doi.org/10.1016/j.corsci.2020.109197.

[55] D. Horlait, S. Grasso, N. Al Nasiri, P.A. Burr, W.E. Lee, Synthesis and Oxidation Testing of MAX Phase Composites in the Cr–Ti–Al–C Quaternary System, Journal of the American Ceramic Society 99 (2016) 682–690. https://doi.org/https://doi.org/10.1111/jace.13962.

[56] B. Guedouar, Y. Hadji, A. Benamor, N. Chiker, A. Haddad, A. Tricoteaux, J.-P. Erauw, V. Dupont, F. Hadj-Larbi, M.A. Soualili, M. Hadji, Oxidation behavior of Al-doped Ti3SiC2-20 wt.%Ti5Si3 composite, Ceram Int 47 (2021) 33622–33631. https://doi.org/https://doi.org/10.1016/j.ceramint.2021.08.272.

[57] S. Gupta, M.W. Barsoum, On the tribology of the MAX phases and their composites during dry sliding: A review, Wear 271 (2011) 1878–1894. https://doi.org/https://doi.org/10.1016/j.wear.2011.01.043.

[58] S. Gupta, D. Filimonov, T. Palanisamy, M.W. Barsoum, Tribological behavior of select MAX phases against Al2O3 at elevated temperatures, Wear 265 (2008) 560–565. https://doi.org/https://doi.org/10.1016/j.wear.2007.11.018.

[59] V.D. Jovic, B.M. Jovic, S. Gupta, T. El-Raghy, M.W. Barsoum, Corrosion behavior of select MAX phases in NaOH, HCl and H2SO4, Corros Sci 48 (2006) 4274–4282. https://doi.org/https://doi.org/10.1016/j.corsci.2006.04.005.

[60] R. Pei, S.A. McDonald, L. Shen, S. van der Zwaag, W.G. Sloof, P.J. Withers, P.M. Mummery, Crack healing behaviour of Cr2AlC MAX phase studied by X-ray tomography, J Eur Ceram Soc 37 (2017) 441–450. https://doi.org/https://doi.org/10.1016/j.jeurceramsoc.2016.07.018.

[61] S. Li, L. Xiao, G. Song, X. Wu, W.G. Sloof, S. Van Der Zwaag, Oxidation and crack healing behavior of a fine-grained Cr2 AlC ceramic, Journal of the American Ceramic Society 96 (2013) 892–899. https://doi.org/10.1111/jace.12170.

[62] X. Lu, S. Li, W. Zhang, B. Yao, W. Yu, Y. Zhou, Crack healing behavior of a MAB phase: MoAlB, J Eur Ceram Soc 39 (2019) 4023–4028. https://doi.org/https://doi.org/10.1016/j.jeurceramsoc.2019.05.059.

[63] G. Bei, B.-J. Pedimonte, T. Fey, P. Greil, Oxidation Behavior of MAX Phase Ti2Al(1−x)SnxC Solid Solution, Journal of the American Ceramic Society 96 (2013) 1359–1362. https://doi.org/https://doi.org/10.1111/jace.12358.

[64] A.-S.M. Farle, J. Stikkelman, S. van der Zwaag, W.G. Sloof, Oxidation and self-healing behaviour of spark plasma sintered Ta2AlC, J Eur Ceram Soc 37 (2017) 1969–1974. https://doi.org/https://doi.org/10.1016/j.jeurceramsoc.2017.01.004.

[65] D.J. Tallman, E.N. Hoffman, E.N. Caspi, B.L. Garcia-Diaz, G. Kohse, R.L. Sindelar, M.W. Barsoum, Effect of neutron irradiation on select MAX phases, Acta Mater 85 (2015) 132–143. https://doi.org/https://doi.org/10.1016/j.actamat.2014.10.068.

[66] B. Shalini Reghunath, D. Davis, K.R. Sunaja Devi, Synthesis and characterization of Cr2AlC MAX phase for photocatalytic applications, Chemosphere 283 (2021) 131281. https://doi.org/https://doi.org/10.1016/j.chemosphere.2021.131281.

[67] M.W. Barsoum, M. Radovic, Elastic and Mechanical Properties of the MAX Phases, Annu Rev Mater Res 41 (2011) 195–227. https://doi.org/10.1146/annurev-matsci-062910-100448.

[68] B. et al Manoun, Compression of Zr2InC to 52GPa, Applied Physics Letters 85.9 (2004): 1514-1516. (n.d.).

[69] M.W., et al. Barsoum, Fully reversible, dislocation-based compressive deformation of Ti3SiC2 to 1 GPa, Nature Materials 2.2 (2003): 107-111 (n.d.).

[70] M. Radovic, M.W. Barsoum, T. El-Raghy, S.M. Wiederhorn, W.E. Luecke, Effect of temperature, strain rate and grain size on the mechanical response of Ti3SiC2 in tension, Acta Mater 50 (2002) 1297–1306. https://doi.org/https://doi.org/10.1016/S1359-6454(01)00424-4.

[71] A.G. Zhou, M.W. Barsoum, S. Basu, S.R. Kalidindi, T. El-Raghy, Incipient and regular kink bands in fully dense and 10vol.% porous Ti2AlC, Acta Mater 54 (2006) 1631–1639. https://doi.org/https://doi.org/10.1016/j.actamat.2005.11.035.

[72] M. and M.W.Barsoum. Radovic, MAX phases: bridging the gap between metals and ceramics., American Ceramics Society Bulletin 92.3 (2013): 20-27. (n.d.).

[73] X. and G.Bei. Chen, Toughening mechanisms in nanolayered MAX phase ceramics—A review., Materials 10.4 (2017): 366. (n.d.).

[74] P. Duval, M.F. Ashby, I. Anderman, Rate-controlling processes in the creep of polycrystalline ice, J Phys Chem 87 (1983) 4066–4074. https://doi.org/10.1021/j100244a014.

[75] M.W., L.F. and T.E.-Raghy.. Barsoum, Dislocations, kink bands, and room-temperature plasticity of Ti 3 SiC 2., Metallurgical and Materials Transactions A 30 (1999): 1727-1738 (n.d.).

[76] W. Hu, Z. Huang, Y. Wang, X. Li, H. Zhai, Y. Zhou, L. Chen, Layered ternary MAX phases and their MX particulate derivative reinforced metal matrix composite:A review, J Alloys Compd 856 (2021) 157313. https://doi.org/https://doi.org/10.1016/j.jallcom.2020.157313.

[77] M.A. Hadi, S.H. Naqib, S.-R.G. Christopoulos, A. Chroneos, A.K.M.A. Islam, Mechanical behavior, bonding nature and defect processes of Mo2ScAlC2: A new ordered MAX phase, J Alloys Compd 724 (2017) 1167–1175. https://doi.org/https://doi.org/10.1016/j.jallcom.2017.07.110.

[78] Y. Deng, W. Li, X. Zhang, C. Zhang, Theoretical predictions on temperature-dependent strength for MAX phases, Journal of the American Ceramic Society 104 (2021) 5898–5907. https://doi.org/https://doi.org/10.1111/jace.17977.

[79] H. Högberg, P. Eklund, J. Emmerlich, J. Birch, L. Hultman, Epitaxial Ti2GeC, Ti3GeC2, and Ti4GeC3 MAX-phase thin films grown by magnetron sputtering, J Mater Res 20 (2005) 779–782. https://doi.org/DOI: 10.1557/JMR.2005.0105.

[80] D.J. Fisher, Mechanical Properties of MAX Phases., Materials Research Forum LLC, 2021. (n.d.).

[81] S. Gupta, M.W. Barsoum, On the tribology of the MAX phases and their composites during dry sliding: A review, Wear 271 (2011) 1878–1894. https://doi.org/https://doi.org/10.1016/j.wear.2011.01.043.

[82] Z.M. Sun, Progress in research and development on MAX phases: a family of layered ternary compounds, International Materials Reviews 56 (2011) 143–166. https://doi.org/10.1179/1743280410Y.0000000001.

[83] Y. Bai, F. Kong, X. He, N. Li, X. Qi, Y. Zheng, C. Zhu, R. Wang, A.I. Duff, Thermal shock behavior of Ti2AlC from 200°C to 1400°C, Journal of the American Ceramic Society 100 (2017) 4190–4198. https://doi.org/https://doi.org/10.1111/jace.14965.

[84] M. and M.W.Barsoum. Radovic, MAX phases: bridging the gap between metals and ceramics., American Ceramics Society Bulletin 92.3 (2013): 20-27. (n.d.).

[85] D. Yu, Y. Tan, Oxidation behaviors of compositionally complex MAX phases in air, Ceram Int 47 (2021) 30188–30193. https://doi.org/https://doi.org/10.1016/j.ceramint.2021.07.198.

[86] E. Drouelle, V. Brunet, J. Cormier, P. Villechaise, P. Sallot, F. Naimi, F. Bernard, S. Dubois, Oxidation resistance of Ti3AlC2 and Ti3Al0.8Sn0.2C2 MAX phases: A comparison, Journal of the American Ceramic Society 103 (2020) 1270–1280. https://doi.org/https://doi.org/10.1111/jace.16780.

[87] M. Sokol, V. Natu, S. Kota, M.W. Barsoum, On the Chemical Diversity of the MAX Phases, Trends Chem 1 (2019) 210–223. https://doi.org/https://doi.org/10.1016/j.trechm.2019.02.016.

[88] M.D.L.M.-L.R.S.D.S.M.F.U.W. and C.S.B. Christin M. Hamm, Structural, magnetic and electrical transport properties of non-conventionally prepared MAX phases V2AlC and (V/Mn)2AlC, (n.d.).

[89] A. Mockute, J. Lu, E.J. Moon, M. Yan, B. Anasori, S.J. May, M.W. Barsoum, J. Rosen, Solid Solubility and Magnetism upon Mn Incorporation in the Bulk Ternary Carbides Cr2AlC and Cr2GaC, Mater Res Lett 3 (2015) 16–22. https://doi.org/10.1080/21663831.2014.944676.

[90] Y. Zhou, F. Meng, J. Zhang, New MAX-Phase Compounds in the V–Cr–Al–C System, Journal of the American Ceramic Society 91 (2008) 1357–1360. https://doi.org/https://doi.org/10.1111/j.1551-2916.2008.02279.x.

[91] T. Cabioc'h, P. Eklund, V. Mauchamp, M. Jaouen, Structural investigation of substoichiometry and solid solution effects in Ti2Al(Cx,N1−x)y compounds, J Eur Ceram Soc 32 (2012) 1803–1811. https://doi.org/https://doi.org/10.1016/j.jeurceramsoc.2011.12.011.

[92] T. Lapauw, B. Tunca, D. Potashnikov, A. Pesach, O. Ozeri, J. Vleugels, K. Lambrinou, The double solid solution (Zr, Nb)2(Al, Sn)C MAX phase: a steric stability approach, Sci Rep 8 (2018) 12801. https://doi.org/10.1038/s41598-018-31271-2.

[93] T. Lapauw, D. Tytko, K. Vanmeensel, S. Huang, P.-P. Choi, D. Raabe, E.N. Caspi, O. Ozeri, M. to Baben, J.M. Schneider, K. Lambrinou, J. Vleugels, (Nbx, Zr1–x)4AlC3 MAX Phase Solid Solutions: Processing, Mechanical Properties, and Density Functional Theory Calculations, Inorg Chem 55 (2016) 5445–5452. https://doi.org/10.1021/acs.inorgchem.6b00484.

[94] E.M.D. Siriwardane, T. Birol, O. Erten, D. Çakır, Nanolaminated ${\mathrm{Fe}}_{2}A{\mathrm{B}}_{2}$ and ${\mathrm{Mn}}_{2}A{\mathrm{B}}_{2} (A = \mathrm{Al},\mathrm{Si},\mathrm{Ga},\mathrm{In})$ materials and the assessment of their electronic correlations, Phys Rev Mater 6 (2022) 124005. https://doi.org/10.1103/PhysRevMaterials.6.124005.

[95] L.A. Hanner, S. Kota, M.W. Barsoum, Formation mechanisms of Cr2AlB2, Cr3AlB4, and Fe2AlB2 MAB phases, Mater Res Lett 9 (2021) 323–328. https://doi.org/10.1080/21663831.2021.1912843.

[96] H. Zhang, H. Xiang, F. Dai, Z. Zhang, Y. Zhou, First demonstration of possible two-dimensional MBene CrB derived from MAB phase Cr2AlB2, J Mater Sci Technol 34 (2018) 2022–2026. https://doi.org/https://doi.org/10.1016/j.jmst.2018.02.024.

[97] S. Kota, Y. Chen, J. Wang, S.J. May, M. Radovic, M.W. Barsoum, Synthesis and characterization of the atomic laminate Mn2AlB2, J Eur Ceram Soc 38 (2018) 5333–5340. https://doi.org/https://doi.org/10.1016/j.jeurceramsoc.2018.07.051.

[98] Y. Chen, S. Kota, M.W. Barsoum, M. Radovic, Compressive deformation of MoAlB up to 1100 °C, J Alloys Compd 774 (2019) 1216–1222. https://doi.org/https://doi.org/10.1016/j.jallcom.2018.09.124.

[99] A. Benamor, S. Kota, N. Chiker, A. Haddad, Y. Hadji, V. Natu, S. Abdi, M. Yahi, M.E.A. Benamar, T. Sahraoui, M. Hadji, Michel.W. Barsoum, Friction and wear properties of MoAlB against Al2O3 and 100Cr6 steel counterparts, J Eur Ceram Soc 39 (2019) 868–877. https://doi.org/https://doi.org/10.1016/j.jeurceramsoc.2018.10.026.

[100] X. Lu, S. Li, W. Zhang, W. Yu, Y. Zhou, Thermal shock behavior of a nanolaminated ternary boride: MoAlB, Ceram Int 45 (2019) 9386–9389. https://doi.org/https://doi.org/10.1016/j.ceramint.2018.08.071.

[101] J. Cedervall, M.S. Andersson, T. Sarkar, E.K. Delczeg-Czirjak, L. Bergqvist, T.C. Hansen, P. Beran, P. Nordblad, M. Sahlberg, Magnetic structure of the magnetocaloric compound AlFe2B2, J Alloys Compd 664 (2016) 784–791. https://doi.org/https://doi.org/10.1016/j.jallcom.2015.12.111.

[102] R. Barua, B.T. Lejeune, L. Ke, G. Hadjipanayis, E.M. Levin, R.W. McCallum, M.J. Kramer, L.H. Lewis, Anisotropic magnetocaloric response in AlFe2B2, J Alloys Compd 745 (2018) 505–512. https://doi.org/https://doi.org/10.1016/j.jallcom.2018.02.205.

[103] X. Tan, P. Chai, C.M. Thompson, M. Shatruk, Magnetocaloric Effect in AlFe2B2: Toward Magnetic Refrigerants from Earth-Abundant Elements, J Am Chem Soc 135 (2013) 9553–9557. https://doi.org/10.1021/ja404107p.

[104] Q. Du, G. Chen, W. Yang, Z. Song, M. Hua, H. Du, C. Wang, S. Liu, J. Han, Y. Zhang, J. Yang, Magnetic properties of AlFe2B2 and CeMn2Si2 synthesized by melt spinning of stoichiometric compositions, Jpn J Appl Phys 54 (2015) 053003. https://doi.org/10.7567/JJAP.54.053003.

[105] Y. Hadji, A. Tricoteaux, M.G. Ben Ghorbal, M. Yahi, R. Badji, T. Sahraoui, M. Hadji, M.W. Barsoum, Microstructure and microindentation of Ti3SiC2 – Titanium filler brazed joints by tungsten inert gas (TIG) process, Ceram Int 43 (2017) 7290–7294. https://doi.org/https://doi.org/10.1016/j.ceramint.2017.03.028.

[106] N. Chiker, A. Haddad, Y. Hadji, M.E.A. Benammar, M. Azzaz, M. Yahi, T. Sahraoui, M. Hadji, M.W. Barsoum, Infiltration behavior of Cu and Ti fillers into Ti2AlC/Ti3AlC2 composites during tungsten inert gas (TIG)brazing, Ceram Int 44 (2018) 3282–3290. https://doi.org/https://doi.org/10.1016/j.ceramint.2017.11.102.

[107] Y. Hadji, A. Haddad, M. Yahi, M.E.A. Benamar, D. Miroud, T. Sahraoui, M. Hadji, M.W. Barsoum, Joining Ti3SiC2 MAX phase with 308 stainless steel and aluminum fillers by tungsten inert gas (TIG)-brazing process, Ceram Int 42 (2016) 1026–1035. https://doi.org/https://doi.org/10.1016/j.ceramint.2015.09.026.

[108] Z. Sun, Y. Zhou, M. Li, Oxidation behaviour of Ti 3 SiC 2 -based ceramic at 900 - 1300 ° C in air, Corros Sci 43 (2001) 1095–1109.

[109] Z. Sun, Y. Zhou, M. Li, HIGH TEMPERATURE OXIDATION BEHAVIOR OF Ti 3 SiC 2 - BASED MATERIAL IN AIR, Acta Mater 49 (2001) 4347–4353.

[110] M.W. Barsoum, The Mn+1 AXn Phases : A New Class of Solids ; thermodynamically stable nanolaminates, 28 (2000) 201–281.

[111] S. Gupta, A. Ganguly, D. Filimonov, M.W. Barsoum, Oxidation of Ti3GeC2 and Ti3Ge0.5Si0.5C2 in air, J. Electrochem. Soc. (2006) 61–68. https://doi.org/10.1149/1.2199287.

[112] M.W. Barsoum, N. Tzenov, A. Procopio, M. Ali, Oxidation of Tin+1AlXn (n = 1-3 and X = C , N) II . Experimental Results, J Electrochem Soc (2001) c551–c562. https://doi.org/10.1149/1.1380256.

[113] P. Taylor, D.J. Tallman, B. Anasori, M.W. Barsoum, A Critical Review of the Oxidation of Ti 2 AlC , Ti 3 AlC 2 and Cr 2 AlC in Air, (2013) 37–41. https://doi.org/10.1080/21663831.2013.806364.

[114] S. Gupta, A. Ganguly, D. Filimonov, M.W. Barsoum, Oxidation of Ti3GeC2 and Ti3Ge0.5Si0.5C2 in air, J. Electrochem. Soc. (2006) 61–68. https://doi.org/10.1149/1.2199287.

[115] M.W. Barsoum, MAX Phases: Properties of machinable ternary carbides and nitrides, 2013.

[116] G.M. Song, Y.T. Pei, W.G. Sloof, S.B. Li, J.T.M. De Hosson, S. van der Zwaag, Oxidation-induced crack healing in Ti3AlC2 ceramics, Scr Mater 58 (2008) 13–16. https://doi.org/10.1016/j.scriptamat.2007.09.006.

[117] S. Li, G. Song, K. Kwakernaak, S. van der Zwaag, W.G. Sloof, Multiple crack healing of a Ti 2AlC ceramic, J Eur Ceram Soc 32 (2012) 1813–1820. https://doi.org/10.1016/j.jeurceramsoc.2012.01.017.

[118] S. Li, G. Song, K. Kwakernaak, S. van der Zwaag, W.G. Sloof, Multiple crack healing of a Ti 2AlC ceramic, J Eur Ceram Soc 32 (2012) 1813–1820. https://doi.org/10.1016/j.jeurceramsoc.2012.01.017.

[119] S. Li, G. Bei, X. Chen, L. Zhang, Y. Zhou, M. Mačković, E. Spiecker, P. Greil, Crack healing induced electrical and mechanical properties recovery in a Ti2SnC ceramic, J Eur Ceram Soc 36 (2016) 25–32. https://doi.org/10.1016/j.jeurceramsoc.2015.09.019.

[120] S. Gupta, T. Hammann, R. Johnson, M.F. Riyad, Synthesis and Characterization of Novel Al-Matrix Composites Reinforced with Ti 3 SiC 2 Particulates, (2014). https://doi.org/10.1007/s11665-014-1330-z.

[121] S. Amini, M.W. Barsoum, On the effect of texture on the mechanical and damping properties of nanocrystalline Mg-matrix composites reinforced with MAX phases, Materials Science & Engineering A 527 (2010) 3707–3718. https://doi.org/10.1016/j.msea.2010.01.073.

[122] S. Gupta, T. Hammann, R. Johnson, M.F. Riyad, Synthesis and Characterization of Novel Al-Matrix Composites Reinforced with Ti 3 SiC 2 Particulates, (2014). https://doi.org/10.1007/s11665-014-1330-z.

[123] S. Gupta, D. Filimonov, T. Palanisamy, T. El-raghy, M.W. Barsoum, Ta 2 AlC and Cr 2 AlC Ag-based composites — New solid lubricant materials for use over a wide temperature range against Ni-based superalloys and alumina, 262 (2007) 1479–1489. https://doi.org/10.1016/j.wear.2007.01.028.

[124] M.H. Abdessabour Benamor, Youcef Hadji, Nabil Chiker, Adel Haddad, Bendiba Guedouar, Mohamed Labaiz, Maamar Hakem, Arnaud Tricoteaux, Christelle Nivot, Jean Pierre Erauw, Riad Badji, Spark Plasma Sintering and tribological behavior of Ti3SiC2–Ti5Si3–TiC composites, Ceram Int (2019). https://doi.org/https://doi.org/10.1016/j.ceramint.2019.07.181.

[125] M.Hadji. Youcef Hadji, Abdessabour Benamor, Nabil Chiker, Adel Haddad, Nacer Tala-Ighil, Jean-Pierre Erauw, Vedi Dupont, Arnaud Tricoteaux, Christelle Nivot, Anthony Thuault, Tribological behavior of composites fabricated by reactive SPS sintering in Ti-Si-C system, Int J Appl Ceram Technol (2019). https://doi.org/https://doi.org/10.1111/ijac.13443.

[126] S. Amini, M.W. Barsoum, On the effect of texture on the mechanical and damping properties of nanocrystalline Mg-matrix composites reinforced with MAX phases, Materials Science & Engineering A 527 (2010) 3707–3718. https://doi.org/10.1016/j.msea.2010.01.073.

[127] I. Relation, Cu / Ti 3 SiC 2 composite : a new electrofriction material, (1999) 80–84.

[128] C. Healing, A. Sn, C.A.O. Composites, G.P. Bei, B.J. Pedimonte, M. Pezoldt, J. Ast, T. Fey, M. Goeken, P. Greil, Guo Ping Bei, ‡ , † Birgit Joana Pedimonte, ‡ Marc Pezoldt, ‡ Johannes Ast, § Tobias Fey, ‡ Mathias Goeken, § and Peter Greil ‡ ‡, 1610 (2015) 1604–1611. https://doi.org/10.1111/jace.13496.

[129] M. Stumpf, J. Biggemann, T. Fey, K. Kakimoto, P. Greil, Thermochemical calculations of the oxidation behavior of Nb 2 AlC MAX phase in ZrO 2 – matrix composites, (2018). https://doi.org/10.1016/j.ceramint.2018.05.249.

[130] T. Lapauw, K. Lambrinou, T. Cabioc'h, J. Halim, J. Lu, A. Pesach, O. Rivin, O. Ozeri, E.N. Caspi, L. Hultman, P. Eklund, J. Rosén, M.W. Barsoum, J. Vleugels, Synthesis of the new MAX phase Zr2AlC, J Eur Ceram Soc 36 (2016) 1847–1853. https://doi.org/https://doi.org/10.1016/j.jeurceramsoc.2016.02.044.

[131] F. Zakeri-Shahroudi, B. Ghasemi, H. Abdolahpour, M. Razavi, Sintering behavior of Cr2AlC MAX phase synthesized by Spark plasma sintering, Int J Appl Ceram Technol 19 (2022) 1309–1318. https://doi.org/https://doi.org/10.1111/ijac.13995.

[132] J. Lyu, E.B. Kashkarov, N. Travitzky, M.S. Syrtanov, A.M. Lider, Sintering of MAX-phase materials by spark plasma and other methods, J Mater Sci 56 (2021) 1980–2015. https://doi.org/10.1007/s10853-020-05359-y.

[133] J. Lyu, E.B. Kashkarov, N. Travitzky, M.S. Syrtanov, A.M. Lider, Sintering of MAX-phase materials by spark plasma and other methods, J Mater Sci 56 (2021) 1980–2015. https://doi.org/10.1007/s10853-020-05359-y.

[134] Y. Gong, W. Tian, P. Zhang, J. Chen, Y. Zhang, Z. Sun, Slip casting and pressureless sintering of Ti3AlC2, Journal of Advanced Ceramics 8 (2019) 367–376. https://doi.org/10.1007/s40145-019-0318-4.

[135] Y. Bai, X. He, R. Wang, Y. Sun, C. Zhu, S. Wang, G. Chen, High temperature physical and mechanical properties of large-scale Ti2AlC bulk synthesized by self-propagating high temperature combustion synthesis with pseudo hot isostatic pressing, J Eur Ceram Soc 33 (2013) 2435–2445. https://doi.org/https://doi.org/10.1016/j.jeurceramsoc.2013.04.014.

[136] J.M. Córdoba, M.J. Sayagués, M.D. Alcalá, F.J. Gotor, Synthesis of Ti3SiC2 Powders: Reaction Mechanism, Journal of the American Ceramic Society 90 (2007) 825–830. https://doi.org/https://doi.org/10.1111/j.1551-2916.2007.01501.x.

[137] J. Liu, S. Li, B. Yao, S. Hu, J. Zhang, W. Yu, Y. Zhou, Rapid synthesis and characterization of a nanolaminated Fe2AlB2 compound, J Alloys Compd 766 (2018) 488–497. https://doi.org/10.1016/j.jallcom.2018.06.352.

[138] B. Wang, A. Zhou, Q. Hu, L. Wang, Synthesis and oxidation resistance of V2AlC powders by molten salt method, Int J Appl Ceram Technol 14 (2017) 873–879. https://doi.org/https://doi.org/10.1111/ijac.12723.

[139] X. Guo, J. Wang, S. Yang, L. Gao, B. Qian, Preparation of Ti3SiC2 powders by the molten salt method, Mater Lett 111 (2013) 211–213. https://doi.org/https://doi.org/10.1016/j.matlet.2013.08.077.

[140] Y. Wang, L.X. Yang, R.J. Liu, H.J. Liu, C.L. Zeng, S.L. Zhu, C. Fu, Ternary-layered Cr2AlB2 synthesized from Cr, Al, and B powders by a molten salt-assisted method, Powder Technol 387 (2021) 354–362. https://doi.org/https://doi.org/10.1016/j.powtec.2021.04.042.

[141] C. Roy, P. Banerjee, S. Bhattacharyya, Molten salt shielded synthesis (MS3) of Ti2AlN and V2AlC MAX phase powders in open air, J Eur Ceram Soc 40 (2020) 923–929. https://doi.org/https://doi.org/10.1016/j.jeurceramsoc.2019.10.020.

[142] A. Dash, R. Vaßen, O. Guillon, J. Gonzalez-Julian, Molten salt shielded synthesis of oxidation prone materials in air, Nat Mater 18 (2019) 465–470. https://doi.org/10.1038/s41563-019-0328-1.

[143] R. Ullah, W. Ahmad, I. Ahmad, M. Khan, M. Iqbal Khattak, F. Hussain, Adsorption and recovery of hexavalent chromium from tannery wastewater over magnetic max phase composite, Sep Sci Technol 56 (2021) 439–452. https://doi.org/10.1080/01496395.2020.1717531.

[144] Z. Ansarian, A. Khataee, S. Arefi-Oskoui, Y. Orooji, H. Lin, Ultrasound-assisted catalytic activation of peroxydisulfate on Ti3GeC2 MAX phase for efficient removal of hazardous pollutants, Mater Today Chem 24 (2022) 100818. https://doi.org/https://doi.org/10.1016/j.mtchem.2022.100818.

[145] S. Haddadi, A. Khataee, S. Arefi-Oskoui, B. Vahid, Y. Orooji, Y. Yoon, Titanium-based MAX-phase with sonocatalytic activity for degradation of oxytetracycline antibiotic, Ultrason Sonochem 92 (2023) 106255. https://doi.org/https://doi.org/10.1016/j.ultsonch.2022.106255.

[146] M. Naguib, J. Come, B. Dyatkin, V. Presser, P.-L. Taberna, P. Simon, M.W. Barsoum, Y. Gogotsi, MXene: a promising transition metal carbide anode for lithium-ion batteries, Electrochem Commun 16 (2012) 61–64. https://doi.org/https://doi.org/10.1016/j.elecom.2012.01.002.

[147] G. Kresse, J. Furthmüller, Efficiency of ab-initio total energy calculations for metals and semiconductors using a plane-wave basis set, Comput. Mater. Sci. 6 (1996) 15.

[148] P. Simon, Y. Gogotsi, B. Dunn, Where Do Batteries End and Supercapacitors Begin?, Science (1979) 343 (2014) 1210 LP – 1211. https://doi.org/10.1126/science.1249625.

[149] TEH WEN SHUN, ADSORPTION-PHOTOCATALYSIS OF MALACHITE GREEN USING TITANIUM DIOXIDE AND EMPTY FRUIT BUNCH DERIVEDACTIVATED CARBON, n.d.

[150] O. Salim, K.A. Mahmoud, K.K. Pant, R.K. Joshi, Introduction to MXenes: synthesis and characteristics, Mater Today Chem 14 (2019) 100191. https://doi.org/https://doi.org/10.1016/j.mtchem.2019.08.010.

[151] M. Khazaei, M. Arai, T. Sasaki, C.-Y. Chung, N.S. Venkataramanan, M. Estili, Y. Sakka, Y. Kawazoe, Novel Electronic and Magnetic Properties of Two-Dimensional Transition Metal Carbides and Nitrides, Adv Funct Mater 23 (2013) 2185–2192. https://doi.org/https://doi.org/10.1002/adfm.201202502.

[152] M. Ashton, K. Mathew, R.G. Hennig, S.B. Sinnott, Predicted Surface Composition and Thermodynamic Stability of MXenes in Solution, The Journal of Physical Chemistry C 120 (2016) 3550–3556. https://doi.org/10.1021/acs.jpcc.5b11887.

[153] P.O.Å. Persson, MXene Surface Chemistry, in: B. Anasori, Y. Gogotsi (Eds.), 2D Metal Carbides and Nitrides (MXenes): Structure, Properties and Applications, Springer International Publishing, Cham, 2019: pp. 125–136. https://doi.org/10.1007/978-3-030-19026-2_8.

[154] M. Naguib, O. Mashtalir, J. Carle, V. Presser, J. Lu, L. Hultman, Y. Gogotsi, M.W. Barsoum, Two-Dimensional Transition Metal Carbides, ACS Nano 6 (2012) 1322–1331. https://doi.org/10.1021/nn204153h.

[155] M. Naguib, J. Halim, J. Lu, K.M. Cook, L. Hultman, Y. Gogotsi, M.W. Barsoum, New Two-Dimensional Niobium and Vanadium Carbides as Promising Materials for Li-Ion Batteries, J Am Chem Soc 135 (2013) 15966–15969. https://doi.org/10.1021/ja405735d.

[156] B. Anasori, Y. Xie, M. Beidaghi, J. Lu, B.C. Hosler, L. Hultman, P.R.C. Kent, Y. Gogotsi, M.W. Barsoum, Two-Dimensional, Ordered, Double Transition Metals Carbides (MXenes), ACS Nano 9 (2015) 9507–9516. https://doi.org/10.1021/acsnano.5b03591.

[157] M. Hu, T. Hu, R. Cheng, J. Yang, C. Cui, C. Zhang, X. Wang, MXene-coated silk-derived carbon cloth toward flexible electrode for supercapacitor application, Journal of Energy Chemistry 27 (2018) 161–166. https://doi.org/https://doi.org/10.1016/j.jechem.2017.10.030.

[158] M.A. Hope, A.C. Forse, K.J. Griffith, M.R. Lukatskaya, M. Ghidiu, C.P. Grey, NMR reveals the surface functionalisation of Ti 3 C 2, Physical Chemistry Chemical Physics 18 (2016) 5099–5102. https://doi.org/10.1039/C6CP00330C.

[159] M. Ghidiu, M.R. Lukatskaya, M. Zhao, Y. Gogotsi, M.W. Barsoum, Conductive two-dimensional titanium carbide 'clay' with high volumetric capacitance, Nature 516 (2014) 78–81. https://doi.org/10.1038/nature13970.

[160] X. Wang, C. Garnero, G. Rochard, D. Magne, S. Morisset, S. Hurand, P. Chartier, J. Rousseau, T. Cabioc'h, C. Coutanceau, V. Mauchamp, S. Célérier, A new etching environment (FeF3/HCl) for the synthesis of two-dimensional titanium carbide MXenes: a route towards selective reactivity vs. water, J Mater Chem A Mater 5 (2017) 22012–22023. https://doi.org/10.1039/C7TA01082F.

[161] A.S. Yang, P. Zhang, F. Wang, A. Gaetano, M.R. Lohe, P.W.M. Blom, Angewandte Chemie, (n.d.). https://doi.org/10.1002/ange.201809662.

[162] A.T. Li, L. Yao, Q. Liu, J. Gu, R. Luo, J. Li, X. Yan, W. Wang, P. Liu, B. Chen, W. Zhang, W. Abbas, R. Naz, D. Zhang, Chemie, (n.d.). https://doi.org/10.1002/anie.201800887.

[163] G. Li, L. Tan, Y. zhang, B. Wu, L. Li, Highly Efficiently Delaminated Single-Layered MXene Nanosheets with Large Lateral Size, Langmuir 33 (2017) 9000–9006. https://doi.org/10.1021/acs.langmuir.7b01339.

[164] B. Soundiraraju, R. Raghavan, B.K. George, Chromium Carbide Nanosheets Prepared by Selective Etching of Aluminum from Cr2AlC for Hydrazine Detection, ACS Appl Nano Mater 3 (2020) 11007–11016. https://doi.org/10.1021/acsanm.0c02230.

[165] X. Zou, H. Liu, H. Xu, X. Wu, X. Han, J. Kang, K.M. Reddy, A simple approach to synthesis Cr2CTx MXene for efficient hydrogen evolution reaction, Mater Today Energy 20 (2021). https://doi.org/10.1016/j.mtener.2021.100668.

[166] J. Halim, M.R. Lukatskaya, K.M. Cook, J. Lu, C.R. Smith, L.-Å. Näslund, S.J. May, L. Hultman, Y. Gogotsi, P. Eklund, M.W. Barsoum, Transparent Conductive Two-Dimensional Titanium Carbide Epitaxial Thin Films, Chemistry of Materials 26 (2014) 2374–2381. https://doi.org/10.1021/cm500641a.

[167] M.R. Lukatskaya, S. Kota, Z. Lin, M.-Q. Zhao, N. Shpigel, M.D. Levi, J. Halim, P.-L. Taberna, M.W. Barsoum, P. Simon, Y. Gogotsi, Ultra-high-rate pseudocapacitive energy storage in two-

dimensional transition metal carbides, Nat Energy 2 (2017) 17105. https://doi.org/10.1038/nenergy.2017.105.

[168] F.Z.X.S.H.P. Yangfan Shao, N-Functionalized MXenes: ultrahigh carrier mobility and multifunctional properties, Chem. Soc. Rev., 2021,50, 12338-12376 (n.d.).

[169] K.L.Q.L.Q.H.J.H.X.W. and S. Du Xian-Hu Zha, Role of the surface effect on the structural, electronic and mechanical properties of the carbide MXenes, (n.d.).

[170] J.Z.C.S. and Z.S. Zhonglu Guo, Flexible two-dimensional Tin+1Cn (n = 1, 2 and 3) and their functionalized MXenes predicted by density functional theories, (n.d.).

[171] A.Ö.N.K.P.F.A. and C.S. Uğur Yorulmaz, Vibrational and mechanical properties of single layer MXene structures: a first-principles investigation, 2016 Nanotechnology 27 335702 (n.d.).

[172] V.N.M. and Y.G. Vadym N Borysiuk, Molecular dynamic study of the mechanical properties of two-dimensional titanium carbides Tin+1Cn (MXenes), Nanotechnology 26 265705 (n.d.).

[173] Y. Wang, Y. Xu, M. Hu, H. Ling, X. Zhu, MXenes: focus on optical and electronic properties and corresponding applications, 9 (2020) 1601–1620. https://doi.org/doi:10.1515/nanoph-2019-0556.

[174] M. Khazaei, M. Arai, T. Sasaki, C.-Y. Chung, N.S. Venkataramanan, M. Estili, Y. Sakka, Y. Kawazoe, Novel Electronic and Magnetic Properties of Two-Dimensional Transition Metal Carbides and Nitrides, Adv Funct Mater 23 (2013) 2185–2192. https://doi.org/https://doi.org/10.1002/adfm.201202502.

[175] L. Hong, R.F. Klie, S. Öğüt, First-principles study of size- and edge-dependent properties of MXene nanoribbons, Phys Rev B 93 (2016) 115412. https://doi.org/10.1103/PhysRevB.93.115412.

[176] R. Momeni Feili, M. Dadsetani, R. Nejatipour, A. Ebrahimian, Electron Energy Loss Structures of Terminated Scandium and Hafnium MXene Monolayers from First-Principles Calculations, J Electron Mater 49 (2020) 2502–2520. https://doi.org/10.1007/s11664-020-07946-w.

[177] M. Khazaei, A. Ranjbar, M. Arai, T. Sasaki, S. Yunoki, Electronic properties and applications of MXenes: a theoretical review, J Mater Chem C Mater 5 (2017) 2488–2503. https://doi.org/10.1039/C7TC00140A.

[178] Y. Lee, Y. Hwang, S.B. Cho, Y.-C. Chung, Achieving a direct band gap in oxygen functionalized-monolayer scandium carbide by applying an electric field, Physical Chemistry Chemical Physics 16 (2014) 26273–26278. https://doi.org/10.1039/C4CP03811H.

[179] Y. Lee, S.B. Cho, Y.-C. Chung, Tunable Indirect to Direct Band Gap Transition of Monolayer Sc2CO2 by the Strain Effect, ACS Appl Mater Interfaces 6 (2014) 14724–14728. https://doi.org/10.1021/am504233d.

[180] X. Yu, J. Cheng, Z. Liu, Q. Li, W. Li, X. Yang, B. Xiao, The band gap modulation of monolayer Ti2CO2 by strain, RSC Adv 5 (2015) 30438–30444. https://doi.org/10.1039/C5RA01586C.

[181] A.N. Gandi, H.N. Alshareef, U. Schwingenschlögl, Thermoelectric Performance of the MXenes M2CO2 (M = Ti, Zr, or Hf), Chemistry of Materials 28 (2016) 1647–1652. https://doi.org/10.1021/acs.chemmater.5b04257.

[182] M.R. Lukatskaya, O. Mashtalir, C.E. Ren, Y. Dall'Agnese, P. Rozier, P.L. Taberna, M. Naguib, P. Simon, M.W. Barsoum, Y. Gogotsi, Cation Intercalation and High Volumetric Capacitance

of Two-Dimensional Titanium Carbide, Science (1979) 341 (2013) 1502–1505. https://doi.org/10.1126/science.1241488.

[183] Y.G. Babak Anasori, 2D Metal Carbides and Nitrides (MXenes), n.d.

[184] J.A. Kumar, P. Prakash, T. Krithiga, D.J. Amarnath, J. Premkumar, N. Rajamohan, Y. Vasseghian, P. Saravanan, M. Rajasimman, Methods of synthesis, characteristics, and environmental applications of MXene: A comprehensive review, Chemosphere 286 (2022) 131607. https://doi.org/https://doi.org/10.1016/j.chemosphere.2021.131607.

[185] L. Dong, M. Dai, H. Liang, N. Zhang, N. Mancheri, J. Ren, Y. Dou, M. Hu, Material flows and resource productivity in China, South Korea and Japan from 1970 to 2008: A transitional perspective, J Clean Prod 141 (2017) 1164–1177. https://doi.org/https://doi.org/10.1016/j.jclepro.2016.09.189.

[186] X. Li, Y. Liu, J. Wang, J. Gascon, J. Li, B. Van der Bruggen, Metal–organic frameworks based membranes for liquid separation, Chem Soc Rev 46 (2017) 7124–7144. https://doi.org/10.1039/C7CS00575J.

[187] C.E. Ren, K.B. Hatzell, M. Alhabeb, Z. Ling, K.A. Mahmoud, Y. Gogotsi, Charge- and Size-Selective Ion Sieving Through Ti3C2Tx MXene Membranes, J Phys Chem Lett 6 (2015) 4026–4031. https://doi.org/10.1021/acs.jpclett.5b01895.

[188] R. Han, RSC Advances membrane with excellent hydrophilicity and high, RSC Adv 7 (2017) 56204–56210. https://doi.org/10.1039/C7RA10318B.

[189] L. Ding, Y. Wei, Y. Wang, H. Chen, J. Caro, H. Wang, Zuschriften Membranes A Two-Dimensional Lamellar Membrane : MXene Nanosheet Stacks Zuschriften Angewandte, (2017) 1–6. https://doi.org/10.1002/ange.201609306.

[190] G. Liu, J. Shen, Q. Liu, G. Liu, J. Xiong, J. Yang, W. Jin, Ultrathin two-dimensional MXene membrane for pervaporation desalination, J Memb Sci 548 (2018) 548–558. https://doi.org/https://doi.org/10.1016/j.memsci.2017.11.065.

[191] O. Mashtalir, K.M. Cook, V.N. Mochalin, M. Crowe, M.W. Barsoum, Y. Gogotsi, Dye adsorption and decomposition on two-dimensional titanium carbide in aqueous media, J Mater Chem A Mater 2 (2014) 14334–14338. https://doi.org/10.1039/c4ta02638a.

[192] Y. Gao, L. Wang, A. Zhou, Z. Li, J. Chen, H. Bala, Q. Hu, X. Cao, Hydrothermal synthesis of TiO2/Ti3C2 nanocomposites with enhanced photocatalytic activity, Mater Lett 150 (2015) 62–64. https://doi.org/https://doi.org/10.1016/j.matlet.2015.02.135.

[193] C. Peng, X. Yang, Y. Li, H. Yu, H. Wang, F. Peng, Hybrids of Two-Dimensional Ti3C2 and TiO2 Exposing {001} Facets toward Enhanced Photocatalytic Activity, ACS Appl Mater Interfaces 8 (2016) 6051–6060. https://doi.org/10.1021/acsami.5b11973.

[194] W. Zhou, J. Zhu, F. Wang, M. Cao, T. Zhao, One-step synthesis of Ceria/Ti3C2 nanocomposites with enhanced photocatalytic activity, Mater Lett 206 (2017) 237–240. https://doi.org/https://doi.org/10.1016/j.matlet.2017.06.117.

[195] Y. Lu, M. Yao, A. Zhou, Q. Hu, L. Wang, Preparation and Photocatalytic Performance of Ti 3 C 2 / TiO 2 / CuO Ternary Nanocomposites, 2017 (2017) 1–6.

[196] D.S. Lee, Two-Dimensional Ti 3 C 2 T, (2017). https://doi.org/10.1021/acssuschemeng.7b02695.

[197] Y. Ying, Y. Liu, X. Wang, Y. Mao, W. Cao, P. Hu, X. Peng, Two-Dimensional Titanium Carbide for E ffi ciently Reductive Removal of Highly Toxic Chromium (VI) from Water, (n.d.). https://doi.org/10.1021/am5074722.

[198] O. Mashtalir, M. Naguib, V.N. Mochalin, Y.D. Agnese, M. Heon, M.W. Barsoum, Y. Gogotsi, Intercalation and delamination of layered carbides and carbonitrides, (2013) 1–7. https://doi.org/10.1038/ncomms2664.

[199] L.W.N.Z. and Z.Z. Yujuan Zhang, Adsorptive environmental applications of MXene nanomaterials: a review, RSC Adv., 2018, 8, 19895-19905 (n.d.).

[200] Q. Peng, J. Guo, Q. Zhang, J. Xiang, B. Liu, A. Zhou, R. Liu, Y. Tian, Unique lead adsorption behavior of activated hydroxyl group in two-dimensional titanium carbide, J Am Chem Soc 136 (2014) 4113–4116. https://doi.org/10.1021/ja500506k.

[201] J. Guo, H. Fu, G. Zou, Q. Zhang, Z. Zhang, Q. Peng, Theoretical interpretation on lead adsorption behavior of new two-dimensional transition metal carbides and nitrides, J Alloys Compd 684 (2016) 504–509. https://doi.org/https://doi.org/10.1016/j.jallcom.2016.05.217.

[202] Q. Zhang, J. Teng, G. Zou, Q. Peng, Q. Du, T. Jiao, J. Xiang, Efficient phosphate sequestration for water purification by unique sandwich-like MXene/magnetic iron oxide nanocomposites, Nanoscale 8 (2016) 7085–7093. https://doi.org/10.1039/C5NR09303A.

[203] A.A. Shahzad, K. Rasool, W. Miran, M. Nawaz, J. Jang, K.A. Mahmoud, D. Sung, Mercuric Ion Capturing by Recoverable Titanium Carbide Magnetic Nanocomposite, J Hazard Mater (2017). https://doi.org/10.1016/j.jhazmat.2017.11.026.

[204] Z. Wei, Z. Peigen, T. Wubian, Q. Xia, Z. Yamei, S. ZhengMing, Alkali treated Ti3C2Tx MXenes and their dye adsorption performance, Mater Chem Phys 206 (2018) 270–276. https://doi.org/10.1016/j.matchemphys.2017.12.034.

[205] B.-M. Jun, J. Heo, N. Taheri-Qazvini, C.M. Park, Y. Yoon, Adsorption of selected dyes on Ti3C2Tx MXene and Al-based metal-organic framework, Ceram Int 46 (2020) 2960–2968. https://doi.org/https://doi.org/10.1016/j.ceramint.2019.09.293.

[206] C. Cai, R. Wang, S. Liu, X. Yan, L. Zhang, M. Wang, Q. Tong, T. Jiao, Synthesis of self-assembled phytic acid-MXene nanocomposites via a facile hydrothermal approach with elevated dye adsorption capacities, Colloids Surf A Physicochem Eng Asp 589 (2020) 124468. https://doi.org/https://doi.org/10.1016/j.colsurfa.2020.124468.

[207] Z. Wei, Z. Peigen, T. Wubian, Q. Xia, Z. Yamei, Alkali treated Ti 3 C 2 T x MXenes and their dye adsorption performance, Mater Chem Phys 206 (2018) 270–276. https://doi.org/10.1016/j.matchemphys.2017.12.034.

[208] C. Cai, R. Wang, S. Liu, X. Yan, L. Zhang, M. Wang, Q. Tong, T. Jiao, Synthesis of self-assembled phytic acid-MXene nanocomposites via a facile hydrothermal approach with elevated dye adsorption capacities, Colloids Surf A Physicochem Eng Asp 589 (2020) 124468. https://doi.org/https://doi.org/10.1016/j.colsurfa.2020.124468.

[209] B. Sun, X. Dong, H. Li, Y. Shang, Y. Zhang, F. Hu, S. Gu, Y. Wu, T. Gao, G. Zhou, Surface charge engineering for two-dimensional Ti2CTx MXene for highly efficient and selective removal of cationic dye from aqueous solution, Sep Purif Technol 272 (2021) 118964. https://doi.org/https://doi.org/10.1016/j.seppur.2021.118964.

[210] N. My Tran, Q. Thanh Hoai Ta, A. Sreedhar, J.-S. Noh, Ti3C2Tx MXene playing as a strong methylene blue adsorbent in wastewater, Appl Surf Sci 537 (2021) 148006. https://doi.org/https://doi.org/10.1016/j.apsusc.2020.148006.

[211] C. Peng, P. Wei, X. Chen, Y. Zhang, F. Zhu, Y. Cao, H. Wang, H. Yu, F. Peng, A hydrothermal etching route to synthesis of 2D MXene (Ti3C2, Nb2C): Enhanced exfoliation and improved adsorption performance, Ceram Int 44 (2018) 18886–18893. https://doi.org/https://doi.org/10.1016/j.ceramint.2018.07.124.

[212] S. Zhang, S. Liao, F. Qi, R. Liu, T. Xiao, J. Hu, K. Li, R. Wang, Y. Min, Direct deposition of two-dimensional MXene nanosheets on commercially available filter for fast and efficient dye removal, J Hazard Mater 384 (2020) 121367. https://doi.org/https://doi.org/10.1016/j.jhazmat.2019.121367.

[213] Y. Li, C. Pan, P. Kamdem, X.-J. Jin, Binder-Free Two-Dimensional MXene/Acid Activated Carbon for High-Performance Supercapacitors and Methylene Blue Adsorption, Energy & Fuels 34 (2020) 10120–10130. https://doi.org/10.1021/acs.energyfuels.0c01352.

[214] Y. Lei, Y. Cui, Q. Huang, J. Dou, D. Gan, F. Deng, M. Liu, X. Li, X. Zhang, Y. Wei, Facile preparation of sulfonic groups functionalized Mxenes for efficient removal of methylene blue, Ceram Int 45 (2019) 17653–17661. https://doi.org/https://doi.org/10.1016/j.ceramint.2019.05.331.

[215] Z.-H. Zhang, J.-Y. Xu, X.-L. Yang, MXene/sodium alginate gel beads for adsorption of methylene blue, Mater Chem Phys 260 (2021) 124123. https://doi.org/https://doi.org/10.1016/j.matchemphys.2020.124123.

[216] Y. Feng, H. Wang, J. Xu, X. Du, X. Cheng, Z. Du, H. Wang, Fabrication of MXene/PEI functionalized sodium alginate aerogel and its excellent adsorption behavior for Cr(VI) and Congo Red from aqueous solution, J Hazard Mater 416 (2021) 125777. https://doi.org/https://doi.org/10.1016/j.jhazmat.2021.125777.

[217] K. Li, G. Zou, T. Jiao, R. Xing, L. Zhang, J. Zhou, Q. Zhang, Q. Peng, Self-assembled MXene-based nanocomposites via layer-by-layer strategy for elevated adsorption capacities, Colloids Surf A Physicochem Eng Asp 553 (2018) 105–113. https://doi.org/https://doi.org/10.1016/j.colsurfa.2018.05.044.

[218] M. Kadhom, K. Kalash, M. Al-Furaiji, Performance of 2D MXene as an adsorbent for malachite green removal, Chemosphere 290 (2022) 133256. https://doi.org/https://doi.org/10.1016/j.chemosphere.2021.133256.

[219] B. Anasori, M.R. Lukatskaya, Y. Gogotsi, 2D metal carbides and nitrides (MXenes) for energy storage, Nat Rev Mater 2 (2017) 16098. https://doi.org/10.1038/natrevmats.2016.98.

[220] J.W. Choi, D. Aurbach, Promise and reality of post-lithium-ion batteries with high energy densities, Nat Rev Mater 1 (2016) 16013. https://doi.org/10.1038/natrevmats.2016.13.

[221] T. Liu, Y. Zhang, Z. Jiang, X. Zeng, J. Ji, Z. Li, X. Gao, M. Sun, Z. Lin, M. Ling, J. Zheng, C. Liang, Exploring competitive features of stationary sodium ion batteries for electrochemical energy storage, Energy Environ Sci 12 (2019) 1512–1533. https://doi.org/10.1039/C8EE03727B.

[222] L. Ma, X. Gao, W. Zhang, H. Yuan, Y. Hu, G. Zhu, R. Chen, T. Chen, Z. Tie, J. Liu, T. Wu, Z. Jin, Ultrahigh rate capability and ultralong cycling stability of sodium-ion batteries enabled by wrinkled black titania nanosheets with abundant oxygen vacancies, Nano Energy 53 (2018) 91–96. https://doi.org/https://doi.org/10.1016/j.nanoen.2018.08.043.

[223] O. Mashtalir, M.R. Lukatskaya, M.-Q. Zhao, M.W. Barsoum, Y. Gogotsi, Amine-Assisted Delamination of Nb2C MXene for Li-Ion Energy Storage Devices, Advanced Materials 27 (2015) 3501–3506. https://doi.org/10.1002/adma.201500604.

[224] M.R. Lukatskaya, O. Mashtalir, C.E. Ren, Y. Dall'Agnese, P. Rozier, P.L. Taberna, M. Naguib, P. Simon, M.W. Barsoum, Y. Gogotsi, Cation Intercalation and High Volumetric Capacitance of Two-Dimensional Titanium Carbide, Science (1979) 341 (2013) 1502 LP – 1505. https://doi.org/10.1126/science.1241488.

[225] Y. Wang, H. Dou, J. Wang, B. Ding, Y. Xu, Z. Chang, X. Hao, Three-dimensional porous MXene/layered double hydroxide composite for high performance supercapacitors, J Power Sources 327 (2016) 221–228. https://doi.org/https://doi.org/10.1016/j.jpowsour.2016.07.062.

[226] S. Xu, G. Wei, J. Li, Y. Ji, N. Klyui, V. Izotov, W. Han, Binder-free Ti3C2Tx MXene electrode film for supercapacitor produced by electrophoretic deposition method, Chemical Engineering Journal 317 (2017) 1026–1036. https://doi.org/https://doi.org/10.1016/j.cej.2017.02.144.

[227] L. Li, N. Zhang, M. Zhang, L. Wu, X. Zhang, Z. Zhang, Ag-Nanoparticle-Decorated 2D Titanium Carbide (MXene) with Superior Electrochemical Performance for Supercapacitors, ACS Sustain Chem Eng 6 (2018) 7442–7450. https://doi.org/10.1021/acssuschemeng.8b00047.

[228] D.D.L. Chung, Electromagnetic interference shielding effectiveness of carbon materials, Carbon N Y 39 (2001) 279–285. https://doi.org/https://doi.org/10.1016/S0008-6223(00)00184-6.

[229] S.H. Lee, S. Yu, F. Shahzad, J.P. Hong, W.N. Kim, C. Park, S.M. Hong, C.M. Koo, Highly anisotropic Cu oblate ellipsoids incorporated polymer composites with excellent performance for broadband electromagnetic interference shielding, Compos Sci Technol 144 (2017) 57–62. https://doi.org/https://doi.org/10.1016/j.compscitech.2017.03.016.

[230] M. Naguib, V.N. Mochalin, M.W. Barsoum, Y. Gogotsi, 25th Anniversary Article: MXenes: A New Family of Two-Dimensional Materials, Advanced Materials 26 (2014) 992–1005. https://doi.org/10.1002/adma.201304138.

[231] F. Shahzad, M. Alhabeb, C.B. Hatter, B. Anasori, S. Man Hong, C.M. Koo, Y. Gogotsi, Electromagnetic interference shielding with 2D transition metal carbides (MXenes), Science (1979) 353 (2016) 1137 LP – 1140. https://doi.org/10.1126/science.aag2421.

[232] J. Liu, H.-B. Zhang, R. Sun, Y. Liu, Z. Liu, A. Zhou, Z.-Z. Yu, Hydrophobic, Flexible, and Lightweight MXene Foams for High-Performance Electromagnetic-Interference Shielding, Advanced Materials 29 (2017) 1702367. https://doi.org/https://doi.org/10.1002/adma.201702367.

[233] X. Zou, H. Liu, H. Xu, X. Wu, X. Han, J. Kang, K.M. Reddy, A simple approach to synthesis Cr2CTx MXene for efficient hydrogen evolution reaction, Mater Today Energy 20 (2021). https://doi.org/10.1016/j.mtener.2021.100668.

[234] R. and S. Kummert, The surface complexation of organic acids on hydrous γ-alumina, Colloid Interface Sci,V. 75, (1980), 373 – 385 (n.d.).

[235] W. et S.B. Stumm, The Cycling of Iron in Neutral Environments: considerations based on laboratory studies of heterogenous Redox processes, Geochim. Cosmochim. Acta, V. 56, (1992), 3233 – 3257 (n.d.).

[236] A.M.L., K.K. and M.F.M.M. Kraepiel, On the acid-base chemistry of permanently charged minerals, Environ. Sci. Technol, V. 32, (1998), 2829 – 2838. (n.d.).

[237] M., L.S., B.F. and B.J.C. Davranche, An easy determination of the surface chemical properties of simple and natural solids, J. Chem. Educ., V. 80, (2003), 76 – 78. (n.d.).

[238] S.E.A.Ö.H.K.Ö. and S.A. George William Kajjumba, Modelling of Adsorption Kinetic Processes—Errors, Theory and Application, 2018.

[239] H.B. Tan KL, Insight into the adsorption kinetics models for the removal of contaminants from aqueous solutions, The Taiwan Institute of Chemical Engineers. 2017;74:25-48 (n.d.).

[240] A.H. C. H. Giles, A general treatment and classification of the solute adsorption isotherms, J. Colloid Interface Sci, 47(3), 755-777, (1974) (n.d.).

[241] J. Abenojar, F. Velasco, M.A. Martinez, Differential thermal analysis of the Al+20% (Fe–50%B) system, J Solid State Chem 179 (2006) 2787–2790. https://doi.org/https://doi.org/10.1016/j.jssc.2005.12.037.

[242] S. Kota, L. Verger, V. Natu, M. Sokol, M.W. Barsoum, Thermal stability of the nanolayered Fe2AlB2 in nitrogen and argon atmospheres, Journal of the American Ceramic Society 104 (2021) 733–739. https://doi.org/https://doi.org/10.1111/jace.17492.

[243] A.K.W. Chee, The Mechanistic Determination of Doping Contrast from Fermi Level Pinned Surfaces in the Scanning Electron Microscope Using Energy-Filtered Imaging and Calculated Potential Distributions, Microscopy and Microanalysis 28 (2022) 1538–1549. https://doi.org/10.1017/S1431927622000642.

[244] A.K.W. Chee, R.F. Broom, C.J. Humphreys, E.G.T. Bosch, A quantitative model for doping contrast in the scanning electron microscope using calculated potential distributions and Monte Carlo simulations, J Appl Phys 109 (2011) 13109. https://doi.org/10.1063/1.3524186.

[245] L.X. Yang, Y. Wang, H.L. Zhang, H.J. Liu, C.L. Zeng, A simple method for the synthesis of nanosized Ti3AlC2 powder in NaCl–KCl molten salt, Mater Res Lett 7 (2019) 361–367. https://doi.org/10.1080/21663831.2019.1613695.

[246] Y. et al Jin, Theoretical and experimental insights into the mechanism for gas separation through nanochannels in 2D laminar MXene membranes, Processes 7.10 (2019): 751. (n.d.).

[247] S. Kushwaha, H. Soni, V. Ageetha, P. Padmaja, An Insight Into the Production, Characterization, and Mechanisms of Action of Low-Cost Adsorbents for Removal of Organics From Aqueous Solution, Crit Rev Environ Sci Technol 43 (2013) 443–549. https://doi.org/10.1080/10643389.2011.604263.

[248] M. Kadhom, K. Kalash, M. Al-Furaiji, Performance of 2D MXene as an adsorbent for malachite green removal, Chemosphere 290 (2022). https://doi.org/10.1016/j.chemosphere.2021.133256.